TU DELFT

MASTER THESIS

Influence of Pore Connectivity on the Spalling Behaviour of Mortars

Author:
Laurens de Vilder

Supervisor:
F. Mendonça Filho
O. Çopuroğlu
K. Varveri

A report submitted in fulfillment of the requirements for the degree of Master of Science

in the

Materials and Environment Department
TU Delft

November 17, 2022

It gets easier
Everyday, it gets a little easier
But you gotta do it everyday
that's the hardest part
But it does get easier

Acknowledgements

I would like to thank all the persons involved and supported me through the writing of this thesis during these strange times.

A sincere thank you to all the people at TU Delft University who were there during the process. To Fernando for introducing and guiding me to academic research and writing. How to think and conduct the experiments and to always take care of the details. To Oguzhan for first introducing me with material sciences and getting me hooked on the subject. Stimulating to really think my results through with always sharp questions and remarks.

This thesis would not have been possible without the technicians of the MicroLAB, Maiko, Arjan, John and Ton who were an immense help in using the equipment with the proper procedures and understanding the acquired data information. Learning how to carefully work with the equipment in a safe way and providing useful tips and insights in how to plan and prepare all the pre-work before starting the actual experiments.

A thanks to all my friends and basketball teammates for the fun and laughter during the writing when everything else was closed during the writing of this thesis. To Luiz, Karthikeyan, Zhang Yu and all the other PhD and Master students who were around the lab to help or just have some small talk and coffee.

Lastly, I would like to thank my parents for supporting me through all those years. Having the patience when things weren't fully going the way they were supposed to and providing for me along the way.

Delft, January 2022
Laurens de Vilder

Contents

Acknowledgements iii

1 Introduction 1
- 1.1 Background . . . 1
- 1.2 Aim of the Study . . . 2
- 1.3 Outline of the Report . . . 3

2 Literature Review 5
- 2.1 Pore Structure of Cement Based Materials . . . 5
  - 2.1.1 Effect of hydration process, pore formation and W/C ratio . . . 6
  - 2.1.2 Classification of pore sizes . . . 8
  - 2.1.3 Porosity, pore size distribution and pore connectivity . . . 9
  - 2.1.4 Definition of pore connectivity . . . 11
- 2.2 Thermal Shock Resistance . . . 13
  - 2.2.1 Thermo-hygral mechanism . . . 13
  - 2.2.2 Thermo-mechanical mechanism . . . 15
  - 2.2.3 Thermo-chemical mechanism . . . 16
  - 2.2.4 Concrete dimensions . . . 17
  - 2.2.5 Degree of pore saturation . . . 17
  - 2.2.6 Heating rate . . . 18
  - 2.2.7 Pore connectivity . . . 19
  - 2.2.8 Polypropylene fibres . . . 19
- 2.3 Analysis Techniques . . . 20
  - 2.3.1 Mercury intrusion porosimetry . . . 20
  - 2.3.2 X-ray computed tomopgraphy . . . 20
- 2.4 Discussion and Conclusions . . . 22

3 Mix Design, Sample Casting and Mechanical Properties 25
- 3.1 High Strength Concrete Mix Design . . . 25
  - 3.1.1 Determination of aggregate distribution . . . 28
- 3.2 Sample Mix Design, Casting and Storage . . . 30
  - 3.2.1 Sample casting . . . 31
  - 3.2.2 Sample storage . . . 32
- 3.3 Mechanical Properties . . . 32
  - 3.3.1 Compressive strength . . . 32
  - 3.3.2 Elastic modulus & flexural strength test preparation . . . 33
  - 3.3.3 Elastic modulus . . . 34
  - 3.3.4 Flexural strength . . . 34
  - 3.3.5 Air content testing . . . 35

4 Thermal Shock Resistance: Spalling Behaviour **37**
4.1 High temperature (HT) experiments: W/C and PP Fibre Ratio Influence 37
4.1.1 Sample preparation . . . 37
4.1.2 Oven setup and procedure . . . 37
4.1.3 heating rate variation . . . 38
4.1.4 HT experiments: results . . . 39
4.1.5 Spalling behaviour . . . 39
4.2 HT Experiments: Recast 30 samples . . . 44
4.2.1 HT setup recast samples . . . 44
4.2.2 Recast spalling results . . . 46
4.3 HT Testing: Volume/Surface Influence . . . 47
4.4 Discussion and Conclusions . . . 48

5 Characterization of the Pore Structure **49**
5.1 X-Ray Computed Tomography . . . 49
5.1.1 Sample preparation . . . 49
5.1.2 Setup, equipment and procedure . . . 50
5.1.3 Processing of CT data - ImageJ/Fiji . . . 50
5.1.4 3D analysis - ImageJ/Fiji . . . 51
5.1.5 CT Porosity - ImageJ/Fiji . . . 58
5.1.6 CT porosity - VGStudio Max 3.0 . . . 58
5.2 Mercury Intrusion Porosimetry . . . 60
5.2.1 Sample preparation . . . 61
Arresting hydration method . . . 61
Exchange time arresting hydration . . . 62
MIP setup . . . 63
5.2.2 MIP porosity . . . 64
5.3 Pore structure analysis . . . 64
5.3.1 Pore Size Distribution . . . 64
MIP: pore size distribution . . . 64
CT: pore size distribution . . . 68
MIP+CT: pore size distribution . . . 71
Porosity: re-analysis through combined PSD . . . 79
5.3.2 Pore Connectivity analysis . . . 79
MIP: pore connectivity . . . 79
CT: pore connectivity . . . 81
Tortuosity script: pore space & non-pore space . . . 82
Tortuosity script: cement and pore space . . . 83
5.4 Predicting spalling: Formula . . . 84
5.5 Discussion and Conclusions . . . 87

6 Conclusions and Recommendations **89**

Bibliography **91**

A Figures Oven Results **99**

B VGStudio Max 3D reconstruction images **113**

C Tortuosity results **119**

Chapter 1

Introduction

1.1 Background

High strength concrete is a material increasingly being used in industries, high rise buildings, and marine applications. Its high strength allows for cheaper design with reduced dimensions while being more durable and able to withstand heavier loads [86]. By reducing the dimensions of concrete, less cement is needed. Which in turn is beneficial to the environment as it reduces the amount of CO_2 produced during cement manufacturing. This reduction in CO_2 being one of the main environmental goals the world is facing currently.

High strength concrete is manufactured using superplasticizers, enabling a lower water to cement ratio as the superplasticizer maintains the workability of the concrete [13, 72]. Combined with a finer aggregate size and possibly pozzolanic materials, it allows for a much denser packing structure with a lower porosity, achieving a higher strength and durability as a result [13, 37, 86].

A problem that has been encountered with high strength concrete, is that the resistance to fire and high temperatures is insufficient. This resistance is referred to as the thermal shock resistance. The high temperature causes spalling, causing pieces of concrete to break away from the surface, leading to deterioration of the concrete [22, 23, 34]. One of the main causes of this behaviour is believed to be the denser and more refined pore structure of high strength concrete. The combination of a low water to cement ratio and refined pore structure through finer aggregate and pozzolanic materials, gives the concrete a lower porosity and lower pore connectivity [34, 37]. Consequently preventing water vapour from escaping through the pore network and causing a build up pressure [83]. In short, the properties that allow the concrete to have a high strength, have negative effects on the thermal shock resistance.

A proven solution to this problem is the use of polypropylene (pp) fibres. By melting when heated beyond 170 °C, they create extra pore channels in the concrete. The created extra pore channels increase the pore connectivity, consequently raising the thermal shock resistance [58]. A multitude of experiments have been performed in recent years on the use of pp fibres to prevent spalling. Proving its efficiency and refining the fibre percentage and length through different experimental researches.

However, most of these experiments evaluate the concrete on a global scale, assessing the sufficiency of the concrete in terms of a yes or a no. On a microstructural level or even smaller, much is still unknown on why the pp fibre works to prevent spalling, or why certain concrete mix designs don't even require pp fibres [58].

It is believed that by assessing the pore connectivity on a nano-microstructural level in concrete, a clearer understanding and possible quantification can be made on

the thermal shock resistance and consequential spalling behaviour of cement based materials. The focus of the presented study will be on achieving this through experimental research.

1.2 Aim of the Study

The main aim of this study is to characterize the pore structure and connectivity of mortar samples and determine if there is a correlation with the spalling behaviour.

More specifically, the first goal is to assess through literature how the pore connectivity is defined and how it can be influenced during mix design. Besides the influence, additional knowledge is required on the quantification of pore connectivity, and if there is a usable definition. Furthermore, the spalling mechanisms have to be assessed and to determine how the spalling behaviour can be influenced through different parameters.

Through experimental research, the goal is to assess the spalling behaviour of samples with different sizes and compositions by testing the samples in a heating oven. The first series of testing will involve a varying water/cement ratio with different polypropylene fibre contents. The second series of testing will involve a varying volume/surface ratio.

Similar samples with the same composition will be put through computerized tomography (CT) and Mercury intrusion porosimetry (MIP) analysis to characterize the pore structure. The goal to find a way through the CT scans to quantify the pore connectivity by using a tortuosity code. Besides the tortuosity code, the CT scan will allow to map out the 3D structure of the mortar samples on a microscale. This will result in a porosity and pore size distribution value per sample.

To complement the results for porosity and pore size distribution through CT, MIP was used. The MIP results gave additional information for the pores on the nanoscale level. The goal was to check whether it is possible to combine both results and get a complete overview of the pore structure. The following goal was to check if this combination can further enhance the prediction of the pore connectivity.

Lastly, the acquired pore connectivity was compared with the spalling results. The aim was to find a relation between the pore connectivity and spalling behaviour, that allowed to establish a value for sufficient pore connectivity in relation to the thermal shock resistance of a cement based material.

In short, to summarize, the following research questions were addressed in this study:

1. How does the pore connectivity relate to the spalling behaviour according on existing research literature? Are there other parameters that should be taken into account?

2. What is the influence of the water/cement ratio, the pp fibre ratio, the heating rate and the volume/surface ratio on the spalling behaviour of the mortar samples through experimental research?

3. Is it possible to map out the pore connectivity of a sample using MIP and CT techniques?

4. Is it possible to predict/estimate the spalling behaviour of mortar samples based on their pore connectivity and the influencing parameters tested through

spalling research, the water/cement ratio, the pp fibre ratio, the heating rate and the volume/surface ratio?

1.3 Outline of the Report

The thesis is divided into 5 chapters, which will contain the following information:

Chapter 1 is the present chapter, containing the motivation for carrying out this study and the aim of the experimental campaign.

Chapter 2 contains a literature review on the present research of the required knowledge to commence the thesis. It discusses how the pore structure of cement based materials is formed, and how it can be influenced. Furthermore, addressing the thermal shock resistance of cement based materials with it's different mechanisms and how to influence it through various parameters. Additionally, a literature review into the chosen analytical techniques is presented. Besides the theoretical knowledge through literature, the chapter contains a section committed to the mix design of high strength concrete and how it can influence the thermal shock resistance.

Chapter 3 presents another small literature review in the possible constituents for the mortar mix design followed by the actual mix design for the experiments. The casting and storage procedure of the mix design is described afterwards. Lastly, the chapter contains the tested mechanical properties that were thought to be of influence on the thermal shock resistance of the samples.

Chapter 4 contains the first series of testing for the oven experiments, in which samples were tested with varying W/C ratio and pp fibre ratio at different heating rates. Furthermore, containing the second series of testing which were aborted due to using a different oven that was insufficient in thermal shock resistance testing.

Chapter 5 presents all the techniques used to identify and characterize the pore structure of the samples. MIP and CT was used to respectively map out the nanoscale and microscale pore structure of the samples. A 3D overview is presented of all the casted samples using the CT results. Using the acquired results an analysis was performed on the pore structure. The MIP will give an overview of the nanoscale pores which are undetectable through CT, while the CT results present . The analysis of the results will present an overview of the total porosity, pore size distribution and pore connectivity of the samples. Finally, a formula is presented that was able to predict the spalling behaviour of the presented samples.

Chapter 6 contains the conclusions and recommendations for further research.

Chapter 2

Literature Review

This chapter is dedicated to a literature review into a number of interests before experimental research could be commenced. Namely, the formation of the pore structure, the thermal shock resistance of cement based materials and its mechanism, and finally the analytical techniques that will be used during the experimental research. After initiating the experimental research, new interests and insights were found. Consequently, sections have been revised and added while the research progressed.

The first section looks into the pore structure of concrete, how it develops and matures, and it's different parameters for classification. The subsequent section will dissect the thermal shock resistance of concrete, mainly the different spalling mechanisms and the influencing factors on the the thermo-hygral spalling behaviour. Afterwards, a literature review of the analytical techniques is done that were used during the experimental research.

2.1 Pore Structure of Cement Based Materials

In acquiring a sufficient overview of how the thermal shock resistance is influenced by the pore structure, a primary definition of the pore structure and it's influences has to be made. Where do pores reside in the concrete and how are they created during the hydration process are of utmost importance to facilitate the knowledge on how the pore connectivity is created in different mix designs.

The mechanical properties of concrete are a direct consequence of the amount of pores present. In more specific terms, a lower volume of pores generally leads to an increase in strength of cement based materials [37, 63, 72, 79]. With the amount of pores mostly controlled by the water/cement (W/C) ratio, a lower W/C ratio resulting in a decreased amount of pores.

The relation between the water/cement ratio and the compressive strength was already reported in 1898 by Feret [31]:

$$F_c = k * \frac{1}{1 + (W/C)^2} \tag{2.1}$$

In which F_c is the compressive strength of the concrete, k a factor depending on the used cement and W/C the water over cement ratio. It is clear that to increase the strength and decrease the pores of concrete, the W/C ratio has to be lowered.

The amount of pores can be expressed as a total pore volume, and relative to the total volume of the material, it is described as the porosity of the material. Porosity is primarily seen as the main influence on compressive strength. But this can be divided further into the pore size- and pore spatial distribution, maximum pore size, pore shape and pore connectivity [5].

Not only does the pore structure influence the mechanical properties but it also influences the transport properties of cement based materials. These transport properties influence both the durability and thermal shock resistance of concrete as it allows movement of liquids and gasses inside the porous network [3, 26, 37].

2.1.1 Effect of hydration process, pore formation and W/C ratio

Pores are created due to the reaction products of cement having a smaller volume than the initial water and cement combined, causing chemical shrinkage of the concrete [99]. As the cement hydrates, CSH (calcium silicate hydrate) is formed as a reaction product of water and cement on the outer surface of the cement particles while also expanding into the pore space. As hydration continues, the formed CSH layers start to grow towards each other and possibly forming a connection between layers, subsequently creating gel pores between the connected CSH layers. While capillary pores are created in the initial water volume as the water is used during hydration [5, 37]. The described expansion of hydration products happens over time. Consequently, the porosity and the pore structure are being lowered and refined over time as the concrete matures [48].

The CSH layers are the most important hydration product of concrete, as it is the main contributor to the mechanical properties and durability of concrete. These CSH layers can be further divided into inner and outer product CSH, in which the inner product is the stronger and more favourable one [3, 37, 63, 95]. Other main reaction products are CH (calcium hydroxide) and CASH (monosulfate hydrate). In which CH is considered to play a minor role in the strength development, and CASH on the microstructure property relations of concrete [63].

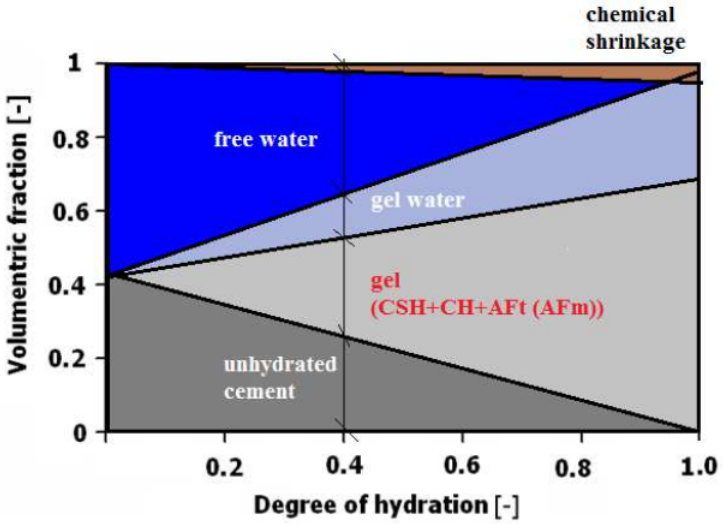
Furthermore, the pore structure should not be viewed as a homogeneous distributed component in the cement paste. Cement paste close to the aggregates has a different pore structure compared to the bulk cement paste [5, 26]. The cement paste structure close to the aggregates is referred to as the interfacial transitional zone (ITZ). The distribution of the pore space within the ITZ is generally not a smooth radial function of distance but rather resemble different areas with either locally extensive porosity intermingled with areas of sparse porosity [26].

The ITZ zone is seen as the main limiter in the maximum compressive strength of concrete due to it's irregular composition around the aggregate, consequently, cracking usually develops in this area [37, 63].

To describe the hydration process, there exist a number of models for cement based materials. Most of the models describe a homogeneous linear reaction, and are quite accurate on a global scale.

Perhaps the most famous model describing the process of hydration and how it's hydration products are formed is the Powers's model [74]. Describing how the initial unhydrated cement and water react to form the 3 phases in hydrated cement; the gel, gel water, and the creation of pores due to chemical shrinkage, see Figure 2.1.

To further show the hydration process according of the Powers's model, Mehta and Monteiro [63] illustrated that after hydration, the volume can be divided in the hydration products and capillary pores. Using the fact that 1 cm^3 of cement hydrates into 2.12 cm^3 of hydration product, the anhydrous cement volume can be converted to a final hydration product volume, see Figure 2.2 [3, 63, 74]. Illustrating how lowering the W/C ratio decreases the amount of capillary pores in the end product and consequently, generally increases the strength of cement based materials.



;

FIGURE 2.1: Powers's model for cement hydration [74]

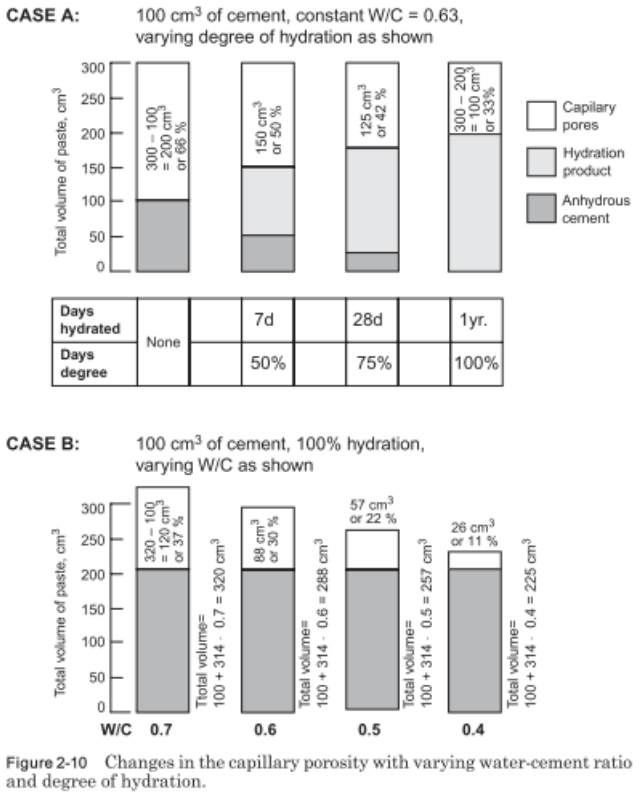


Figure 2-10 Changes in the capillary porosity with varying water-cement ratio and degree of hydration.

;

FIGURE 2.2: Capillary porosity development with varying W/C ratio according to Mehta and Monteiro [63]

There should however, be a note on the hydration of cement at a lower W/C ratio. Theoretically, the lowest possible W/C ratio is 0.42 to fully hydrate Portland cement according to the Powers's model. 1g of cement is able to bind 0.23g of chemically bound water during hydration reactions and 0.19g of strongly physically bound gel water, adding up to 0.42. Consequently, 0.42 is the lowest possible W/C ratio to fully hydrate cement particles [5, 37, 74]. This chemically bound water is part of the gel in the Powers's model and is chemically bound in the CSH and

CH reaction products, while the strongly physically bound gel water exist in the gel pores and is represented in the Powers's model as gel water.

Resulting in the question how it is possible for high strength concrete to go lower than 0.42 W/C ratio and still become stronger. This is due the fact that the cement doesn't have to fully hydrate, just enough to grow towards adjacent cement grains and create mechanical bonds, and as stated earlier, the strength is controlled mostly by the amount of pores, not the amount of hydrated cement. The unhydrated cement will have a similar function as the aggregate [37]. Additionally, with the use of additives such as superplasticizer, the cement can be kept workable while lowering the W/C ratio [3, 6, 13].

Furthermore, a more illustrative way to visualize this decrease in porosity with lower W/C ratio is seen in Figure 2.3. Notably showing how mortar/concrete with a decreasing W/C ratio, the distance between cement grains decreases. Consequently, a lower capillary volume develops in the initial water volume. Furthermore, as the cement particles are closer to each other, it is easier to bond between cement particles and refine the pores, subsequently not only lowering the porosity but also decreasing the pore sizes. Finally, as parts of the product become enclosed, research has shown that moisture movement becomes sluggish, which improves the formation of inner product CSH [3, 5].

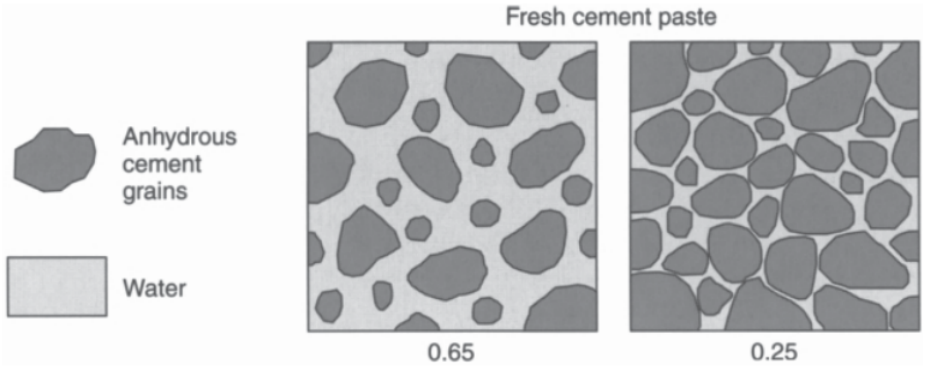


Fig. 5.6 Schematic representation of two fresh cement pastes having a water/cement ratio of 0.65 and 0.25. In this representation the ratio of the surface of the water to that of the cement is equal to the massic water/cement ratio.

;

FIGURE 2.3: Schematic representation of the influence of the W/C ratio [3]

Lastly, there are also the air voids in the concrete that can be classified as either entrapped or entrained air. Both these types of air voids are generally seen in a spherical shape. Entrapped air is usually created during the mixing process, as some air is trapped in the cement paste during mixing, while entrained air can be created by using certain admixtures in the concrete [63].

2.1.2 Classification of pore sizes

In hydrated paste, 2 distinct classes of pores exist, the gel pores and the capillary pores. At any stage the hardened paste contains a mixture of gel, calcium hydroxide, some minor components and unhydrated cement and, important for the definition of the pores, a residue of the water filled spaces in the fresh paste, the capillary pores. While within the gel itself there exist another structure of voids, the gel pores [26, 37].

The pore system can be divided in 3 types according to the IUPAC, the micropores with dimensions smaller than 2 nm, the mesopores from 2 to 50 nm and finally the macropores that are larger than 50 nm[5]. However, different opinions exist on the classification of the pore sizes and how to define them as seen in an overview in Figure 2.4.

Other definitions of the pores depend on their function, either gel pores (0.5 - 10 nm), capillary pores (5 - 5000 nm) or macropores (larger than 5000 nm)[52].

The pores can be further classified into the classes of interlayer pores (0.58-0.63 nm), gel micropores (1.55-2.89 nm) and the inter-hydrate pores between CSH clusters (no range given) for the gel pores. While the capillary pores can be divided into the fine capillary pores and the combination of coarse capillary pores, air voids and small cracks (no range) [97].

Table 1.1 Classification of pore sizes according to the general classification by the IUPAC and to concrete science terminology [1.39]

According to IUPAC [1.35]		According to P. Mehta, 1986 [1.40]		According to S. Mindess *et al.*, 2002 [1.4]				
Name	Diameter	Pore type	Size range	Name		Diameter	Role of water	Paste properties affected
Micropores	Up to 2 nm	Interparticle space between C–S–H sheets	1 nm to 3 nm	Micropores "inter layer"	Gel pores	Up to 0.5 nm	Structural water involved in bonding	Shrinkage, creep at all RH
				Micropores		0.5 nm to 2.5 nm	Strongly adsorbed water; no menisci form	Shrinkage, creep at all RH
Mesopores	2 nm to 50 nm			Small (gel) capillaries		2.5 nm to 10 nm	Strong surface tension forces generated	Shrinkage between 50% and 80% RH
		Capillary pores (low w/c)	10 nm to 50 nm	Medium capillaries	Capillary pores	10 nm to 50 nm	Moderate surface tension forces generated	Strength, permeability, shrinkage at high RH, >80%
Macropores	>50 nm	Capillary pores (high w/c)	3 µm to 5 µm	Large capillaries	Hollow-shell pores	50 nm to 10 µm	Behaves as bulk water	Strength, permeability
		Entrained voids	50 µm to 1 mm	Entrained air		0.1 mm to 1 mm		Strength

Notes
These are the most commonly mentioned classifications with reference to hydrated cement pastes. The hollow-shell pores were not included in the classification by S. Mindess *et al.*

;

FIGURE 2.4: Classification pore sizes[5]

For this thesis, the exact sizes will be left up to debate, only using the definition of gel pores, capillary pores and air voids. These definitions are found to be the most useful in defining the concrete pore structure and the development of the pore structure as it matures.

2.1.3 Porosity, pore size distribution and pore connectivity

Porosity is the most common parameter for defining the pore structure of cement based materials, and is used to predict mechanical and transport properties of cement based materials. Porosity can be divided into two classes; the total(or absolute) porosity, and the effective porosity [5].

Total porosity is defined as the fractional volume of pores with respect to the total bulk volume of the material, see Equation 2.2 [5, 37]. The total porosity is a dimensionless quantity, defined as a percentage value. Total porosity contains both the open and closed pores in a system. Since some techniques can only determine

open pores, it should always be reported which method is used when reporting the results [5].

$$Porosity = 100 * \frac{V_p}{V_b} \tag{2.2}$$

Where V_p is the total pore volume of the bulk in mm^3, and V_b the bulk volume of the material.

Effective porosity is described as the fraction of pores only consisting of open and interconnected pores with respect to the bulk volume of the material. It uses the same formula as described in 2.2, only the total pore volume is replaced with the open and interconnected volume of pores [5].

However, different literature states that the pore size distribution is actually a better criterion at evaluating the characteristics of cement based materials. Stating that the use of the pore size distribution can give a clearer understanding of the pore sizes present and the quantity of the pore sizes in the cement based material [63]. Capillary voids larger than 50 nm are stated to be more influential on the strength and permeability characteristics, while the voids smaller than 50 nm play a more important role in drying shrinkage and creep. With the use of the pore size distribution the pore structure of the cement based material is captured more clearly and consequently the characteristics can be determined more effectively [37, 63].

Lastly, a useful property, especially for the given experimental research, is the pore connectivity or permeability of cement based materials. Describing how the pores are interconnected with each other and allow gases or liquids to flow through it's pore structure [37, 61, 86].

In definition permeability and pore connectivity differ in that permeability describes the ability of outside substances to flow through the pores of the cement matrix. In pore connectivity they do not have to be connected to the outside of the matrix and allow flow of gasses but rather only have to be interconnected on the inside of the cement matrix [7].

Armatas [7] expressed the combined effect of the pore size distribution and pore connectivity on the ability of the porous material to diffuse gasses. Properties such as the mean pore size and the standard deviation of the pore size range, influence the tortuosity and the effective pore diffusivity significantly for a porous material with low pore connectivity. The paper recommends constructing the pore size distribution and the pore connection distribution as a narrow set of values to obtain the most effective system.

Figure 2.5 shows the relation between connectivity and the pore radius, and the diffusivity of the material as a consequence of those combinations. Figure 2.6 shows how it the combination of connectivity and pore radius relates to the tortuosity. It can be deduced from the figures that pore connectivity in combination with the pore radius can have a significant influence on the material's diffusivity.

In terms of thermal shock resistance this is one of the more interesting parameters, as permeability and pore connectivity can be used to define how the pore network is able to dissipate water vapour pressures caused by heating [57, 61, 86, 89]. Low permeability and an insufficient increase in permeability during heating are stated to be highly problematic for the spalling resistance of concrete [49].

Unfortunately, the definition for pore connectivity is quite variable through literature, and quantification is even more subjective, mostly depending on the experimental data acquired when measuring [15, 75]. As this definition and quantification

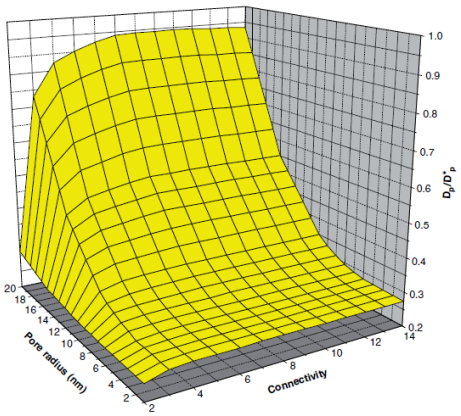


FIGURE 2.5: Relation between pore radius, pore connectivity, and the diffusivity of the porous material[7]

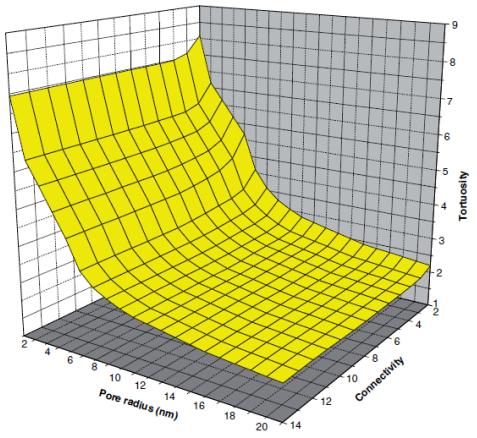


FIGURE 2.6: Relation between pore radius, pore connectivity, and the tortuosity of the porous material [7]

is of reasonable interest to the presented research and experiments, a separate literature review section is dedicated to the definition and possible quantification in 2.1.4.

2.1.4 Definition of pore connectivity

In general, pore connectivity is a relatively well understood property, but with a somewhat variable definition and quantification. Different definitions are used throughout literature for the pore connectivity, such as pore interconnectivity or describing the property in terms of permeability. Illustrating that besides the unknown quantification, a clear definition doesn't exist for the property either. Through literature, multiple definition have been found, some with an additional method of quantification or just an advice. This section summarizes these findings, accompanied by an evaluation on the definition and effectiveness of the described quantification method.

First definition was proposed by Zhao et al. [96], defining pore interconnectivity as:

Definition 1. *The voids with both ends connected to external space are classified as valid interconnected pores*

The paper actually defines what part of the connected pore structure contributes to the permeability of liquids through porous asphalt. Given the context of the research, the definition is actually stating what the usable connected pores are in terms the permeability and not on the internal pore connectivity.

Quantifying the pore connectivity was done using CT images and running them through a Matlab program to build a three-dimensional matrix, and subsequently running a subroutine to identify the interconnected pores. The end result for the interconnected pores is defined as volume space in m^3.

Second definition was proposed by Armatas [7], in which the paper defines pore connectivity as the following:

Definition 2. *The number of throats/bonds that are connected to the same pore body/node*

This definition is more appropriate to describe the property as it takes into account the network of pores rather than a single path that runs through the sample. Furthermore, the paper is more relevant to the proposed experimental research in cement based materials. The research states a mathematical approach on how to study the flow and transport in porous media using a dual site-bond lattice model (DSBM). Through this model, relations were found between the different properties of concrete and how they affect gas diffusion properties.

The main findings were to not only look at the total pore connectivity, but to also examine the pore connectivity distribution. A poorly connected porous material suffers greatly from a varying distribution in the pore connectivity. The poorly connected material, along with a varying pore connectivity distribution, causes the material to have certain volume spaces with an even greater disconnected porous network. By not taking the pore connectivity distribution into account, the diffusivity and tortuosity values could be wrongly estimated.

In light of the proposed research in this paper, this could mean that the thermal shock resistance is overestimated, and consequently will give a poorer prediction model.

Bossa et al. [15] defined pore connectivity when researching the connectivity through micro computed tomography as the following:

Definition 3. *Pore connectivity is defined as the number of void voxels in the largest percolating pore cluster divided by the total number of void voxels in the VOI*

Which can be described as the largest connected pore volume divided by the total pore volume. This definition is more focused on describing the connectivity through CT scanning. In which VOI is short for "Volume of interest".

It appears that this method of analysing the connectivity disregards the possibility of multiple large pore spaces to exist in a concrete sample. For instance, the paper describes the pore connectivity as 13% of the concrete, as this is the volume of the largest connected pore space. However, multiple other connected pore spaces of a lower percentage than 13% could co-exist in the concrete. Consequently, the combined connected pore spaces could take up a much higher percentage of the the total volume. Additionally, with the previously mentioned pore connectivity distribution by Armatas [7], a more thorough overview of the pore structure could be determined with the available results.

The described method to define the pore connectivity could be useful. However, rather than only assessing the largest connected pore space in regard to the total volume, every connected pore space crossing a certain threshold value should possibly be considered towards the connectivity. With the threshold value being determined as a value at which the pore connectivity increases the thermal shock resistance of the concrete.

Lastly, Promentilla et al. [75] used the same definition as Definition 3 when analysing the connectivity through CT scanning. In addition, the paper stated to use a specific principle to determine the connected pores.

The principle used is defined as the cluster multiple labeling technique to identify and label connected pore clusters using the 6-point connectivity rule [38]. The principle is relatively simple, voxels are considered connected when they share a common face with another voxel, voxels that only share an edge or vertex are considered disconnected. The resulting set of connected voxels is then considered as

a pore cluster. The resulting cluster is used to determine the connectivity by the previously described Definition 3.

The last step in the paper is to convert the connectivity back to a value for the effective porosity. Explaining that when the porosity is 21% and the pore connectivity 87%, the resulting effective porosity is the multiplication of both values, hence acquiring an effective porosity of 18%.

The main weakness of this method is viewed to be the heavy reliance on the voxel resolution. This could either mean a low voxel resolution with a representative volume or an adequate voxel resolution with a too small area of interest as the voxel resolution is related to the volume of interest. The first option would mean an under representation of connected pore space, while the second option would have a too small area of interest to be representative for the whole material.

2.2 Thermal Shock Resistance

The thermal shock resistance of a material has to be defined initially for the purpose of this research. Thermal shock resistance is defined by Lu and Fleck [60] as the ability of a material to withstand a jump in temperature without showing cracks. When the thermal shock resistance is insufficient, it is possible to observe spalling in concrete.

Spalling is the term used for concrete pieces that violently explode of the main concrete structure. These pieces fly off the concrete by a large build-up of tension forces that are quickly created within the concrete [34, 49, 83].

It was discovered that the thermal shock resistance and spalling is influenced by a multitude of variables, which can influence three different types of spalling mechanisms. The three types are identified as thermo-hygral, thermo-mechanical and thermo-chemical spalling. The three types have a distinctive way in which the degradation is initiated and enhanced by certain parameters. Illustrating that there is not one single mechanism that controls the thermal shock behaviour, but is rather controlled by the different parameters that influence the response.

Consequently, it is believed that by enhancing or reducing certain variables, one of the mechanisms can become the dominant mechanism, while the other mechanisms are reduced in contribution. The following sections will try to address the way these mechanisms are described in literature, and how the reactions are influenced through different variables.

2.2.1 Thermo-hygral mechanism

The thermo-hygral mechanism is explained as the build up of pore pressure due to water vapours unable to escape through the pore structure. It can also be referred to as pore pressure spalling [40, 58, 90].

Different sources mention different sample temperature zones at the location of spalling during the heating that the spalling mechanism can occur. Luz, Braulio, and Pandolfelli [61] explains that this happens between the temperatures of 100-300 °C, referring to it as the ebullition stage. Kalifa, Menneteau, and Quenard [42] mentions it to happen between 190-250, while Liu, Tan, and Yao [58] explains it will most likely happen in the range of 220-320 °C.

Through literature the mechanism is explained not entirely the same way and different terms are used to describe the zones, but they all concur on how the vapour

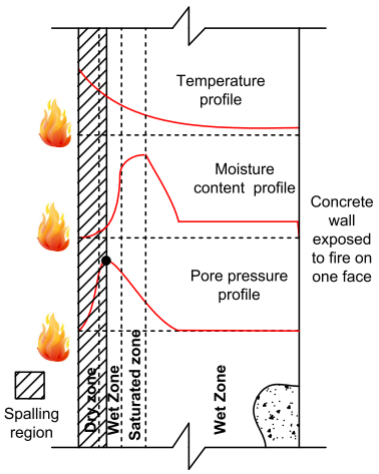
pressures build up. The common thread of the mechanism is explained through literature as follows [32, 42, 49, 58, 79, 90]:

(1) As the concrete is subjected to heating, vaporization will happen inside the concrete. Capillary water, gel water and physically bound water vaporize at around 100 °C. The heating will cause a moisture movement in the concrete due to the temperature difference inside and outside the concrete. Moisture partly moves outside the concrete and partly moves further inside the concrete to the cooler regions. Consequently, creating a dry zone at the surface area. While the vapour that moves inside the concrete will partly condensate and create a mixture of vapour and liquid water.

(2) As the heating progressing, the vaporization takes place deeper in the concrete. This causes the mixture of vapour and liquid to again fully vaporize and move further inside the concrete. Moving the dry zone further inside the concrete.

(3) The constant flow of vapour moving deeper inside the concrete will cause an accumulation of water moisture and vapours. When this accumulation is unable to move deeper inside the concrete, a so-called moisture clog or (quasi-)saturated zone is formed. When this happens, the vapours are trapped between the heat and the moisture clog, causing the pore pressure to build up quickly. This zone in front of the moisture clog in which the trapped vapours reside, is referred to as the wet zone in some literature, a seen in figure 2.7. The accumulation can possibly induce spalling when the build-up of vapour pressure passes the tensile strength of the concrete. Hence, the term pore pressure spalling is commonly used.

The mechanism is explained and illustrated in figure 2.7 and 2.8.

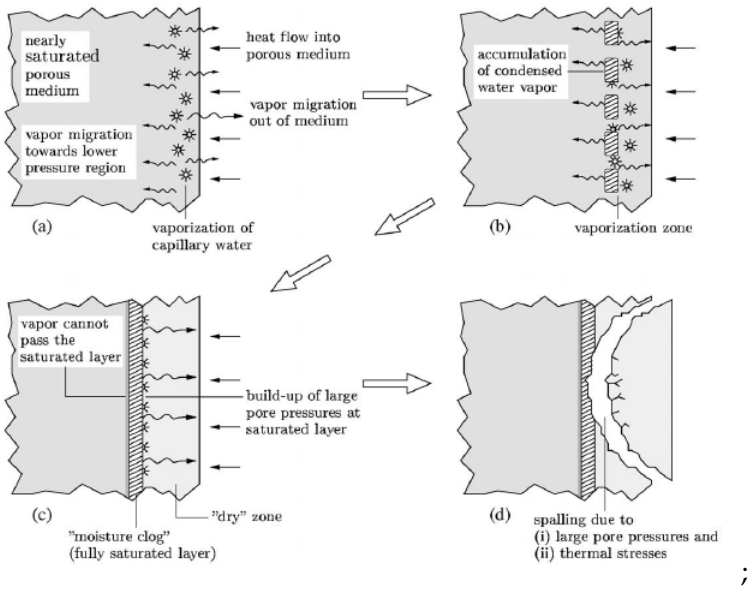


;

FIGURE 2.7: Mechanism of thermo-hygral spalling [58]

The thermo-hygral mechanism is the mechanism most influenced by the pore structure, pore connectivity, moisture content and permeability, as the vapour movement is largely influenced by the ability to move outside or further inside the concrete [23, 56, 58, 83, 90]. When the pore connectivity/permeability is lower, the moisture clog will happen closer to the surface [58].

Different researches have tried to numerically model the thermo-hygral spalling behaviour with the permeability as variable with relative success in line with their own experimental results [43, 59]. Showing possible guidance in the analysis of the proposed experimental research.



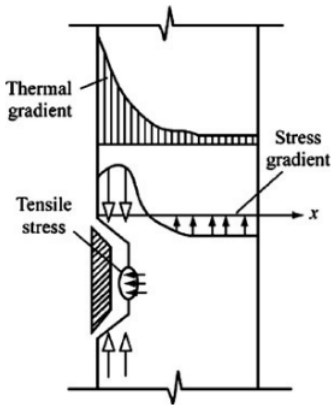
;

FIGURE 2.8: Mechanism of thermo-hygral spalling, also stating the thermo-mechanical influence [90]

2.2.2 Thermo-mechanical mechanism

Thermo-mechanical spalling is caused by a temperature gradient occurring in the concrete specimen. The gradient arises from the difference between heated outside surface and cooler inner sections, causing thermal stresses inside the member as a consequence of this temperature difference [44, 49, 58]. The gradient increases with higher heating as the temperature difference is bigger between inside and outside of the concrete. Consequently, increasing the risk of spalling with higher heating rates [49]. The mechanism is explained in literature as follows:

When dilation is restrained, bi-axial thermal stresses are caused parallel to the surface as the concrete wants to expand when heated, which induce tensile stresses perpendicular to the surface [32, 49, 90]. The tensile stresses cause spalling in the same way as the pore pressure spalling. If the tensile stresses exceed the tensile strength of the concrete, spalling occurs, see figure 2.9.



;

FIGURE 2.9: Overview of thermo-mechanical spalling [9, 32]

The thermo-mechanical reaction is greatly influenced by the applied compressive strength and the degree of restrain. A preload as low as 5% of the compressive strength can increase the risk of spalling significantly [16, 49, 58]. This is due to the fact that the compressive force will restrain the dilation caused by the heating, and will increase the previously described bi-axial thermal stresses.

Bazant [9] hypothesised that while pore pressure from water expansions serves as the trigger of spalling, it cannot explain the mechanism on it's own. Explaining that when the pore pressure causes cracking to appear, the pore pressure should drop as a larger volume area becomes available to expand. Stating that the stored thermal stresses from the thermal gradient are actually the trigger of spalling to happen after the initial cracking is caused by the vapour pressures.

That there is a conjunction with the thermo-hygral/pore pressure mechanism and the thermo-mechanical mechanism is a view shared among scholars through experimental and theoretical research [9, 32, 42, 49, 58, 90]. However, opinions differ on the main/dominant mechanism that induces spalling.

Lastly, different opinions exist on which mechanisms fall under the thermo-mechanical reaction. Some describe the shrinkage and dilation of cement and aggregate (sloughing-off spalling, see Section 2.2.3) as part of the thermo-mechanical reaction [42, 47, 49], while other research separates this behaviour under a separate mechanism, the thermo-chemical [58].

2.2.3 Thermo-chemical mechanism

The thermo-chemical mechanism is a later discovered mechanism during the writing of this thesis. Most research defines it as part of the thermo-mechanical mechanism, but should be mentioned for the purpose of this research. The Thermo-chemical mechanism is described to happen beyond 700 °C [58], and is thus considered outside the scope of the current experimental research.

Liu, Tan, and Yao [58] described it as two possible mechanisms. Namely, sloughing-off spalling and post-cooling spalling. Especially post-cooling spalling is still stated to be limited in knowledge and research on the mechanism. Both mechanisms are described to be much less explosive than the other counter mechanisms, thermo-hygral and thermo-mechanical spalling.

Sloughing-off spalling happens as a result of degradation between the cement-aggregate bond. This degradation is caused by the breakdown of calcium hydroxide and CSH, which causes the cement to shrink [58]. The process is described as the progressive breakdown of cement phases as temperature rises [79]. Combined with the expansion of aggregate when heated, cracking starts to occur progressively in between the cement-aggregate bond as temperature rises [40, 47].

Post-cooling spalling happens when the temperature drops after heating. When the calcium carbonate in the calcareous aggregate starts to decompose at high temperatures and turns into calcium oxide. During cooling, moisture is reabsorbed into the cement based material and starts to react with the newly formed calcium oxide, forming calcium hydroxide. This reaction product has an increase of 44% in volume, possibly causing cracking and spalling in the concrete due to the expansion [58].

Furthermore, post-cooling spalling happens in a more progressive manner and needs certain precondition such as an environment with sufficient moisture and enough generated calcium oxide. The reaction is much slower than that of thermo-hygral and thermo-mechanical spalling, and can take weeks to see an effect [58].

2.2.4 Concrete dimensions

The concrete dimensions play an important role in both the thermo-hygral and thermo-mechanical mechanism. With the previously described mechanisms, it can be understood that with a thicker sample, moisture can travel further inside the concrete or a larger temperature gradient is created between inside and outside of the concrete specimen. Consequently causing a larger build-up of stresses. However, only the thickness is insufficient to describe this phenomena. The influence is best described with taking into account both the volume and surface area of the sample. More specific for the surface area is the surface area exposed to heating [58, 60].

A quantity to describe the influence of concrete dimensions, is the Biot number [60, 61], see equation 2.3.

$$B = h * L/K \tag{2.3}$$

In which h is the heat transfer coefficient by convection, K the solid thermal conductivity and L the characteristic body length. In which L is referred to in the heating of solids as the V/A ratio, the previously described volume over exposed surface area.

Through literature multiple experimental researches have been found which all exhibit the same results, namely that a higher Biot number will increase the likelihood of spalling. Cardoso et al. [21] showed that when increasing samples with equal diameter and height from 2.1 cm to 5.2 cm, the samples went from not spalling to spalling.

Hertz [36] cast cylindrical ultra strength samples in the sizes from 200x100, 100x57 mm and 52x28 mm. Only causing the largest cylindrical sample to explode with a heating rate of 1 °C/min. Debicki, Haniche, and Delhomme [25] tested spheres of high performance concrete with different fibre contents with diameters of 0.12, 0.18 and 0.24 m, showing that for a fibre content of 0.5 kg/m^3 the samples with a diameter of 0.12 did not spall while the 0.18 and 0.24 samples did spall. Kanéma et al. [44] also reported a clear perceived scale effect in its research when heating samples.

All found experimental research results clearly illustrate the effect of an increasing Biot number, and how it influences the thermal shock resistance of cement based materials of the same quality.

2.2.5 Degree of pore saturation

The degree of pore saturation (DPS) is mostly of influence on the thermo-hygral spalling mechanism. It's quite clear that with more moisture inside the pores of a sample, larger pore pressure build-up is caused by the vapour pressures when heated.

Li et al. [56] did extensive reading into the moisture content, concluding that it is a major indicator for the risk of spalling. Different samples under different curing conditions and drying conditions showed a clear correlation between the moisture content and risk of spalling for similar concrete samples. However, one of the findings is that water cured samples have a lower risk than air cured samples, attributing this to the expansion of water causing microcracks in the structure, which help relieve the pressure by increasing the pore connectivity. Important to note is that while a specimen can be fully submerged in water, the capillary pores inside a cement paste will still not be entirely saturated with water [50].

Research by Liu, Tan, and Yao [58] concluded that while according to Eurocode 2, spalling is unlikely to occur at moisture contents lower then 3%, the correct measure should be DPS instead of moisture content, as moisture content fails to take the porosity in account. To further clarify, a moisture content of 3% has a much more damaging effect in a concrete sample with 4% porosity compared to a sample with 10%. Hence, by using the DPS instead of moisture, the amount of saturation in the pores is defined more clearly.

Ramal, Salomão, and Pandolfelli [76] showed in experimental research that samples with higher DPS will spall sooner and at a lower sample temperature. Concluding that the pore pressure build-up is quicker inside the concrete at higher degrees of saturation.

Connolly [24] stated that oven drying samples at 105 degrees completely mitigates spalling, while concrete with a moisture content of 4-9 % did show spalling. Although it is known from background research into stopping hydration (see chapter 5.2.1), that drying at 105 °C not only dries the concrete but also damages the microstructure of the concrete[91], consequently increasing pore connectivity. Thus the results should be taken with some considerations.

Mendonça Filho et al. [64] showed in experiments that by drying samples in isopropanol and reducing the DPS, the cracking pattern changes when samples are heated. Cracking changes from parallel cracking towards the heated surface for hydrated samples to perpendicular cracking for dried samples. Illustrating how drying the sample converts the dominant spalling mechanism from hygral to mechanical spalling.

2.2.6 Heating rate

In terms of the thermo-hygral mechanism, a high heating rate combined with a low pore connectivity causes the vapour pressures to build up more quickly, reaching a value that causes spalling of the concrete [39, 83, 90]. The pore pressure build-up is quicker and relatively closer to the surface with increasing heating rates [8]. For thermo-mechanical mechanism the higher heat rate causes larger heating gradients inside the specimen, consequently increasing the bi-axial stresses [49, 58].

While the heating rate does influence the spalling behaviour, a high heating rate is not a prerequisite for spalling to happen. Through different studies it was found that spalling can happen at lower heating rates of 0.5 °C/min [49, 73], 1.0 °C/min [36, 49], and 3 °C/min [25]. Important to note is that these results were achieved when dealing with high strength or ultra-high strength concrete, using silica fume as a constituent. Displaying the effect of the porosity and pore connectivity.

Additionally, different spalling behaviour is observed under different heating rates. When concrete is subjected to a low heating rate, spalling behaviour tends to be a sudden bursting failure with a loud bang, spalling deeper inside the concrete. When concrete is under fast heating, spalling behaviour is dominated by progressive peeling-off with continuous popping sound close to the surface. Both the one-time explosive spalling and progressive spalling occur in a violent manner [58]. Klingsch [49] described it as the following: ”High heating rates lead to spalling layer-by-layer, while low heating rates lead to spalling initiated in the core of the specimen. Moisture migration into and out of the specimen and drying of concrete layers caused these different failure mechanisms”.

Results seem to indicate the the spalling behaviour is an interaction between the heating rate and the ability of the concrete to dissipate the vapour pressure. Showing

that concrete with a more refined pore system and high strength is also prone to spalling at low heating rates [36, 44]. Displaying how the heating rate interacts with the ability to dissipate pore pressure through the pore connectivity.

The reported findings indicate that a higher heating rate forces the concrete to dissipate vapour pressures faster through the pore network, and when unable, vapours will build-up and cause spalling. What happens with spalling at lower heating rates is that the pore connectivity is never sufficient enough to allow vapour pressures to dissipate through the pore network. Consequently, pore pressure build-up is bound to happen at any heating rate in these low connectivity samples.

2.2.7 Pore connectivity

The basics and definition of pore connectivity are discussed in section 2.1.3 and 2.1.4. This section will discuss it's influence on the spalling behaviour of cement based materials.

Pore connectivity not only influences whether or not the concrete spalls, but also the way it spalls. Concrete with a denser microstructure and lower permeability usually has shallower spalling at the surface, while concrete with a higher permeability has the moisture move further inside the concrete and cause spalling in a deeper region [35, 56]. Higher pore connectivity improves the ability to dissipate vapour pressures, consequently improving the resistance against spalling [22, 83].

Klingsch [49] stated that silica fume is decisive parameter in the spalling behaviour. Explaining that with silica fume the permeability decreases and consequently shallower spalling will happen. Silica fume is know as constituent that greatly refines the pore structure because of it's very fine dimensions and pozzolanic effect.

It's effect is demonstrated in combination with the previous described heating rate. An interaction between the two is proven quite clearly [36, 44]. The pore connectivity being a deciding factor in the spalling behaviour is understood quite clearly, and ways of improving it have been researched extensively. The main solution being the use of pp fibres which help to create extra pore channels [3, 41, 49, 83].

2.2.8 Polypropylene fibres

Polypropylene (PP) fibres have shown to mitigate plastic and early drying shrinkage by increasing the tensile strength of the concrete [45]. Consequently, by resisting the crack propagation, the durability of the concrete is increased. A side effect of polypropylene fibres is that it reduces the workability of concrete.

More importantly for this research, pp fibres have shown to improve the thermal shock resistance of cement based materials. Other types of fibres have shown similar improvement, such as PVA fibres [56, 57, 77].

In terms of Thermal shock resistance pp fibres have shown to increase the resistance significantly by creating additional pore channels at low heating temperatures, increasing the pore connectivity [12, 61, 90]. Specifically, the pp fibres melt at around 170 degrees and leave behind an open pore channel that allows vapours to move through [83], Consequently allowing more pores to connect to each other , increasing the pore connectivity and lowering the pore pressure build-up [12, 90].

The positive effect of pp fibres on the thermal shock resistance by creating pore channels is undisputed, and has been researched and proven multiple times results

[23, 83, 90]. However, different opinions exist on how they mitigate the pore pressure build-up in the cement based materials.

Liu and Tan [57] questioned the way plastic fibres improve the thermal shock resistance by using PVA instead of PP fibres. PVA fibres melt at a higher temperature (240 °C), while spalling usually happens between 190 and 250 °C [40]. Meaning that the fibres only start melting at the end of the risk zone for thermo-hygral spalling. Nonetheless, the fibres showed to mitigate the spalling risk. The research showed that before melting, fibres expand and cause microcracking around it's interfacial transition zone, which could possible be part of the mechanism of fibres that improves the spalling resistance. Zeiml et al. [90] hypothesized that it is actually the ITZ zone that is created around the fibres before heating and during hydration that improves the resistance, in addition to the melting mechanism.

2.3 Analysis Techniques

The research has used two different techniques, MIP and CT, to assess the pore structure of the cement based materials. To fully comprehend the results and it's possible shortcomings a small additional literature review is given on MIP and CT.

2.3.1 Mercury intrusion porosimetry

Mercury intrusion porosimetry (MIP) is a common tool used to asses the pore structure of cement based materials. Through reviewing the papers of Abell, Willis, and Lange [1] and Münch and Holzer [66], the following was learned about MIP.

The technique works on the idea that a non wetting liquid can only intrude capillary pores under pressure and that a certain pore diameter requires a specific pressure to allow it to enter. The relationship between applied pressure and pore radius is described by the Washburn equation [84]:

$$P = \frac{2 * \gamma * cos(\theta)}{r} \tag{2.4}$$

In which P is the applied external pressure, γ the surface tension of mercury , θ the contact angle and r the capillary radius. The pore size distribution is consequently calculated by measuring the volume intruded per pressure increase.

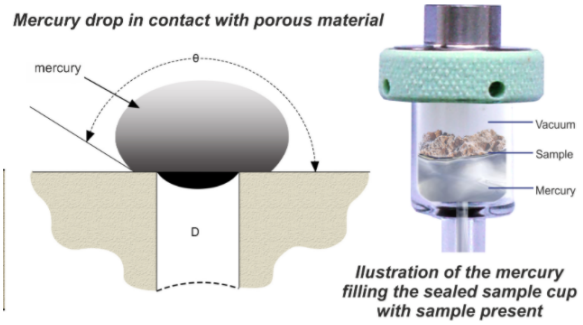
The shortcomings of this technique are that only the connected pores to the outside of the specimen are measured, as isolated pores cannot be intruded [27]. Additionally, a small sample is needed from the concrete to put in the setup, thus the need to damage the specimen in order to do MIP testing.

Furthermore, another issue is that for increasingly smaller pore sizes a larger force is required to intrude the specimen, possibly causing damage to the internal structure of the sample and consequently not giving an entirely accurate pore size distribution.

Lastly, there is the problem of the so called "Ink bottle-effect", in which larger pores are mistakenly seen as smaller pores, as the entrance to the pore is of a small diameter.

2.3.2 X-ray computed tomopgraphy

The following facts were learned through literature review about x-ray computed tomography scanning [15, 18, 75]. X-ray computed tomography is usually referred



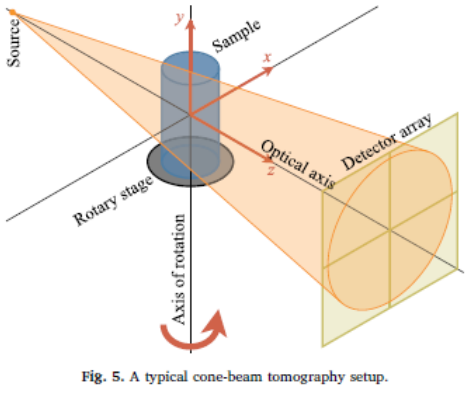
;

FIGURE 2.10: MIP intrusion setup[81]

to as CT scanning, and depending on the scale either as micro CT or Nano CT in cement based research. It is a non destructive technique that is used to scan a (concrete) sample and provide a grey level three dimensional image of the entire volume content.

The setup for CT scanning is visualized in Figure 2.11 and can be explained as follows:

The source produces x-rays and directs them at the sample. The sample sits in the middle and is able to rotate 360° as to create a 3-dimensional view. Behind the sample is a detector that measures the intensity of the x-rays coming from the sample. X-rays are able to pass through the sample depending on the density, registering different intensities for varying densities. As concrete is heterogeneous, it will show different intensities depending on where the x-ray passes through. For example, air will have a black colour as it has close to no density, while cement will show up as light grey, as it is most of the times the densest constituent in the cement based material.



;

FIGURE 2.11: CT scanning setup[19]

Shortcomings of this technique is the resolution, better described as the voxel size. Voxel size is the true dimensions of a sample, opposed to resolution which is the optical quantity that quantifies the ability of an imaging setup to separate close objects. Furthermore, even though the resulting image slices are in 2D, each voxel contains a value in the 3 dimensional space. Shortcoming are the limited voxel size

using CT, allowing only for microns to be recognized. Meaning that the smallest pores in cement based materials are not distinguishable using a CT scan.

The limited voxel size consequently also limits the results for the analysis of the pore connectivity. Previous research found that while for micro CT the pore connectivity was 13%, the connectivity through nano CT was 97% or higher [15]. The results from the proposed experiments should thus rather be viewed in regards to the spalling behaviour, and if the limited view of the connectivity is enough to predict the risk.

2.4 Discussion and Conclusions

The literature review into the thermal shock resistance and spalling behaviour of cement based materials gave some new insights to the mechanisms at play. There are a multitude of factors that have an influence on the spalling behaviour. Most factors are not singularly causing spalling to happen, but rather cause spalling to happen with a combination of negatively influencing factors. The main insights and discoveries are summed up below:

1. Initially the general assumption was that the main cause of spalling is pore pressure spalling, also termed as thermo-hygral spalling. Through literature review it was discovered that spalling is dictated by three different mechanisms, the thermo-hygral mechanism, the thermo-mechanical mechanism and the thermo-chemical mechanism. Each has different influencing factors that contribute to the build-up of forces through the mechanism. By altering these influencing factors, one of the mechanisms can become the more controlling mechanism in the consequent spalling behaviour.

    - To further explain, thermo-hygral is believed to be influenced most by the W/C ratio, pozzolanic materials (silica fume being the most influential), heating rate and DPS. To a lesser degree it is believed to be influenced by the volume/surface ratio. Each parameter either controlling the pore connectivity, the water content, or the distance and speed the vapours can and need to travel through the material. By tweaking with the described parameters, the thermo-hygral mechanism can become more pronounced.
    - With the thermo-mechanical it is slightly different, but with some overlap with the thermo-hygral mechanism. Thermo-mechanical is similarly controlled by the volume/surface ratio and the heating rate, allowing higher heating gradients to develop inside the concrete. In addition to these parameters, the degree of restrain and the load level are of large influence on the response. Both parameters influencing the degree of expansion that is allowed during heating, consequently influencing the build-up of the bi-lateral stresses.
    - Lastly there is the thermo-chemical mechanism, but not much is yet known about it. Some influencing factors that have been discovered are the used of aggregate. Mainly, siliceous aggregate has a larger volume expansion when heated, while calcareous aggregate will degrade into calcium-oxide and cause damage during cooling as it reabsorbs moisture and consequently expands.

2. With the acquired knowledge, it is believed that thermo-mechanical spalling is of more significant influence than initially thought. Especially the restraint caused by the compressive forces in the structure can cause a notable increase in spalling risk. It is believed that this mechanism is dominant in spalling seen in structures such as tunnels, in which the concrete lining is loaded with large compressive forces.

3. Applying the acquired theoretical knowledge from the literature review, it's thought to be possible to have either a thermo-hygral or thermo-mechanical dominant spalling mechanism. However, truly isolating the mechanism is believed to be very difficult in an experimental setup.

    - To observe a thermo-hygral dominant mechanism, it is essential to create an as much as possible refined pore structure combined with a high moisture content. Using a low W/C ratio in combination with silica fume, high DPS and high heating rate will refuse the water vapours of travelling further inside or outside the concrete. Creating shallow spalling very close to the surface, which is believed to be the spalling behaviour mostly influenced by the thermo-hygral mechanism. This might not even need a high volume/surface ratio, just enough to create a moisture clog inside the specimen.
    - To create a thermo-mechanical dominant mechanism, some amplification of the thermo-mechanical parameters has to be done while defusing most of the thermo-hygral mechanism. Applying a load to the sample, combined with a high heating rate and volume/surface ratio to increase the thermal gradient are thought to be controlling parameters for the thermo-mechanical mechanism.

      To limit most of the thermo-hygral mechanism, it is thought that drying the sample will be enough to greatly reduce it's influence.

Chapter 3

Mix Design, Sample Casting and Mechanical Properties

This chapter is dedicated to the determination, casting and testing of certain mechanical properties of the mix design.

First, as the initial focus of the research was on the thermal shock resistance of high strength concrete, the possible constituents and how it can affect the thermal shock resistance of concrete was researched trough literature. Afterwards, the choice of different mix designs with varying W/C ratios and PP fibre ratios to influence the spalling behaviour. Lastly, certain mechanical properties were tested that are of influence on the spalling behaviour. Namely, the compressive strength, the flexural strength, the elastic modulus and the initial air content.

3.1 High Strength Concrete Mix Design

Like normal concrete, high strength concrete is made using cement, water and aggregates. However, high strength concrete usually includes a combination of additives, fillers, lower water to cement ratio and finer aggregates to increase the strength properties [13, 72, 86]. High strength concrete is classified as concrete with a compressive cylinder strength higher than 40 MPa according to US standards, C50/60 and higher according to EU standards [86]. High strength concrete is usually produced by lowering the water to cement ratio (W/C) with the use of superplasticizers, typically achieving a W/C ratio between 0.25 and 0.35 [72]. Additionally, a finer aggregate size is often used to achieve a better packing and form a more compact concrete.

Furthermore, if the concrete has improved durability and abrasion resistance it can be classified as high performance concrete [86]. Specifically, this increased durability can be achieved in a number of ways, mostly done with fillers such as silica fume, fly ash or blast furnace slag [13, 54, 86]. Other mechanical properties such as the tensile strength can be increased by using steel fibres in the concrete [86]. On top of all this, the use of polypropylene fibres is suggested as an effective measure to increase the thermal shock resistance of high strength concrete [12, 33, 83, 90]. To get a clearer view on the mix design of high strength concrete for the proposed research, the above mentioned possible components have been reviewed through literature.

Water/cement ratio versus water/binder ratio

First it is important to state the difference between the both. Water cement ratio only takes into account the amount of cement in the mix, while water binder ratio takes

into account the amount of cement plus the additional fillers [37].

Water to cement (W/C) and water to binder(W/B) ratios are the most important characteristics of concrete according to Aïtcin [2], as it controls the microstructure in fresh and hardened states and also influences the durability. Further stating that when the W/C ratio is low, it results in rapid development of very strong bonds and very low porosity, as it places the cement particles close to each other. Consequently, the bonds between particles are formed quickly and give a better strength development for the concrete.

Furthermore, Aïtcin [2] states that both ratios should be taken into account when cement is partly replaced with fillers, explaining that W/C ratio is important to consider in the short term, as the first hydrates to develop are on the surface of the cement particles, while the pozzolanic fillers react and develop later, depending on the fineness of the pozzolanic material [13].

Lastly stating that the initial capillaries network is no longer be governed by the W/C ratio for long term consideration, but by the w/b ratio, as well as the strength development and durability [2]. Consequently, when analysing or designing a concrete mix, the w/b ratio should be governing for the mix design.

Superplasticizer

Superplasticizers are highly effective water reducers. The mechanism of superplasticizers is by giving the cement particles negatives charges and thus repelling each other due to the same electrostatic charge[6, 72]. The research stating that this results in the deflocculation and dispersion of the cement particles, achieving a higher workability of the mix. With this increased workability, the water content can be lowered, consequently lowering the water cement ratio, which in turn causes an increase in compressive strength of the concrete [6, 13, 37, 72].

Neville and Aïtcin [72] state that the superplasticizer interacts with tricalcium aluminate (C_3A), and that C_3A is the first component of cement to hydrate by reaction with the gypsum and other alkali sulfates. Advising that not all C_3A should become fixed with superplasticizer, stating that the cement can become incompatible. Consequently, it is important to consider the solubility of the gypsum(calcium sulfate) as it needs to start the cement hydration by reacting with the C_3A, and being aware that more sources of calcium sulfate can exist in different forms in the cement.

As for mix proportioning of superplasticizer, the advice according to Neville and Aïtcin [72] is 5-15L per cubic meter concrete, depending on the active solids in the superplasticizer and the reactivity of the cement as explained above. The effectiveness of superplasticizer is dependant on multiple factors such as the ambient temperature, cement chemistry, and fineness aggregate [13]. Alsadey [6] advises a general usage of 1-3 l/m^3, with possible dosages up to 5-20, stating that the concentration of superplasticizer varies, and thus should be made on the amount of solids and not on the basis of total mass.

Silica fume

Silica fume is a pozzolanic material usually consisting of ultra fine particles and often added in high strength concrete as a filler. Silica fume lowers porosity, permeability and consequently increases the durability [72]. The ultra fine particles of the silica fume fill the spaces between the cement grains, consequently achieving a better packing. Additionally, it increases the strength development of the concrete,

as it's SiO_2 content reacts with $Ca(OH)_2$ creating extra CSH chains [86]. This pozzolanic reaction usually develops slower over time, however, the finer and vitreous the pozzolanic material, the faster this reaction will be [13]. As silica fume is usually made up of very fine particles it improves the 28 day compressive strength of concrete [14]. In literature it is stated that silica fume begins to react at roughly 3 days [2].

Recommendations on the dosage of silica fume is between 5-15 % of the total cementitious mass according to Neville and Aïtcin [72], stating that higher percentages are wasted, as the optimal packing density is reached. Other reports [46] state that an optimal packing density is reached between 10-20 %. This difference can possibly be attributed to the difference in cement grain fineness, as the silica fume particles fill the spaces between the cement grains. Consequently, the spaces that can be filled by silica fume vary per mix design. A combination of both papers would suggest a dosage of 10-15% to replace cement content as a safe assumption.

Blast furnace slag

Blast furnace slag is a byproduct of steel production, it is a pozzolanic material which can be used to partly replace the cement content.Blast furnace slag strength development usually has a 28 days reaction, depending on the degree of disorganization(vitrification) [2]. The greater the disorganization, the more reactive the slag. The disorganization is a function of the temperature of the liquid slag when it is quenched, the higher the temperature of the slag, the higher the level of disorganization [2]. Furthermore, the colour of the slag reveals the degree of disorganization, a pale slag has a high degree of disorganization, a darker slag having a low degree of disorganization. As with silica fume, blast furnace slag SiO_2 content reacts with $Ca(OH)_2$ creating extra CSH chains [86]. Lastly, the fineness is also of influence on the reactivity, but it is of importance that blast furnace slag is grinded separate of the concrete as it grinds more difficult than the clinker [37].

Recommendation for blast furnace slag to replace cement content are quite high. In a literature review done by Cabrera-Madrid, Escalante-Garcia, and Castro-Borges [20] it was found that up to 50% of the cement can be replaced with blast furnace slag without much consideration. When exceeding this ratio, careful determination of the mix design is advised as the combination with other additives can have adverse effects. Upper limit possibility is up to 70% in when risk for carbonation is low, otherwise the ratio should never exceed 50%.

Fly ash

Fly ash is a pozzolanic material and a byproduct of burning pulverized coal. Using it in concrete, it has positive effects on the long term development of strength and durability [37]. It has the slowest reactivity of the common pozzolanic fillers, with a usual development of strength at 56-91 days after casting [2]. As fly ash replaces cement, less superplasticizer is needed when used in concrete [72]. Fly ash refines the pores structure long term, as it's SiO_2 content reacts with $Ca(OH)_2$ creating extra CSH chains, taking up to 2 years to fully cure [87]. Consequently, fly ash gives a higher porosity after 1 year but with a better durability, as durability is more governed by critical pore size than porosity according to Yu and Ye [87]. Further stating that while fly ash has some influence on porosity, the W/B ratio is more significant.

Considering thermal shock resistance, it has a positive influence, as heating up to 400 degrees actually strengthens the concrete, and heating up to 1000 degrees shows a slower degradation compared to ordinary portland cement [4].

Fly ash has 2 categories, fly ash class F and class C. While class F contains very little lime, class C usually contains around 10% [2]. As for the mixing recommendations for high strength concrete, fly ash can be used to replace cement up to 25%, as higher ratios have significant negative effects on the 28 day strength [62].

Aggregate size

Aggregate size is of influence for high strength concrete as a denser and more compact concrete is used to increase the strength and durability. Finer aggregate sizes are wanted that pack well into each other when designing high strength concrete [2]. Recommendations according to Neville and Aïtcin [72] are that the fineness modulus of the the fine aggregate should be between 2.7-3.0, being coarsely graded. The coarse aggregate is recommended to not be larger than 10 to 14 mm, it should not contain any reactive silica, and flaky or elongated shapes are unwanted as they can prevent an optimal packing of the aggregates. Further explaining that smaller maximum aggregate sizes will reduce the differential stresses at the aggregate-cement interface, and that smaller aggregates are usually stronger as the grinding removes the largest flaws in the aggregates.

3.1.1 Determination of aggregate distribution

For the use of aggregate there was some discussion among supervisors as to whether to use it or not, as it can influence MIP results. The point was made that with aggregate present, the porosity might be over or underestimated depending on the aggregate presented in the prepared MIP sample.

Research done by Winslow and Liu [85] showed that porosity increases when aggregates are used in the mix compared to just plain paste or mortar at similar degrees of hydration. Proving that aggregate in the mix influences the pore size distribution and overall porosity significantly. A clear increase between paste and mortar pore diameter can be observed in Figure 3.1. However, mortar and concrete are quite comparable in terms of porosity and pore size distribution. It is noted by the author that the slight variation in aggregate content between the mortar and cement might be the cause for the minimal difference.

It can be concluded from the results that testing mortar samples is similar to concrete samples, while testing cement paste on it's own is significantly different in pore structure.

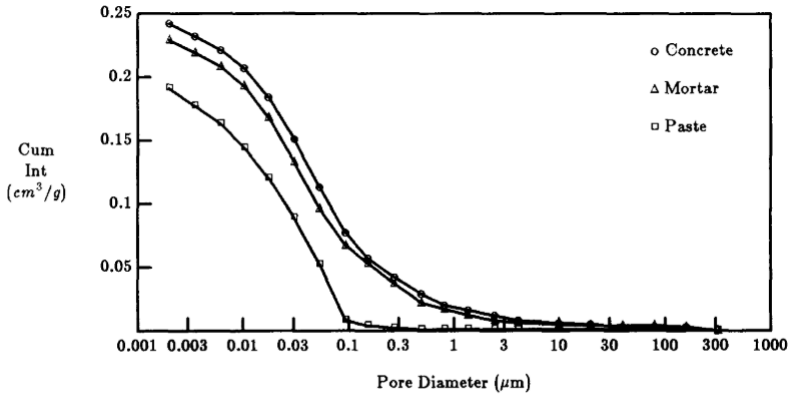


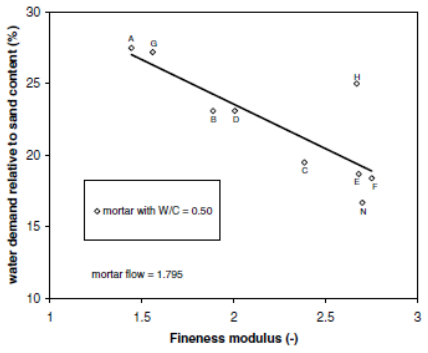
Figure 2 - Pore Structure of More Hydrated Samples, w/c = 0.45

FIGURE 3.1: Difference in pore structure between paste, mortar and concrete at 10+ days hydration [85]

With this in mind, the decision was made to use aggregate in the mix design for the spalling experimental research, but not bigger then 1 mm. The maximum aggregate size was determined at 1 mm to account for possible variability in the microstructure of the samples when testing for MIP. Meaning that the aggregate might take up most of the sample space, consequently giving a lower porosity as more of the sample volume is taken by the aggregate volume.

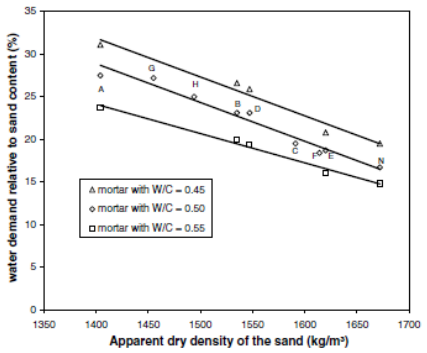
An aggregate distribution was made according to the Andreassen model [53]. The acquired mix design was found to lack workability, and required either more water, more superplasticizer, or less aggregate content. Each choice being undesirable for the mix design, additional literature review was done to determine how to improve workability without the need for extra superplasticizer, water content or less aggregate content.

Research by Schutter and Poppe [80] proved that with an increasing fineness modulus of the sand, the water demand increases as well. Determining that the type of sand and fineness modulus influences the workability of the mortar, and sand-cement ratio needs to be adjusted to achieve the same workability compared to a mix with normalised sand. Water demand was measured against the fineness modulus, as plotted in Figure 3.2. Proving that a smaller fineness modulus has a higher water demand to achieve the same workability.



;

FIGURE 3.2: Water demand versus fineness modulus of the aggregate [80]



;

FIGURE 3.3: Water demand versus the apparent dry density of the aggregate [80]

Additionally, it has been determined that the correct method to estimate what the water demand will be of a mortar sample, is to calculate the apparent dry density of the sand [80]. This shows a very strong correlation with the water demand, see figure 3.3.

Following these conclusions, it was decided to use CEN-NormSand DIN EN 196-1. The decision based on the fact that it has a higher fineness modulus compared to the Andreassen method, and a proven effective aggregate distribution for good workability. The aggregate distribution for CEN-NormSand DIN EN 196-1 is shown in Table 3.1.

TABLE 3.1: CEN-NormSand DIN EN 196-1 distribution

Mesh (mm)	**2.0**	**1.6**	**1.00**	**0.5**	**0.16**	**0.08**
Cummulative %	0.0	7	33	67	87	99
Retained %	0	7	26	34	20	12

Polypropylene fibres

Polypropylene is a plastic fibre that is being used more often in high strength concrete mixtures as it has positive influences on the thermal shock resistance and durability of concrete. Extensive review on how it improves the resistance is given in Section 2.2.8.

Different recommendations are found for the fibre content, such as 2.0 kg/m^3 according to Eurocode 2 for prevention of explosive spalling in high strength concrete [83].With a high performance concrete of 40 MPa, a fibre percentage of 0.05% (0.45 kg/m^3)by weight and W/C 0.40, showed to mitigate spalling[33]. While a study done by P. Kalifa et al. (2001)[41] stated that while recommendations are 2 kg/m^3, it could effectively be reduced to 1 kg/m^3 for HPC under 100 MPa. Furthermore, a study on ultra high performance concrete showed that not only the percentage is important, but also the length of the pp fibre[12]. Point of attention in all these results and recommendation is that there is less mention of the heating rate influence, which has been determined as a major influence on the spalling behaviour of concrete[32, 60, 73].

3.2 Sample Mix Design, Casting and Storage

All samples were cast mortar made with Portland cement type CEM I 42.5N, tap water and CEN-Norm Sand with a distribution according to DIN EN 196-1 [70]. To achieve a difference in porosity and pore connectivity throughout the samples, the water/cement (W/C) ratio and polypropylene (pp) fibre ratio were varied. The W/C ratio being determined by weight and the pp fibre ratio by volume. The fibres used were Fibermesh 150, which possess 12 mm length and 31 µm in diameter. Some mixes presented poor workability, in which case MasterGlenium 51 was used as superplasticizer.

An overview of the sample labelling is given in Table 3.2 and what they mean in terms of variety in the mix design. Table 3.3 and Table 3.4 contain the exact mix

design for respectively the first series of casting and the recasting of the 30 samples. The 30 samples were recast as problems were encountered during testing (see Section 4.1 for full explanation).

TABLE 3.2: Overview of sample labelling

Sample name	W/C ratio (%)	PP fibre ratio (%)
30_0	0.30	0.00
30_5	0.30	0.05
30_1	0.30	0.10
40_0	0.40	0.00
40_5	0.40	0.05
40_1	0.40	0.10
50_0	0.50	0.00
50_5	0.50	0.05
50_1	0.50	0.10

TABLE 3.3: Mix proportions of cast samples

Material	30 samples (kg/m^3)	40 samples (kg/m^3)	50 samples (kg/m^3)
Cement	712.89	665.41	624.17
Water	213.87	266.16	312.08
Aggregate	1425.78	1330.82	1248.33
Superplasticizer	(3.15; 3.72; 5.05)	0	0
PP fibre (0.00%; 0.05%; 0.1%)	(0; 0.45; 0.91)	(0; 0.45; 0.91)	(0; 0.45; 0.91)

TABLE 3.4: 30 samples recast

Material	30 samples (kg/m^3)
Cement	712.89
Water	213.87
Aggregate	1425.78
Superplasticizer	(3.13; 3.42; 5.05)
PP fibre (0.00%; 0.05%; 0.1%)	(0; 0.45; 0.91)

3.2.1 Sample casting

Mixing was done using a Hobart planetary mixer. First, all the dry ingredients (cement, aggregate and pp fibre) were combined and mixed for 30 seconds on speed 1. Afterwards, water was added while mixing at speed 1. Then, depending on the mix design, the mixing time and steps varied.

For the 0.30 W/C ratio, mixing was done for 6 minutes, until the desired workability was achieved. First half of the water volume was added and mixed, then 0.5% superplasticizer was mixed with the remaining half of water. The adding of superplasticizer and 0.5% superplasticizer was done in the first minute of mixing. Afterwards, mixing was continued while, if necessary, extra superplasticizer was added until a sufficient workable mix was achieved. In the 6 minutes, 30 seconds of mixing at speed 2 was done to speed up and disperse the superplasticizer through the mix.

The 0.40 W/C ratio samples were mixed for 4 minutes while observing if superplasticizer was necessary. In the end it was decided to forgo the use of superplasticizer and cast the samples without adding it to the mix.

The 0.50 W/C ratio samples were mixed for 2 minutes without any additional steps.

Samples were cast in plastic cups of 55 mm diameter and varying height between 80-90 mm height. Per mix design, 8 samples were cast. amounting to a total of 64 samples. After 2 weeks of hardening, samples were cut to identical shapes of 55 mm diameter and 65 mm in height.

3.2.2 Sample storage

Samples were stored in the lab for 24 hours at 22 °C. After 24 hours they were demoulded and stored in the fog room at 20 °C and >95% RH. Then, depending on the experiments performed the samples were either stored for circa 56 days for the oven and pore structure experiments or 28 days for the mechanical properties. This variability in maturity was due to the COVID restrictions in the lab which caused some delay in the oven and pore structure experiments. Each specified chapter will describe the exact number of days at which the tests were performed.



FIGURE 3.4: Demoulding of 30_0 sample after 24 hours of casting

3.3 Mechanical Properties

3.3.1 Compressive strength

Compressive strength tests were performed to give an actual strength number to the cast samples. Most papers state either researching normal, high strength/performance, ultra high strength/performance concrete or mortar before conducting experiments. In light of this, it was decided to determine the compressive strength quality of the cast samples.

Compressive strength test samples were prepared by casting 4x4x16 cm samples inside a Styrofoam mould. The samples were cast air tight for 24 hours inside the mold. Afterwards, the samples were removed from the Styrofoam mould and placed

inside the fog room for 20 days, at 20 degrees and >95% RH. After 20 days samples were cut to 4x4x4 cm samples. Samples were then placed back inside the fog room for another 7 days. Finally, the samples were removed from the fog room and tested after a total of 28 days of curing.

Compressive strength tests were performed using a Macben Cube press for small specimens. Samples were placed inside a steel cylinder specific for 4x4x4 cm samples. A loading rate of 1.5 kN/sec was used with a starting load of 2000 kN. Results of the tests are represented in Table 3.5.

TABLE 3.5: Compressive Strength Results

Sample	Compressive strength [MPa]	Test 1 [MPa]	Test 2 [MPa]	test 3 [MPa]
30_00	73.84	75.67	78.17	75.89
30_05	68.08	78.39	73.56	73.35
30_10	81.05	75.15	78.41	78.20
40_00	55.42	44.27	55.59	52.42
40_05	49.25	46.23	44.88	46.78
40_10	44.00	48.59	51.20	47.93
50_00	41.02	46.09	44.67	43.92
50_05	42.18	43.11	43.32	42.87
50_10	44.77	39.14	42.62	42.18

3.3.2 Elastic modulus & flexural strength test preparation

Samples were cast using the mix design described in Section 3.2.

For the elastic modulus experiments, 6 different mortar mix designs were selected. These are similar to the previously used mix design. Only the design with 0.05 % is left out due to lack of time during testing. A total of 3 samples per mix design were cast in styrofoam moulds. These styrofoam moulds had dimensions of 40 mm width, 40 mm height and 160 mm length.

For the flexural strength testing a total of 3 samples per mix design were cast in Styrofoam moulds. These Styrofoam moulds had the same dimensions of 40 mm width, 40 mm height and 160 mm length. All 9 mix designs were tested for the flexural strength tests.

Samples were stored for 27 days in a fog room at 20 °C and >95% RH before testing. Additionally, the samples were heated a day before testing at 250 °C for 2 hours at that temperature with a heating rate of 20 °C/min in a BOF 1100 Carbolite Furnace with a Eurotherm 3208 Temperature Controller. This step was done to simulate what the mechanical properties would be at the point of spalling, which is estimated to be 250°C at the location of spalling. By heating the entire sample to 250 °C for 2 hours, the degradation is simulated with the accompanied melting of pp fibres.

However, while the controller indicated the oven was at 250 degrees for 2 hours. The samples after heating seemed to indicate a lower temperature. PP fibre can still be observed on the surface of the _05 and _10 samples. This suggests that the oven temperature was actually lower than the melting temperature of the fibres, which is 170°C for polypropylene fibres.

After heating they were kept at room temperature in the lab for an additional day until testing.

3.3.3 Elastic modulus

Elastic modulus setup and testing was done according to NEN-EN 12390-13 [68]. Testing was done using an Instron 8872. The stabilized secant elastic modulus was measured after 3 load cycles with a maximum loading of 9 kN. Testing was loading controlled with a loading rate of 0.1 kN per second (0.063 MPa/sec). The loading rate is less then the prescribed 0.2 MPa/sec according to NEN-EN 12390-13 [68]. This choice was preferred, to ensure safe use of the Instrom as it's loading nears it's maximum capacity (9.5 kN).

Gauges were glued with Pedikit 860 to all 4 sides of the samples with an initial length of 60 mm parallel to the vertical surface. Sandpaper was used to level the the top and bottom surface.

The stabilized secant elastic modulus was calculated according to the formula provided in NEN-EN 12390-13 [68]:

$$E_{cs} = \frac{\Delta\sigma}{\Delta\epsilon_s} \tag{3.1}$$

In which E_cs is the stabilized secant elastic modulus. Delta-sigma$\Delta\,\sigma$ the change in stress, $\Delta\,\epsilon_s$ the strain of the sample. $\Delta\,\epsilon_s$ is calculated in the following way, in accordance with NEN-EN 12390-13 [68]:

$$\Delta\,\epsilon = \frac{\Delta\,L}{L_0} \tag{3.2}$$

In which $\Delta\,L$ is the change in length, and L_0 the initial length of the gauge, 60 mm.

TABLE 3.6: Elastic modulus results

Sample	Elastic Modulus [GPa]	Test 1 [GPa]	Test 2 [GPa]	Test 3 [GPa]
30_00	42.8	40.4	42.6	45.4
30_10	42.9	41.3	44.5	42.9
40_00	35.2	35.0	36.1	34.5
40_10	34.6	33.8	35.4	34.6
50_00	30.7	31.5	30.2	30.4
50_10	28.4	26.8	29.3	29.0

Elastic modulus for the untested samples was then estimated based on the compressive strength ratio between the sample with similar W/C ratio and the tested elastic modulus. The calculation was done by using the elastic modulus _10, divide it by it's compressive strength and multiply it with the _05 compressive strength.

3.3.4 Flexural strength

Flexural strength setup and testing was done according to NEN-EN 12390-5 [69]. Tests were performed using a three point bending setup with a centre top load and 2 rollers at the bottom. The bottom rollers having a distance of 120 mm between them. Notches of 3 mm were applied to the bottom in the middle of the sample to ensure the cracking happens in the middle area. Two gauges were glued to both sides of the bottom part to measure the strain. Testing was done displacement controlled using the crack width from the applied gauges.

The second test for the 30_10 samples failed due to slipping of the gauge causing the Instrom to quickly overload and break the sample. Consequently, this sample is disregarded for the results.

TABLE 3.7: Elastic modulus estimation based on compressive strength of samples

Sample	Elastic Modulus [GPa]	Compressive strength [MPa]
30_00	42.8	68.30
30_05	41.39	66.01
30_10	42.9	70.38
40_00	35.2	47.18
40_05	33.75	42.11
40_10	34.6	43.14
50_00	30.7	39.53
50_05	28.8	38.58
50_10	28.4	37.96

Flexural strength was calculated according to the formula provided in NEN-EN 12390-5 [69]:

$$f_{ct,fl} = \frac{3 * F * l}{2 * d_1 * d_2^2} \tag{3.3}$$

In which F is the force, l the length between the two bottom rollers, d_1 the width of the sample, and d_2 the height of the sample.

TABLE 3.8: Flexural strength results

Sample	Flexural Strength [MPa]	Test 1 [MPa]	Test 2 [MPa]	Test 3 [MPa]
30_00	5.50	5.69	5.60	5.21
30_05	5.27	5.16	5.10	5.55
30_10	4.90	5.13	Failed	4.68
40_00	3.88	4.12	3.50	4.04
40_05	4.49	4.76	4.23	4.49
40_10	4.14	4.37	4.08	3.98
50_00	3.70	3.66	3.93	3.50
50_05	3.60	3.86	3.71	3.24
50_10	3.40	3.61	3.38	3.22

3.3.5 Air content testing

Air content tests were performed using a Form+Test Prufsysteme Air Entrainment Meter according to the standard NEN-EN 1015-7:1998 [71]. The test was decided to perform after large air pores were detected through the CT scanning results for the lower W/C ratio samples.

1L of mortar was prepared according to the mix designs of Table 3.3 and 3.4. The mortar was then placed inside the metal cylinder and vibrated the same time as the mix design was done. After vibration the surface of the mortar was leveled to the same height as the cylinder edge, see Figure 3.5. The air content meter was then placed on top of the cylinder block and closed using the front and back handle, see Figure 3.6. Tap water was added until the water was overflowing from both side holes on top, the holes were then subsequently closed. The air content meter was then pressurized by pumping the black handle on top until set at 0%.

Air content test is then commenced by pulling the metal lever on top of the meter. Air content can then be read from the meter as a percentage value of the 1L. Results are given in Table 3.9.

A single second test was performed to see how the vibration time influences the air content of the mortar. The vibration time was changed from 10 to 30 seconds, with positive results on the air content as seen in the last row of Table 3.9. However, after some consultation with Technicians around the TU Delft lab[55], it was decided that the reduced air content does not weigh up against the adverse effects. Mainly that the aggregate and cement can get segregated, with the aggregate settling down at the bottom and the cement plus water and superplasticizer rising to the top surface. Stating that an air content of around 4% is not that strange for mortars with low W/C ratio and superplasticizer and pp fibre added, as they both have an air entraining effect.



FIGURE 3.5: Mortar prepared in cylinder for air content test



FIGURE 3.6: Full setup of air content test

TABLE 3.9: Air content of samples

Sample	Air content (%)
30_00	4.8
30_05	4.3
30_10	4.1
40_00	3.0
40_05	3.4
40_10	4.6
50_00	0.8
50_05	1.8
50_10	2.2
30_00 retry	4.6
30_05 retry	4.2
30_10 retry	4.4
30_10 Longer vibration	3.8

Chapter 4

Thermal Shock Resistance: Spalling Behaviour

To research the spalling behaviour of the samples, it was chosen to set up an experiment in which different samples with varying mix designs were subjected to different heating rates.

Four factors were chosen to be the most influencing on the spalling behaviour. Namely, the pp fibre ratio, the W/C ratio, the heating rate and the volume/surface area ratio. These four factors were divided into two experimental series. First series will research the influence of the pp fibre ratio and the W/C ratio. The second series will research the influence of the volume/surface ratio. Both series will use a varying heating rate.

This chapter will cover both experimental series and report the findings and encountered difficulties during testing. The goal being to illustrate the effect of all the different parameters on the spalling behaviour of cement based materials.

4.1 High temperature (HT) experiments: W/C and PP Fibre Ratio Influence

In the first series of HT experiments the influence of the W/C and pp fibre ratio. Samples were cast according to the mix design specified in Section 3.2, Table 3.2.

4.1.1 Sample preparation

Samples were taken out of the fog room to the oven room. Pictures were taken from different angles for each sample, and the weight was measured. Sample dimensions were of 65 mm height and 55 mm diameter, as specified in Section 3.2.

The samples had a variety in maturity of a couple of days when tested, as there is limited use of the oven per day, and casting was decided to do all on the same day because of COVID regulations. The aim was to test every sample at a maturity of +/- 28 days with a an allowable variation of 2 days. This was not achieved as the oven needed to be repaired when maturity was reached. As a result the maturity was readjusted to +/- 56 days.

4.1.2 Oven setup and procedure

Samples were placed inside an open element HTF1700 Carbolite Furnace with an Eurotherm 3208 temperature controller. A protection cage was placed over the sample to protect the exposed heating elements. Maximum temperature was set at 600

°C. Heating rates of 10, 30 and 50 °C/min were used. Then, depending on the temperature gradient, different setups for the dwell time were used.

With a 50 °C/min temperature gradient, a dwell period of 30 minutes was used, while the total heating up time to achieve 600 °C was approximately 12 minutes (start at room temperature 20 °C).

Samples tested with a heating rate of 30 °C/min, the dwell period was set at 18 minutes, while the heating up phase was around 20 minutes.

Lastly, for the 10 °/min samples, the dwell period was 6 minutes, while the heating up time was around 58 minutes.

After performing a couple of tests, an extra procedure to the oven tests was added. Namely, that when loud spalling is heard, the heating was turned off. This was done to protect the open heating elements of the oven. During the first experiments it was discovered that the cage can be blown off of the sample if a big piece of mortar spalls off. Consequently, it was decided to terminate the experiments when spalling is initiated to ensure no damage is caused to the open heating elements.

4.1.3 heating rate variation

Problems were observed during the oven experiments with the heating rate. While the average heating rate was correct over the entire period, the per minute heating rate varied. This was especially apparent for the 10 °C/min, as the heating rate is much slower. For higher heating rates the change in heating rate was observed to be less variable.

The heating rate per minute were written down for the 40_00 leading up to the spalling, see 4.1. As can be read from the table, the spalling happens at a higher heating rate than was programmed.

TABLE 4.1: Per minute heating rate for 40_00 sample at 10 °C/min experiment

Starting temperature	End temperature	temperature difference/gradient
491 °C	512 °C	21 °C
512 °C	534 °C	22 °C
534 °C	527 °C	-7 °C
527 °C	541 °C	14 °C
541 °C	spalling	-

To further elaborate on the findings, while the 10 °C/min is true for the average of the total heating time, the heating rate on a per minute basis can go up to 20 °C/min. Spalling also happens around these heating rate rises, questioning the experimental setup and whether this should be considered spalling at 20 °C/min instead of 10 °C/min.

A possible explanation for the behaviour of the oven is that the heating elements can only be heated at a specific power, consequently only able to radiate heat at one level. To control the heating rate, the elements will turn off and on to control it. It can be observed that the controller starts heating and shuts off during the experiments depending on the heating rate. It is believed that the controller will heat up to a certain temperature rate. After it passes this threshold, it will stop heating, until it again passes a lower threshold to start heating again.

This allows the oven to maintain the programmed heating rate for the entire program, but fluctuate on a per minute basis.

4.1.4 HT experiments: results

In Table 4.2, 4.3 and 4.4 the results are presented for the HT experiments. Not all samples were tested due to limited testing time. Specific samples were chosen to test to get the most representative overview of the samples. This choice was decided upon the results of the _05 sample at each different heating rate. If the sample spalled, then the _10 sample would consequently be tested at the same heating rate. If no spalling was observed in the _05 sample, the _00 sample would be tested at the same heating rate.

It should be noted that is that the fog room was not functional for 2 weeks. When the 30 samples were tested, these came out in different conditions then the usual 20 degrees >95% RH conditions of the fog room. Meaning that the 30 samples were kept for 10 days in different conditions leading up to the testing. The fog room was repaired the following week, giving the 40 samples 3 or more days of saturation time in optimal conditions before testing, and the 50 samples 10+ days.

TABLE 4.2: Results 30 samples

Sample	heating rate	Maturity	Spalling time	heating rate	Maturity	Spalling time	heating rate	Maturity	Spalling time
30_00	10°C/min	58 days	51 min(530°C)	30°C/min	57 days	20(595°C), 23 min(607°C)	50°C/min	57 days	12(545°C), 21 min(607°C)
30_05	10°C/min	-	-	30°C/min	58 days	No spalling	50°C/min	58 days	No spalling
30_10	10°C/min	-	-	30°C/min	-	-	50°C/min	57 days	No spalling

TABLE 4.3: Results 40 samples

Sample	heating rate	Maturity	Spalling time	heating rate	Maturity	Spalling time	heating rate	Maturity	Spalling time
40_00	10 °C/min	68 days	54 min(541°C)	30°C/min	-	-	50°C/min	56 days	11, 18, 19 min(all 600°C)
40_05	10°C/min	61 days	No spalling	30°C/min	61 days	20 min(580°C)	50°C/min	56 days	15 min(580°C)
40_10	10°C/min	-	-	30°C/min	61 days	No spalling	50°C/min	56 days	No spalling

TABLE 4.4: Results 50 samples

Sample	heating rate	Maturity	Spalling time	heating rate	Maturity	Spalling time	heating rate	Maturity	Spalling time
50_00	10°C/min	56 days	54(570°C), 57 min(570°C)	30°C/min	-	-	50°C/min	-	-
50_05	10°C/min	56 days	No spalling	30°C/min	55 days	18(550 °C), 26 min(600°C)	50°C/min	55 days	11(550 °C), 12 , 13 min(600°C)
50_10	10°C/min	-	-	30°C/min	56 days	No spalling	50°C/min	55 days	No spalling

4.1.5 Spalling behaviour

The most notable results and observations will be discussed in this section accompanied with figures from the tests. A complete overview with all the oven results figures is presented in Appendix A.

First observation made during the experiments is that when the samples are subjected to a lower heating rate, the type of spalling changed.

The lower the heating rate, the larger the spalling pieces were. This is relative to the fibre content, meaning in practice that larger spalling pieces occur at heating rates of 30 °C/min for 0.05% samples and 10 °C/min for the 0.00% fibre samples. The behaviour could be observed for the 30_00 samples between 10 °C/min and 50 °C/min, but also for the 40_05 and 50_05 samples at 30 °C/min and 50 °C/min. This behaviour was accompanied with much louder spalling sounds at the lower heating rates and the possibility of the cage going up in the air (see figure 4.1), displaying the forces generated with spalling.

Figure 4.2 and Figure 4.3 show the difference in behaviour for the 0.30 W/C ratio with 0.00 % fibre at different heating rates. The pieces at a heating rate of 50 °C/min are broken in lots of little small pieces, almost becoming pulverized, while the sample at 10 °C/min shows 2 big chunks of mortar that spalled off.

;



FIGURE 4.1: Spalling forces lift the protection cage off the sample



FIGURE 4.2: Spalling 30_00 at 50 °C/min



FIGURE 4.3: Spalling 30_00 at 10 °C/min

Figure 4.4, 4.5, 4.6 and 4.7 show the difference for the 40_05 samples at 50 and 30 °C/min. Again, a clear difference in the spalling behaviour. The sample at a heating rate of 50 °C/min shows that the heating rate generated a multitude of small spalling pieces. While the sample at a heating rate of 30 °C/min showed a disk shaped pieces that came of in it's entirety with a smaller side chunk and some little spalling pieces. Figure 4.7 shows a complete overview of the pieces collected from the 0.40 W/C ratio at 30 °C/min.



FIGURE 4.4: Spalling pieces 40_05 at 50 °C/min

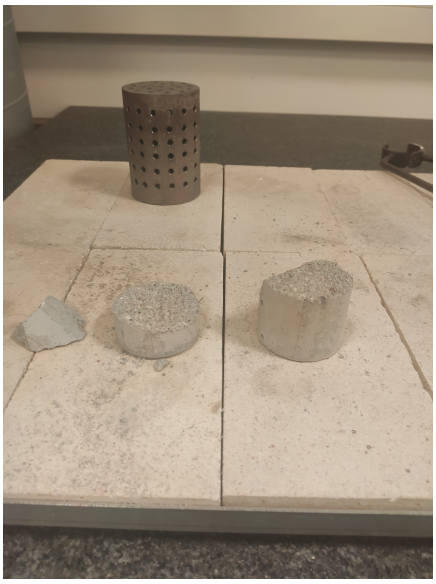


FIGURE 4.5: Spalling pieces 40_05 at 30 °C/min



FIGURE 4.6: side view of the spalling damage for the 40_05 sample at 30 °C/min



FIGURE 4.7: Overview of spalling pieces for the 40_05 at 30 °C/min

The 50_05 sample once more exhibit the difference in spalling behaviour. Figure 4.8 shows a large collection of small pieces collected at 50 °C/min. Clearly displaying the effect of a higher heating rate, and how the mortar reacts with smaller spalling pieces.

Figure 4.9 shows some small pieces and a large disk that spalled of the top at 30 °C/min heating rate. Spalling sounds were heard twice for the given heating rate, and it is suspected that the first spalling sounds at 18 minutes were from the small pieces at the top surface, as the sound was quite soft. The second spalling sound was much louder, contributing to the suspicion that this was the larger disk piece.

Consequently, it is thought that both shallow and deep spalling can happen in a sample, provided that the core is still largely intact for big spalling pieces to happen. However, with the current results the observation is inconclusive at most with only one result displays both shallow and deep spalling.



FIGURE 4.8: Overview of spalling pieces for the 50_05 at 50 °C/min



FIGURE 4.9: Overview of spalling pieces for the 50_05 at 30 °C/min

Big spalling pieces are also observed for the 40_00 and 50_00 samples at 10 °C/min, but no tests were done at higher heating rates to compare with because of time constraints with the use of the oven. However, results and findings from previous research[49, 58], it seems very plausible that both samples would have shown similar smaller spalling pieces as the heating rate increases.

An additional and especially interesting result was found with the 40_00 sample at 10 °C/min. The piece that spalled off stayed intact perfectly on the outside and could be fitted back onto the sample with some small missing pieces, shown in Figure 4.10 and Figure 4.11.

Furthermore, upon inspection of the inside another observation was made on the spalling behaviour. Namely that both pieces exhibited a hollow core, as seen in Figure 4.12 and Figure 4.13. Displaying that the core underwent quite some damage when the sample underwent spalling. The core spalled into lots of little pieces, almost pulverising the core. Showing that while the outside stays almost entirely intact for both the spalled off piece and the original sample, the core shows severe damage.

Reexamining previous results, similar observations can made with the 30_00 sample at 10 °C/min (see Figure 4.14 and 4.15), but a little less clear. The sample displays a similar hollow core, but not with a two section that can be fitted back on together. Additionally, the pulverised mortar is still partly residing in the hollow core when taken out of the oven, displaying the created fineness from the spalling.



FIGURE 4.10: Spalling pieces for the 40_00 at 10 °C/min fitted together

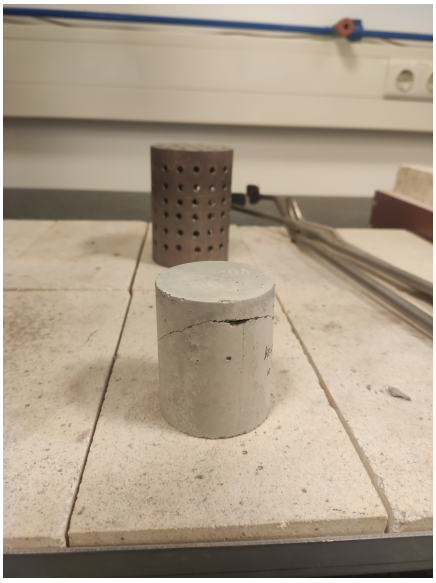


FIGURE 4.11: Spalling pieces for the 40_00 at 10 °C/min fitted together

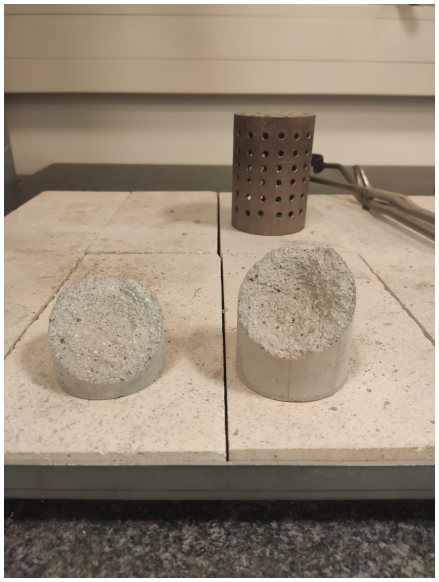


FIGURE 4.12: Hollow core for the 40_00 at 10 °C/min



FIGURE 4.13: Hollow core for the 40_00 at 10 °C/min side angle



FIGURE 4.14: Spalling pieces of W/C 0.30 sample with 0.00% at 10 °C/min heating rate



FIGURE 4.15: Spalling pieces of W/C 0.30 sample with 0.00% at 10 °C/min heating rate

A possible explanation for the observed spalling behaviour is that spalling at higher heating rates is caused by a one sided or two sided moisture clog close to the surface, while at lower heating rates the moisture clog meets in the middle from multiple sides.

A more extensive explanation is that at lower temperatures the pore pressure does not exceed tensile strength of the sample at the surface. Consequently, the moisture clog moves further inside as the heating progresses. As the heating progresses further inside the concrete, there comes a certain point the moisture clog from all heated surface sides(viewed from a 2D standpoint from top, left and right for the tested samples), meet in or around the core of the sample. Consequently, while the previous pressure build-ups were all sufficient and below the tensile strength of the samples, the combined stresses from the pore pressure exceed the tensile stress of the sample, causing spalling deep inside the specimen and large spalling pieces while pulverising the core.

An additional influence is thought to be the temperature gradient. Shallow spalling with small pieces is believed to be a mostly thermo-hygral dominant mechanism, while the deeper spalling becomes a combination of both thermo-mechanical and thermo-hygral spalling. Similarly to the moisture clog, the heating gradient is also thought to combine in the middle from multiple sides.

4.2 HT Experiments: Recast 30 samples

4.2.1 HT setup recast samples

Retesting of the 30 samples were done in a different oven due to emerging problems with the previously used oven.

Mainly, the problem being that the small cement pieces that spalled off and dispersed through the oven, started melting through the insulation when other experiments were performed that went up to 1200 °C. This is a progressive damage, causing large holes to appear inside the oven over time. Consequently, it was decided to halt further testing inside the original oven and instead offered an alternative oven was used.

The new oven was a closed element BOF 1100 Carbolite Chamber Furnace with a Eurotherm 3208 controller. The samples were placed on a separate insulation stone to make it easier to replace the insulation when it is possibly damaged. Similar to the previous experiments, the samples were put inside the oven with a steel protection cage.

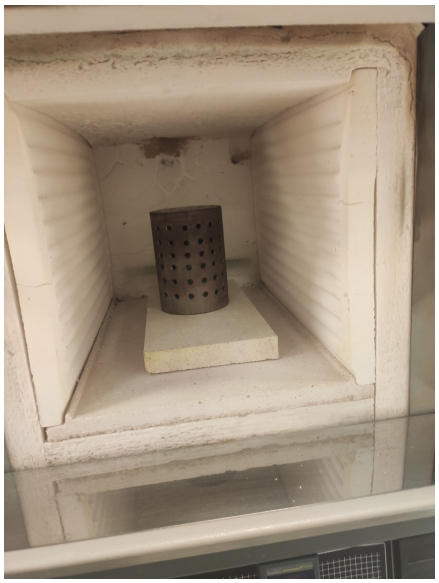


FIGURE 4.16: Oven setup BOF 1100 Carbolite Chamber Furnace with cage



FIGURE 4.17: Oven setup BOF 1100 Carbolite Chamber Furnace

In terms of safety, the new oven is an improvement as the heating elements were protected by the thermal insulation. However, because of this protection, there was a delay between the heating element temperature and the actual inside oven temperature. Moreover, to reach the desired heating rate until 600 °C, the heating elements needed to heat up to 700 °C or even 850 °C for 25 °C/min. If not done, the heating rate fell off at higher temperatures as it came closer to the maximum temperature. Meaning that the heating rate would be lower than the desired heating rate.

Consequently, it was decided to measure the temperature of both the heating elements and the oven temperature and the subsequent acquired heating rate. The Eurotherm 3208 controller is able to measure both temperature values, which were used to determine the acquired heating rate per executed experiment. Measured temperatures and heating rates for the four experiments performed are presented in Figures 4.18-4.21. On the left Y-axis both the element and oven temperature are presented against the time. On the right y-axis the subsequent heating rate is presented against the same time interval.

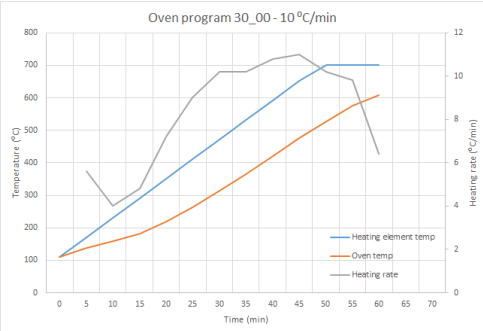


FIGURE 4.18: Heating program for 30_00 at 10 °C/min

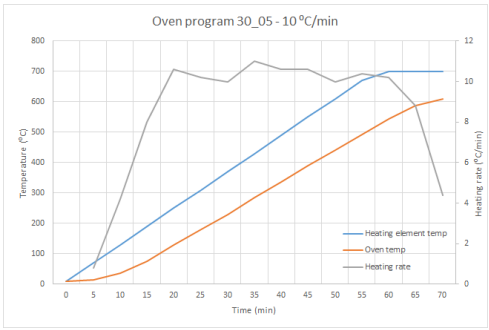


FIGURE 4.19: Heating program for 30_05 at 10 °C/min

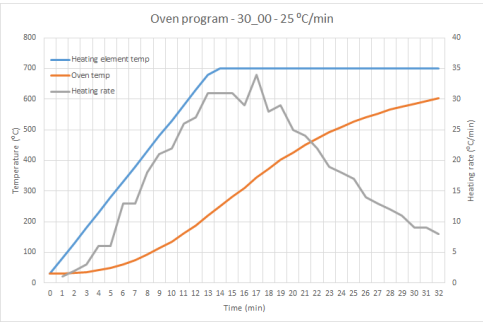


FIGURE 4.20: Heating program for 30_00 at +/- 25 °C/min

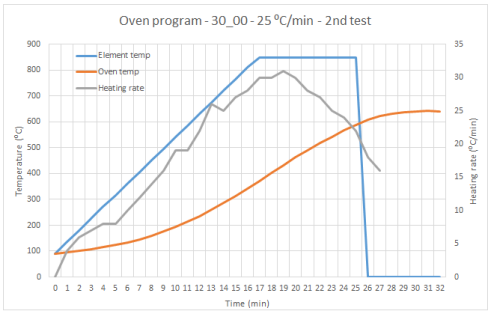


FIGURE 4.21: Heating program for 30_00 at +/- 25 °C/min

As can be seen from the figures, there is quite a difference between element temperature and the oven temperature. Additionally, this difference changes with different heating rates. Consequently making it difficult to run the correct program with the desired heating rates without falling off in heating rate at the end of the program. Moreover, because of this difference, the initial heating rate is lower than the desired heating rate.

If the maximum temperature was too low, the heating rate fell below the required heating rate at the end of the heating program as can be seen from Figure 4.20. Displaying that the end temperature of 700 °C for the heating elements is insufficient as the oven heating rate slowed down after reaching a oven temperature of 450 °C. As a consequence of this, a second experiment was performed using an end temperature of 850 °C to compensate for it.

4.2.2 Recast spalling results

Recast samples were tested again at approximately 8 weeks. More specifically at 58 and 59 days. Results of the testing is presented in Table 4.5.

TABLE 4.5: Results recast 30 samples

Sample	heating rate	Maturity	Spalling time	heating rate	Maturity	Spalling time	heating rate	Maturity	Spalling time
30_00	10°C/min	58 days	No spalling	25-1°C/min	59 days	No spalling	25-2°C/min	59 days	No spalling
30_05	10°C/min	58 days	No spalling	30°C/min	-	-	-	-	-
30_10	10°C/min	-	-	30°C/min	-	-	-	-	-

No spalling was observed as can be seen from the results. Compared to the previous experiments in the other oven, some influences are thought of as the cause

of the samples to not spall, while they did spall in the other oven. It is believed to be caused by either one or more of the following reasons:

1. Lower heating rate at the beginning of the heating program. When the heating program is initiated, the oven needs time to properly heat up and get to the right heating rate. The first minutes will already be at an elevated temperature while the heating rate was still low. It's known from arresting hydration using oven drying that moisture already starts to leave the sample at temperatures of 40 °C. Consequently, with the current heating program, the moisture inside the sample has more initial time to escape at the start of the experiment while the heating rate is still lower than the desired heating rate.
2. Additional heating through radiation is present besides convection heating through the air. The open elements cause heating through radiation, besides the convection heating in both ovens. Even though the temperatures are the same inside the oven, the radiation heating will cause the sample to heat up quicker inside the oven. Meaning that the disparity between oven temperature and sample temperature is lower.
3. Fluctuation effect causes additional thermal gradient forces inside the sample. The HT1700 oven had a fluctuation effect that is not present with the current oven. It is possible that this fluctuation causes an increased heating gradient inside the sample. Consequently, an increase in the thermal mechanical mechanism is caused.
4. The HT1100 oven was not working properly, and the given temperatures in the oven are incorrect.The oven temperature might be lower than is represented by the controller. As a consequence, the temperature could be a lot lower than is obtained at the given heating rate.

As a consequence of these results, it was decided to terminate the volume/surface testing at different heating rates as the oven was deemed insufficient for the experiments. Furthermore, the determined volume/surface ratio's that are useable are lower than the tested 30 samples. This would already theoretically mean no spalling reactions in any of the proposed samples, while larger samples were not possible due to the dimensions of the protection cage.

4.3 HT Testing: Volume/Surface Influence

Unfortunately, this experimental series was terminated due to the issues mentioned in the previous section with the heating rate. However, the proposed experimental series are still believed to be relevant for future research.

Dimensions for the experiments are shown in Table 4.6. The goal was to keep the volume values exactly the same while varying the surface area. The proposed samples would then be subjected to identical heating rates as the first experimental series.

TABLE 4.6: Volume/Surface samples proposal

Height(mm)	Length (mm)	Width (mm)	Volume(mm^3)	Surface (mm^2	Volume/subj surface (mm)
50	50	40	100000	13000	9.09
40	50	50	100000	13000	9.52
80	25	50	100000	14500	7.54
100	50	20	100000	16000	6.67

4.4 Discussion and Conclusions

While unable to emulate different spalling behaviours among varying W/C ratios with different heating rates and pp fibre ratios, a number of other observations and conclusions were made using the spalling experimental results.

- The heating rate has shown to not only influence the spalling behaviour, but also the type of spalling, confirming results from other research. A higher heating rate creates spalling closer to the subsurface, with less force and smaller spalling pieces. While a lower heating rate will cause a deeper and more explosive spalling with larger spalling pieces. Another way to describe it, is that the spalling becomes deeper the closer it gets to the heating rate that will not cause spalling. Large chunks were observed for 30 °C/min with 0.05%, the same way for 10 °C/min with 0.00% fibre. Meaning that the closer the mix gets to the point being spalling free, the deeper the spalling gets.
- 0.10% pp fibre was found to be sufficient to mitigate spalling with the used dimensions for all samples. It increases the pore connectivity in the sample when heated more than enough to prevent spalling at all heating rates.
- 0.05% pp fibre was only sufficient at lower heating rates. Showing that it will only mitigate spalling at a heating rate of 10 °C/min (possibly 20 °C/min considering the heating rate variation).
- For the sample 40_0 and 30_0 at 10 °C/min a hollowed out core was observed, while the outside remained mostly intact. It is thought that this was caused by a multi-sided thermo-hygral-mechanical mechanism. Both the temperature gradient and pore pressure combining and meeting in the middle of the sample cause a large build-up of pressure. Which showed the core to pulverise while keeping the outside intact.
- The use of a different oven posed some obstacles in the experimental campaign. It was not possible to research the volume/surface influence due to this adjustment. Results would not have been representative in relation to the results acquired in the other oven. It did raise the question whether there is not only an influence in the temperature but also in the way samples are heating. Mainly, if there was a combination of convection and radiation, or only convectional heating. This could be further questioned with the influence of heating through conduction.

Chapter 5

Characterization of the Pore Structure

This chapter is dedicated to the characterization of the pore structure. To analyse the pore structure of the mortar samples, CT and MIP technique were used.

The main use of the X-ray Computed Tomography (CT) is to analyse the bigger pores, more specifically the large capillary pores and air voids in the mortar samples. The possible pore dimensions range in the micrometer scale, from 6 µm upwards.

The Mercury intrusion porosimetry (MIP) is used to analyse the smaller pores, ranging in the nano scale. This is in the range from the capillary to the gel pores, between 7 nm and 400 µm.

By combining the CT and MIP, the objective is to get a total assessment of the pore structure from the nano to milimeter scale. The goal being to assess the porosity and pore size distribution with the combination of both techniques. The results will then be compared to the results of the thermal shock resistance experiments in Section 4.1 and look for possible influences on each other.

Additionally, the pore connectivity will be analysed through the CT scans using a tortuosity script and try to find a possible connection between the results. The same will be done to assess the pore connectivity through the MIP results. Again, both results will be evaluated in relation to the spalling behaviour.

5.1 X-Ray Computed Tomography

5.1.1 Sample preparation

To prepare the samples for CT scanning, additional coring had to be done to fit the samples inside the CT scanner and to improve the voxel size of the images.

From the original 55 mm diameter and 65 mm height samples, cores were taken, with a diameter of 12 mm and 20 mm height. After coring they were placed in a SECADOR desiccator to stop hydration. Coring was done after 57 days for the 30 samples, 50 days for the 40 samples, and 43 days for the 50 samples.

The difference in maturity is a result of the CT scans all done in a two day interval as to difficulties with scheduling around the lab. While not ideal, it still gave a more than sufficient indication of the pores and air voids in the samples as the samples are beyond the initial hardening stage.

After 5 days in the desiccator the samples were submerged in a Potassium Iodine solution, to improve the contrast for the CT images. The solution contained 0.83 grams of Potassium Iodine per 100 ml of water, combined together in a flask. After combining, the solution was mixed with a magnetic mixer for 10 min at 500 RPM.

When the mixing was done, all 9 samples were submerged in the solution and stored airtight for 2-3 days.

After storing for 2-3 days, the last preparation was done for the CT scans. Samples were removed from the solution and wrapped in plastic foil. To fit inside the CT scanner, the wrapped samples were fitted inside a plastic tube. This plastic tube was then placed inside the Micro CT scanner.

5.1.2 Setup, equipment and procedure

Micro-tomography scans were performed using a Phoenix Nanotom X-ray CT scanner. The machine consists of a transmission type x-ray tube, a sample stage and a 3072 x 2400 flat panel detector with a pixel size of 100 µm. The transmission target uses a tungsten filament and possesses a maximum accelerating voltage of 185 kV. The acquisitions were performed at 100 kV.

Samples were placed at a distance of 25.99 mm from the transmission tube and 199.99 mm from the detector. A magnification of 7.69 was acquired, achieving a 6.499 µm voxel size. Each voxel contains 16 bits and displays a grey scale depending on the density of the passed through element.To improve the resolution, part of the sample height is left out of scan. Total scanned height was 14.96 mm. Reconstruction was done using Datos VeloCT. Additionally, a median filter was applied through VGStudio Max 3.0. Figure 5.1 and Figure 5.2 show the setup of the sample and the used micro tomography scanner.



FIGURE 5.1: Sample inside CT scanner (detector not placed yet)

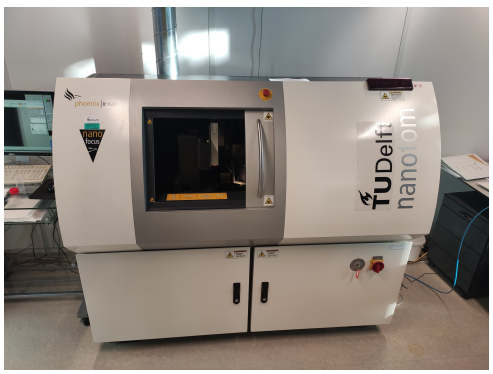


FIGURE 5.2: Phoenix Nanotom CT scanner

5.1.3 Processing of CT data - ImageJ/Fiji

The CT results were processed using the Freeware software ImageJ/Fiji. To only have mortar in the analyzed frame, a circle had to be specified that consists only of the sample and not the background area. This specified circle is smaller than the initial sample diameter as there was a slight misalignment between the top and

bottom part of the sample, causing the circle to move outside of the sample into the background area. To address this problem, the circle is smaller than the initial sample diameter, keeping the circle inside the diameter. Additionally, part of the top and bottom was cut off because of visible noise in the images.

The resulting specified area was 10.73 mm in diameter for all samples. Due to the presence of ring artefacts a large number of images were considered insufficient. In total 1520 images were chosen to be sufficient for the image stack, which equals to a 9.87 mm height.

The specified image stack was analysed using the Trainable Weka Segmentation plugin in ImageJ. The plugin is used to segment all the pores, air voids and fibres out the mortar. After segmentation, an image is created which has divided the image in the specified segmented classes. Namely, pores/voids/fibres, large/dark aggregate, small/light aggregate, cement and background. The voids and fibres are then filtered out using a threshold, resulting in a black and white image that consists only of the pore and fibre structure of the sample.

To achieve the segmentation the plugin first has to train a classifier that will separate each class using only the mean training feature. The classifier was first trained on an image stack of 10 images. After assessing the classifier as sufficient, it was applied on the total image stack of 1520 images.

It was observed during processing of the samples that correctly segmenting the cement and aggregate interface was difficult to achieve. However, this had no influence on the segmented pores. Consequently, it was decided to disregard the aggregate and cement problems for the chosen analysis as the region of interest is the pore structure.

Additionally, there was a remark on the segmented pore structure as well. It was found that during segmentation for some of the stacks that either the fibres would not fully be recognized as part of the pore structure, or noise would occur in the form of pores that are not present in the original image. The noise becoming more problematic when the classifier was changed from a short image sequence with 10 images to the total image stack containing the entire specified volume.

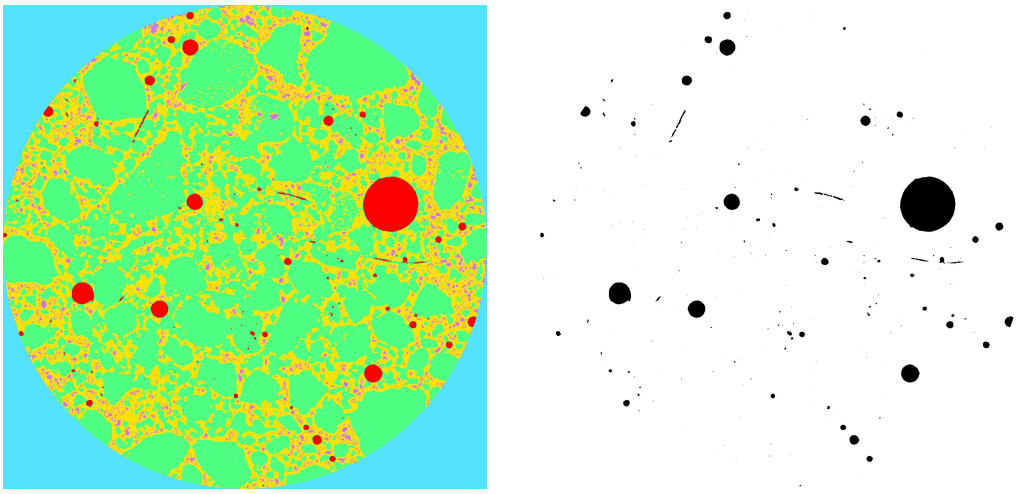
The decision was made to keep the noise, and fully incorporate the fibres. The noise spots will only take up a small amount of the volume space, and can possibly be removed later on when analysing the pore size distribution by removing the smallest measured sizes.

Moreover, what this decision will gain is fully segmented fibres that will allow the analysis of the pore connectivity to be most effective. While the random spots are believed to not contribute much to the pore connectivity as they are observed to be mostly isolated, and thus too small to connect voids and fibres with each other.

5.1.4 3D analysis - ImageJ/Fiji

The 3D view for each segmented pore volume is presented in Figures 5.4 - 5.12. The 3D reconstruction was done using the BoneJ in ImageJ [28]. The 3D images were reconstructed using the segmented black and white image stack of the pore structure. The resulting image stack and consequently the presented 3D figures are 10.73 mm in width and 9.87 mm in height. The images were tried to be presented as clear as possible, but some difficulties are still observed due to the amount of pores and the random observed spots due to segmenting choices.

The different 3D view figures show quite a large difference between the amount of visible voids and fibres. The 30 samples contain the largest amount of air voids



(A) (B)

FIGURE 5.3: (A) Segmented image divided in 5 classes. Red: pores/fibres, green: large/dark aggregate, small/light aggregate, yellow: cement, blue: background. (B) Black and white 2D view of the pore structure as a result of segmentation

in the 3D view, followed by the 40 samples and then the 50 samples. This result is counter intuitive on the belief that samples with lower a W/C ratio have a lower porosity. The cause of the higher porosity in the 30 samples is believed to be the combination of superplasticizer and pp fibres. In which the superplasticizer has an air entraining effect, and the pp fibre an effect on the workability. Consequently needing more superplasticizer as more fibre is used.

With the 40 samples the cause is believed to be a reduced workability. In addition, it can be observed that there is a big difference in porosity among the 40 samples. Focus was on not using too much superplasticizer and the workability was considered enough when the samples were cast. However, upon review of the results there seems to be a clear increase of porosity with additional pp fibre. It is known that pp fibre reduces workability, which indicates that the reduced workability increases the porosity.

In terms of fibre orientation it was observed that the 30 and 40 samples show an orientation in multiple directions, while the 50 sample start to display a horizontal alignment of fibres. Besides the horizontal alignment, the 50_10 sample show an agglomeration of fibres seen at the bottom of the sample.

The agglomeration of fibres iwas believed to be caused by the shorter mixing times of the sample, as the dry and wet mixing was completed in a shorter time interval. A solution to this problem could be to lengthen the dry mixing time or to disperse and separate the pp fibres more from one another before adding to the mix.

The alignment perpendicular to the casting direction, is the result of the better workability, caused by less internal friction between cement, aggregate and fibres [17]. This horizontal alignment happens during the vibration process as the fibres can move easier between the aggregate and cement by the described lower internal friction between them. This could either be a positive or negative effect for the thermal shock resistance, depending on how the structure is used/analysed.

To further elaborate on if the alignment perpendicular to the casting direction is positive or for the vapour molecules. One thought process is that a single orientation can help the vapour to either pass easier to the outside of the concrete or easier

past the moisture clog inside the concrete. Consequently, limiting the thermo-hygral reaction inside the concrete. However, the alignment should then be in the direction of the heated surface area for it to be effective, which could be problematic for floors and other horizontally cast elements. This can either be

The other thought process is that a multi-directional orientation allows the water vapour to move in all directions, and thus provide better thermal shock resistance in different sides or multiple sided heating.

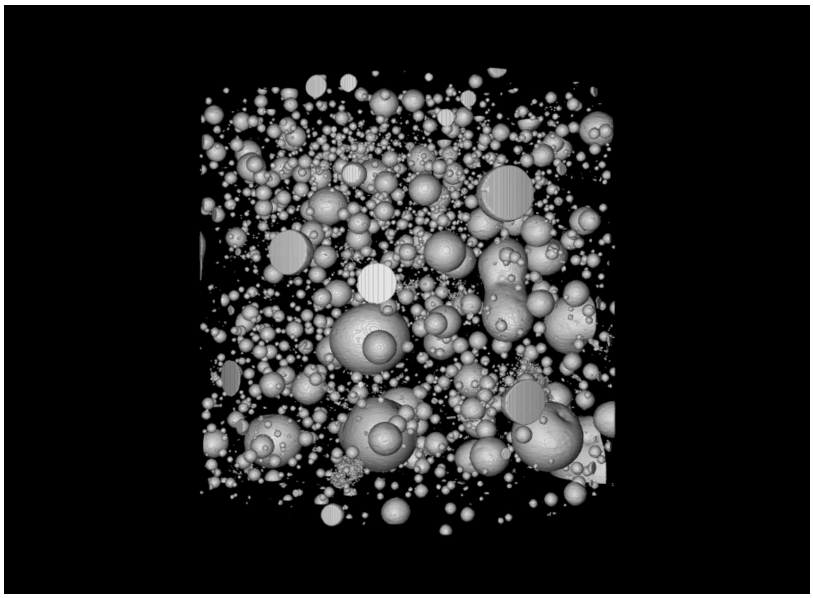


FIGURE 5.4: 3D view of the pore space in the 30_00 sample through ImageJ. Large air voids can be observed in the pore structure.

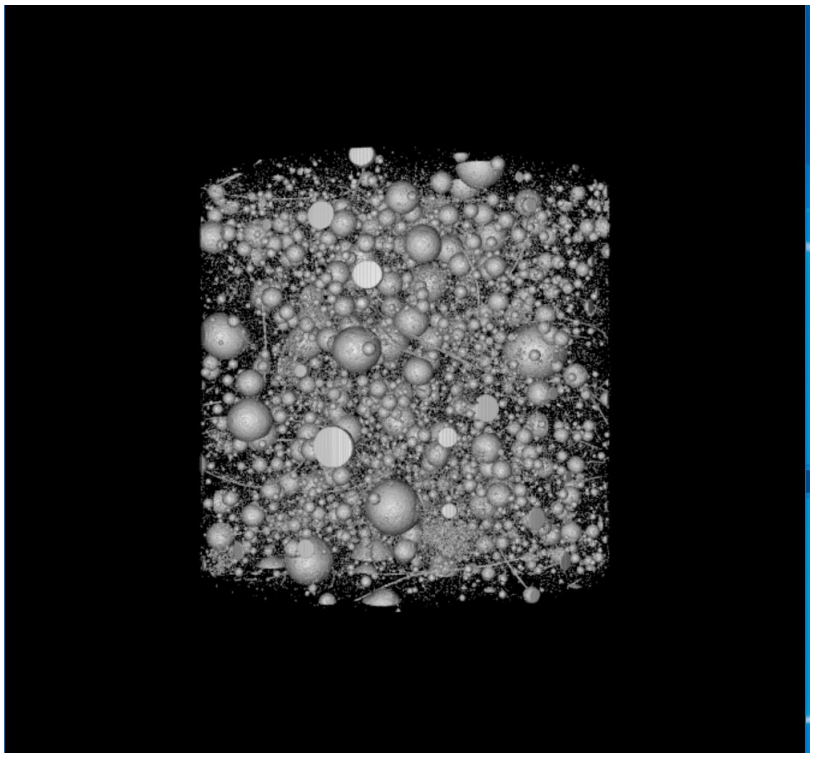


FIGURE 5.5: 3D view of the pores and pp fibres in the 30_05 sample through ImageJ. Fibres are observed along with the described random spots and a multitude of pores and voids. Fibre orientation is observed in multiple directions.

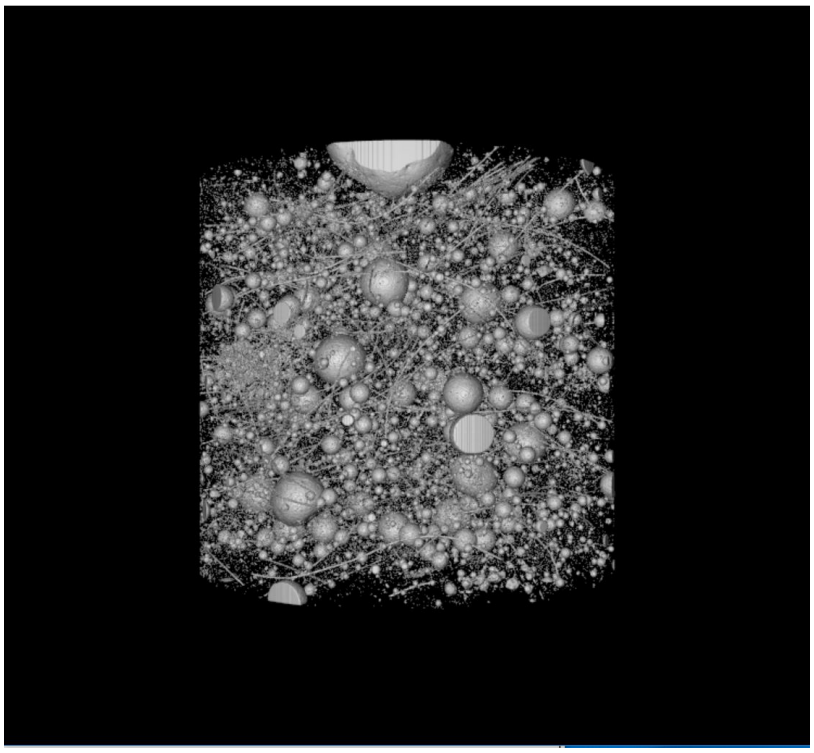


FIGURE 5.6: 3D view of the pores and pp fibres in the 30_10 sample through ImageJ. Fibre orientation observed in multiple directions.

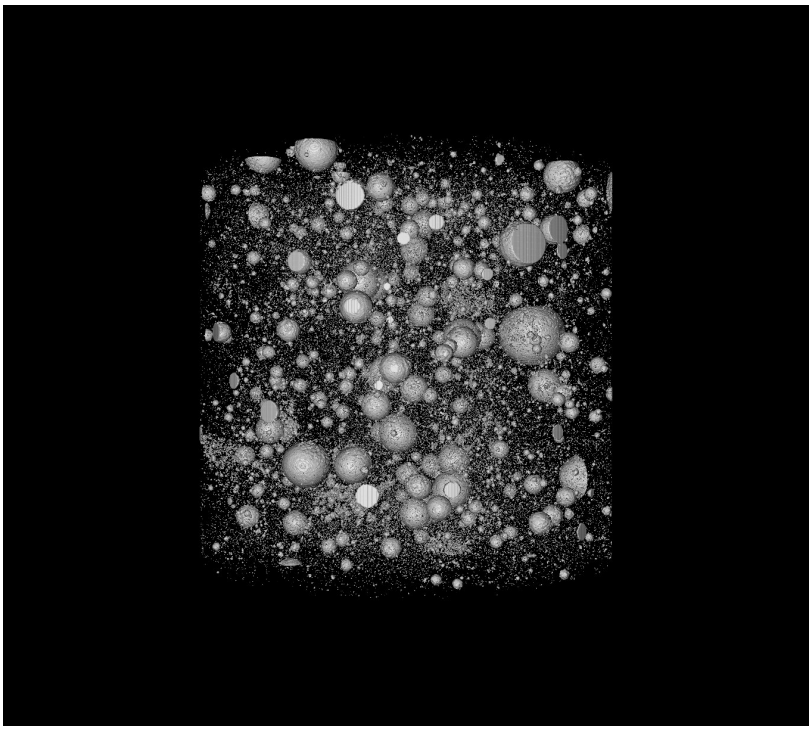


FIGURE 5.7: 3D view of the pores and pp fibres in 40_00 sample through ImageJ. Less visible pores compared to the 30 samples, combined with described random spots.

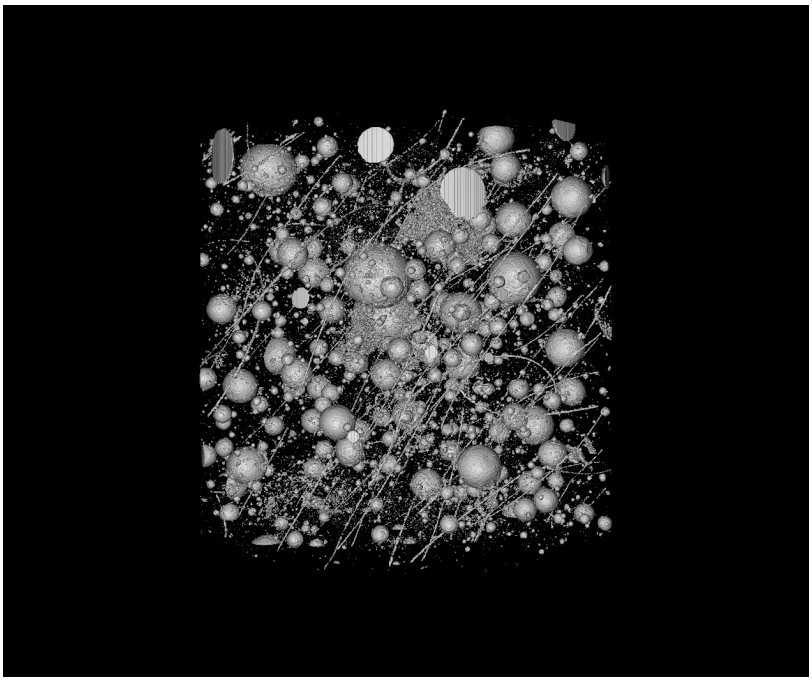


FIGURE 5.8: 3D view of the pores and pp fibres in 40_05 sample through ImageJ. Fibres show a more diagonal orientation.

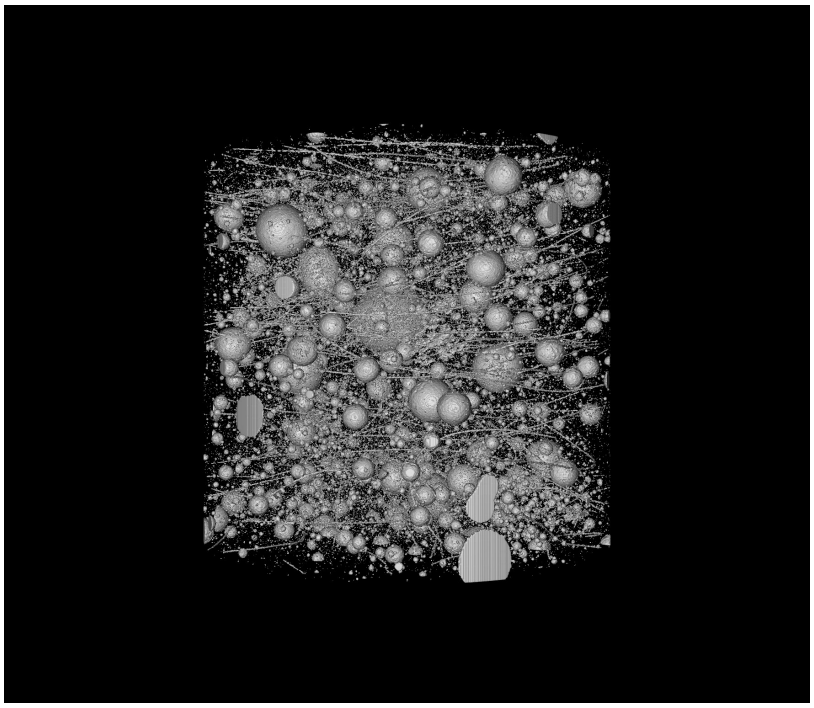


FIGURE 5.9: 3D view of the pores and pp fibres in 40_10 sample through ImageJ. The fibres already seem to show a more pronounced horizontal alignment. More fibres seem to be present in the image with random spots, creating a crowded 3D image.

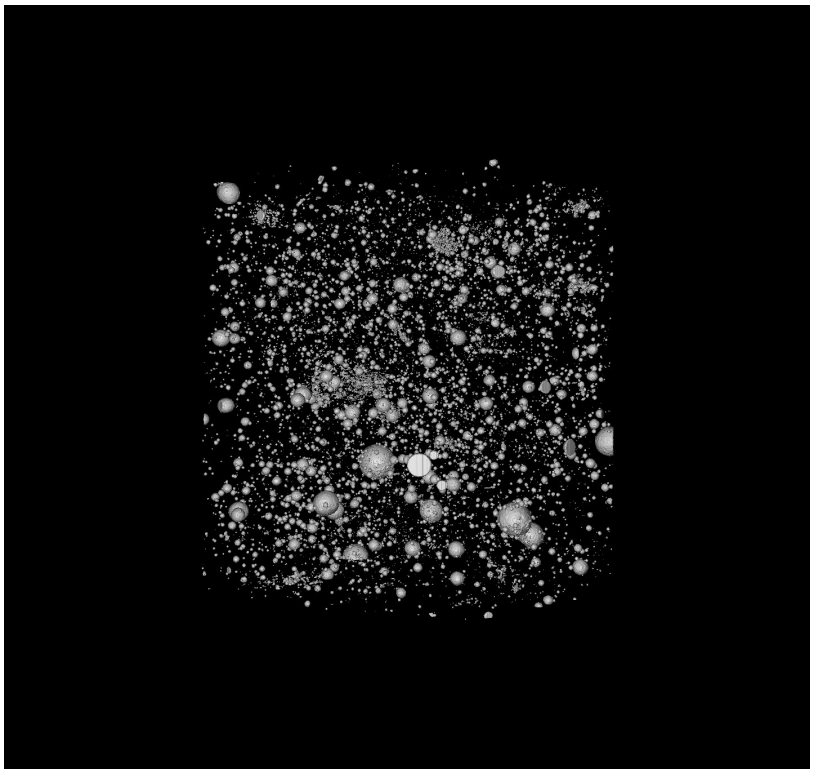


FIGURE 5.10: 3D view of the pores and pp fibres in 50_00 sample through ImageJ. The pores are much smaller in volume and diameter.

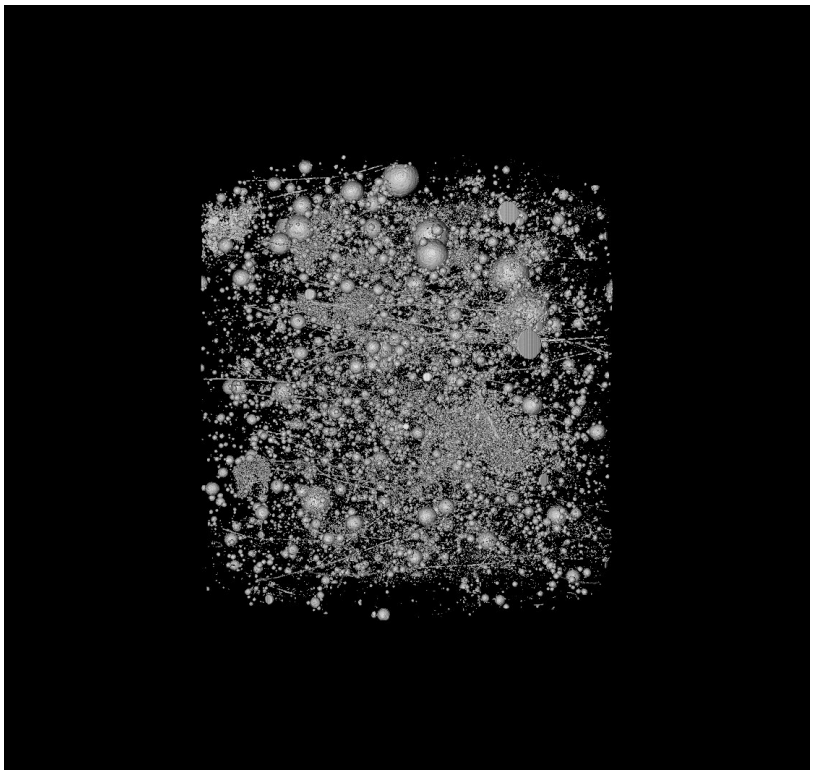


FIGURE 5.11: 3D view of the pores and pp fibres in 50_05 sample through ImageJ. Multiple pieces of porous aggregate observed through the sample. Additionally, a horizontal fibre orientation is visible

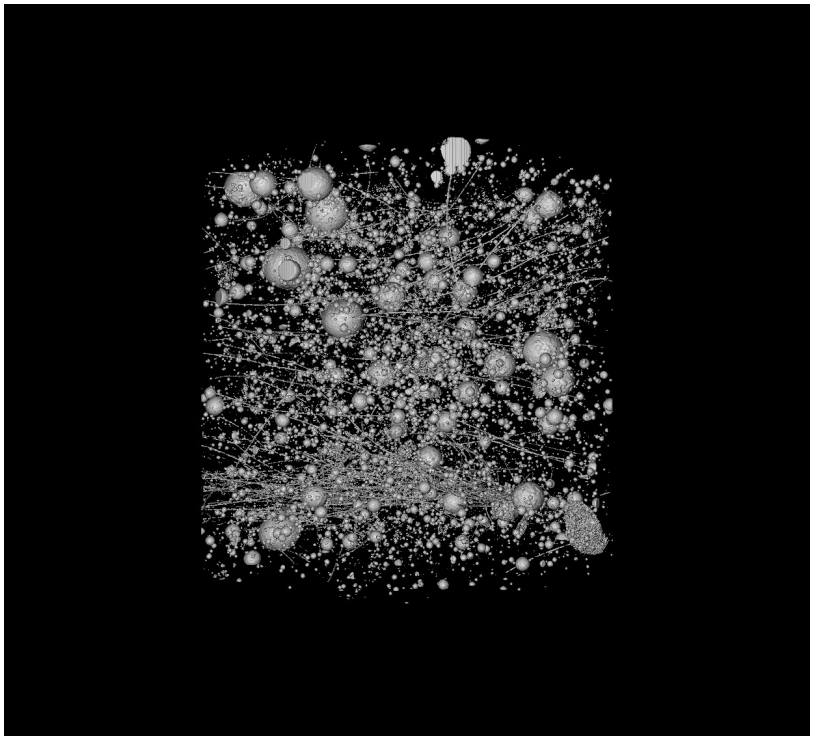


FIGURE 5.12: 3D view of pores and pp fibres in 50_10 sample through ImageJ. An agglomeration of fibres is observed at the bottom of the sample along with horizontal alignment of fibres.

5.1.5 CT Porosity - ImageJ/Fiji

Porosity from CT images was acquired using BoneJ [28], a plugin for ImageJ/Fiji. Using the segmented pore space consisting of the black and white image stack, which contains the pore volume in black and the rest of the sample in white, BoneJ is able to calculate the volume of each individual pore. The total porosity is acquired by dividing the sum volume of pores and fibres by the total volume of VOI.

To illustrate the influence of the initial air content, the air content is presented with the porosity results. Namely, that a higher initial air content will increase the porosity of the samples in the CT results. The acquired porosity along with the calculated air content from Section 3.3.5 are presented in Table 5.1 along with Figure 5.13.

TABLE 5.1: Porosity of CT images

Sample	Porosity (%)	Air Content (%)
30_00	5.67	4.8
30_05	4.20	4.3
30_10	3.09	4.1
40_00	2.20	3.0
40_05	3.34	3.4
40_10	3.44	4.6
50_00	0.57	0.8
50_05	1.32	1.8
50_10	1.56	2.2

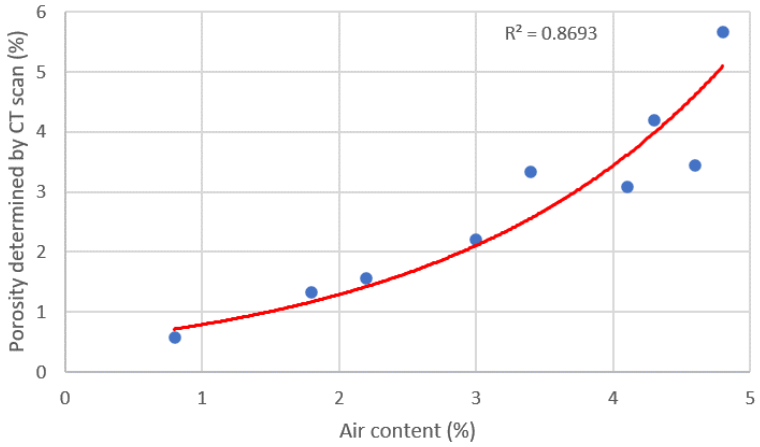


FIGURE 5.13: Porosity of the CT images versus the Air Content

5.1.6 CT porosity - VGStudio Max 3.0

A second program was used to analyse and visualise the results. The software VGStudio Max 3.0 was used, which is present on the TU Delft light microscope computer. The software is used to compare results with the results acquired through ImageJ. The original CT scan results were uploaded on the light microscope computer and reanalysed through VGStudio Max 3.0.

An area was selected through drawing a circle in the sample section and specifying the usable height. Again, not the entire cross section could be used because of misalignment between the top and bottom part of the sample, and visible noise at the top and bottom of the sample, see Figure 5.14. This specified area is then extracted from the original sample.

A problem encountered using the program is that it's free features do not allow to measure the height and diameter of the area. However, while the program was not able to specify the height and diameter of the sample because of product restrictions, it was possible to calculate the total volume of the space. This total volume will be compared to the pore volume space that was acquired and generate a porosity value.

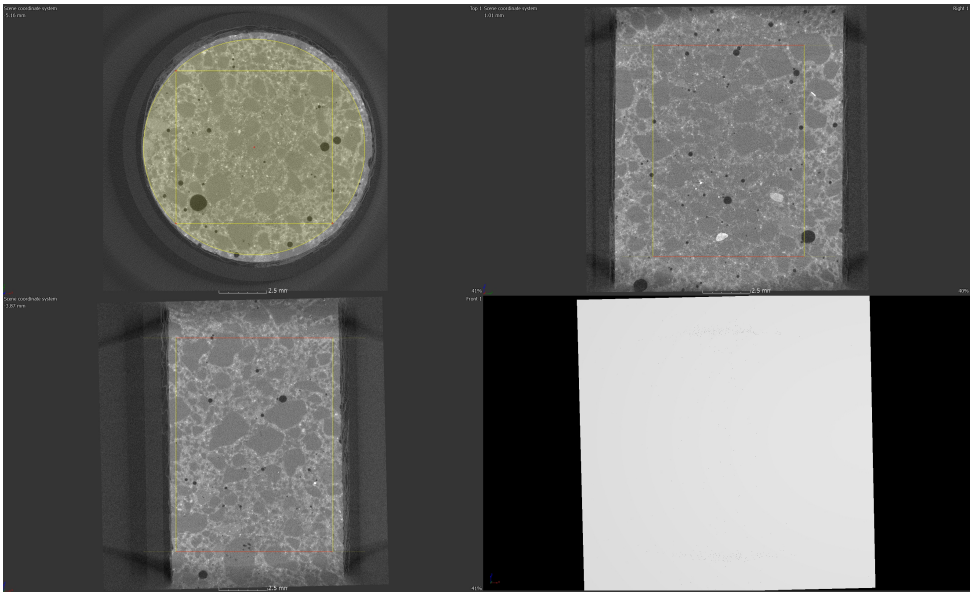


FIGURE 5.14: Specifying usable area using VGStudio Max 3.0. Top left figure shows the specified area, while the bottom left and top right show the specified area over the height. The yellow surface or lines show the area indicate the specified area.

The pore volume space was acquired by first applying a median filter to the selected volume space. This step is done to filter out the visible noise and improve the segmenting of the pore space. Afterwards, the segmenting of the pore space is done using threshold segmentation. First a small region was selected using the region growing command. Within this small region the threshold was optimized until the pore space was accurately represented. This region was then set to the entire volume and extracted.

Lastly, as the extracted volume space actually segmented the pore space out of the volume instead of isolating them, the extracted volume space has to be reversed. To reverse this, the extracted volume space is inverted, and thus the isolated pore space is acquired. Finally, this pore space is extracted again from the total volume space to create a separate volume space only containing the pores.

The acquired pore volume, total volume and consequent porosity are presented in table 5.2. A complete overview of all the 3D VGStudio Max figures is given in Appendix B.

One of the issues with using a threshold analysis is that it has more trouble with correctly assessing the phases in the image stack. In Figure 5.15 the difference is represented between the results for the 50_10 sample (Note that the VGStudio Max takes up a larger volume space. Consequently around the edges, pores are present that are not present in the ImageJ result). The problem with threshold analysis is observed quite clearly, as the fibres are underestimated compared to the ImageJ results. While the ImageJ results clearly show the fibres and the agglomeration at the bottom, the VGStudio Max result fails to recognize most of the fibres.

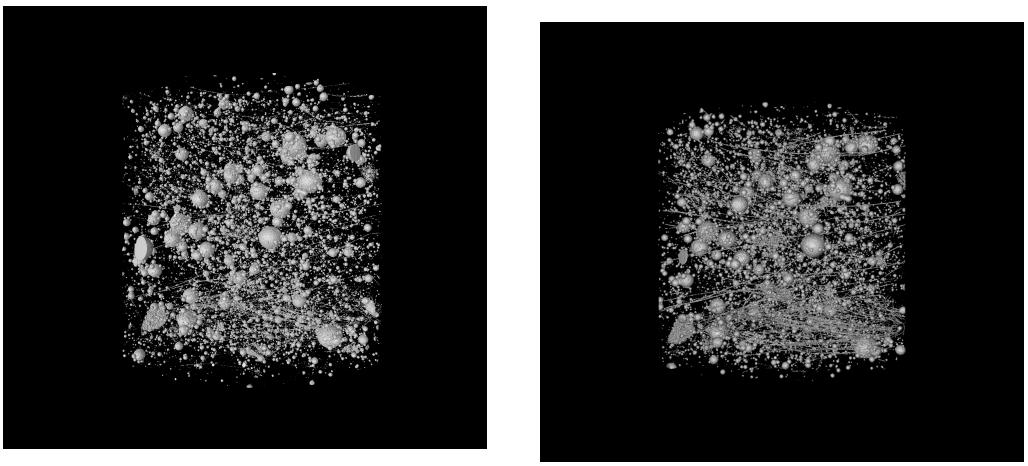
TABLE 5.2: Results VGStudio Max 3.0 volume analysis

Sample	Total volume (mm^3)	Pore volume (mm^3)	Porosity VGstudioMax 3.0 (%)	Porosity Fiji-BoneJ (%)
30_00	1154.56	59.01	5.11	5.67
30_05	1191.81	50.05	4.20	4.20
30_10	1121.06	35.31	3.15	3.09
40_00	1131.18	21.60	1.91	2.20
40_05	1174.59	33.38	2.84	3.34
40_10	1112.13	37.10	3.34	3.44
50_00	1099.94	5.10	0.46	0.52
50_05	1080.18	11.90	1.11	1.32
50_10	1132.33	15.69	1.39	1.56

While the VGStudio Max results take up a slightly different volume, the porosity check should still be compatible.

Comparing the results, some remarks can be made. First, most porosity values are quite close to each other. Consequently, it can be concluded that the segmentation is done correctly, and the porosity values are usable.

Secondly, it was noticed with the tresholding for the VGstudio Max volume that fibres were underrepresented the fibres inside the sample. Thus concluding that the porosity from ImageJ/Fiji results should be higher than the VG Studio max results. This conclusion doesn't seem to entirely hold. Sample 30_10 porosity is below the VGstudio Max value. Other samples are above or at the same value as their control value. Thus it can be assumed that the 30_10 under representation is possibly caused by the volume difference or possibly by some difference in thresholding and segmenting values. Overall, the difference is quite small, and can be explained by a number of possible reasons, some stated above.



(A) 3D view of 50_10 sample through VGStudio Max 3.0

(B) 3D view of 50_10 sample through ImageJ

FIGURE 5.15: Comparison 3D view results through VGStudio and ImageJ

5.2 Mercury Intrusion Porosimetry

Mercury intrusion porosimetry (MIP) was used to analyse the pore structure of the samples on the nanoscale. MIP turns out to be a useful analytical tool, but with a lot of remarks on how the preparation influences the porosity and structure, and how to interpret the results obtained from different samples. A multitude of different opinions exists among scholars on whether MIP is an effective tool to quantify the

porosity. Conclusions differ, and not every conclusion is positive about the end results [26, 67]. Nonetheless, this research will use MIP, as it is an accessible and quick technique to use in the MicroLab.

5.2.1 Sample preparation

10 mm slices were cut out in the middle from the original 55 mm diameter and 65 mm height samples. As discussed in Section 3.1.1, the samples contain aggregate, as cement paste creates a finer pore structure. The 10 mm slices were then broken with a hammer to create smaller pieces of mortar that will fit in the MIP. The aim for these pieces was to be around 10 mm in width, height and length. It's of importance that at least one of these dimensions is around 10 mm, further explained in chapter 5.2.1.

The sample pieces were collected until a total of 12 grams was reached. The entirety of the collected 12 grams was then submerged in isopropanol for 3 days to fully stop hydration (See Section 5.2.1 for the choice of isopropanol, Section 5.2.1 for the required exchange time).

After 3 days of exchange time, they were removed from the isopropanol and put into vacuum drying. This step is done to dry out the isopropanol.

As with the CT scans, there is a difference between maturity of the samples. Problems to get an appointment for the MIP made it difficult to achieve the correct maturity date. Consequently, MIP testing was performed much later than the initially wanted 8 weeks. The 30 samples were tested at approximately 12 weeks, 40 samples at 11 weeks and the 50 samples at 10 weeks.

Arresting hydration method

The method used to arrest hydration was solvent exchange using isopropanol, followed by vacuum drying. This is the most effective method to preserve the pore structure of samples [65, 82, 91, 93, 94, 95]. Points of attention should be made using isopropanol nonetheless, that should be considered when viewing the results.

First, damage to the pore structure will always happen at some scale, but with isopropanol the effects are far less severe than other drying methods. Some damage does happen in the cement structure. The main points of attention were damage is thought to happen are the $Ca(OH)_2$ and CSH structures in the cement [1, 91].

In terms of damage to the $Ca(OH)_2$ structure, Zhang and Scherer [93, 94] concluded that the damage to $Ca(OH)_2$ is less significant then reported by previous studies, as previous studies based their conclusions on TGA to analyse the effects. Stating that the main problem with TGA is that it possibly enhances the reaction of isopropanol with $Ca(OH)_2$ in a complicated way that needs further research to fully comprehend. Further researching the effect with different experimental tools confirmed the suspected TGA reaction with $Ca(OH)_2$, and concluded that the damage effects are less significant then previously reported.

In terms of damage to the CSH structure, research confirmed that isopropanol is able to draw the interlayer water out between the CSH structure, but unable to replace it [50, 98]. Drawing out water from these interlayers without fully replacing them, can cause the CSH structure to collapse. Research confirms this collapse of interlayers to be true, verified by length changes observed during isopropanol replacement [10, 29]. Disagreement exists whether the isopropanol is entirely unable to penetrate the interlayer after drawing out the water [50] or that the interlayer water is partly replaced by isopropanol and partly collapsed [98].

Zhou et al. [98] further showed that the pore structure changes during prolonged exposure to isopropanol, as a consequence of drawing water out of the CSH structure. As the CSH interlayer structure collapses, the interlayer pores decrease significantly while the volume of interhydrate pores increases. In addition, also proving that the total volume of the interlayer pores, gel pores and interhydrate pores stay relatively the same. Showing that there is a transition from interlayer pores to gel pores and interhydrate pores when exposed to isopropanol. Contraction and collapse of the CSH structures is explained as the main cause of this observation.

To conclude, the latest research confirms the damage to both the $Ca(OH)_2$ and CSH structures, but reports it less significant than initially described by earlier papers.

Exchange time arresting hydration

To have a correct indication of the solvent exchange time, a correct assessment of the diffusivity and the dimensions had to be made for the mortar samples.

The dimensions have to be determined, as larger dimensions will require longer exchange times. The exchange time is controlled by the smallest dimension size of the sample, and easily calculated with the use of the following formula [91]:

$$t_e = a^2/D \tag{5.1}$$

In which t_e is the equilibrium time, a the characteristics thickness (outside to middle of sample. radius for a circle, 1/2*thickness for a cube), and D the diffusivity of the sample. Then depending on the remaining water in the sample multiplied by a certain constant. This constant is estimated using Figure 5.16.

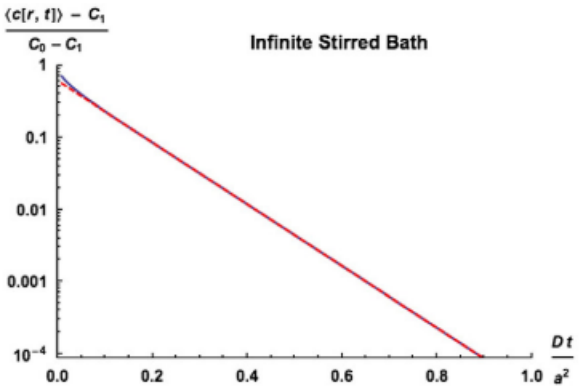


Fig. 7. Normalized concentration in the pores of a spherical particle with initial concentration C_0 surrounded by an infinite bath at concentration C_1. The solid curve is the exact solution and the dashed (red) curve is the approximation given in Eq. (2).

;

FIGURE 5.16: Isopropanol solvent exchange time constant determination[91]

To further elaborate and explain the figure, the first step is to determine what the required remaining water content is. If a remaining water content of 0.10% is wanted, a value of 0.65 should be used. Which can be read from the horizontal axis of Figure 5.16 at the 0.001 value of the red line. Consequently, as 0.10% remaining water content is the general rule of thumb [91], 0.65 will be used for the estimate of our own experimental samples.

This does introduce a second unknown, the diffusivity. For the tested samples this is an unknown value. However, with the use of other researches an estimate can be made on the value of isopropanol exchange time in mortar samples.

Backward calculation is done with the use of data from Zhou et al. [98]. The research used a mortar paste with W/C 0.50 cured for 32 weeks. Specimens had a diameter of 25 mm and a height of 20 mm. It took 6 weeks to fully penetrate the isopropanol until a weight change of less then 0.01% was achieved per week.

By rewriting Equation 5.1, the diffusivity can be calculated as following:

$$Diffusivity = constant * a^2/t_e = 2.480 * 10^-11\ m^2/s \tag{5.2}$$

A constant of 0.90 is used as the water concentration reduced to 0.01% . A value of 10 mm is used for a, and t_e is converted from 6 weeks to seconds.

Analysing the calculated value for the diffusivity, it seems off compared to other values. Zhang and Scherer [91] reported for cement pastes diffusivity values of $3 * 10^-11\ m^2/s$ for a 3 year old W/C= 1.0 paste, and $3 * 10^-12\ m^2/s$ for a 3 year 0.30 W/C ratio paste. Further finding that a relative average value for the diffusivity is around $1 * 10^-11\ m^2/s$ [30, 91].

Considering the difference in microstructure between mortar and cement paste (see chapter 3.1.1 and how it influences the diffusivity, the calculated diffusivity is assessed incorrect.

Unfortunately, no other reference samples were found through literature. Consequently, an estimate is made for the diffusivity for the 0.50 and 0.30 W/C ratio at respectively $10^-9 m^2/s$ and $10^-10 m^2/s$.With these estimates the required exchange time can be calculated for the 0.30 and 0.50 W/C ratio samples. Logically, the 0.40 value will lie somewhere in between.

$$t_e = 0.65 * (0.005^2/10^-9 = 4.5\ hours\ (W/C = 0.50)$$

$$t_e = 0.65 * (0.005^2/10^-10 = 1.88\ days\ (W/C = 0.30)$$

As a result of the above calculations, an exchange time of 2 days is deemed sufficient to properly stop hydration and reduce the original water content to less than 0.10% for all 3 W/C ratios.

The last step in the process is to remove the isopropanol from the samples. This is recommended to do using vacuum drying for 24 hours with cement pastes with dimensions of 1 mm thickness and 31 mm diameter [11]. As the used samples are mortar, it was determined that vacuum drying for 3 or more days will be enough.

MIP setup

MIP was performed using a Micromeritics AutoPore IV 9500 Mercury Porosimeter. A contact angle of 141 degrees was used. Dried samples were first weighted, then put inside the penetrometer. The penetrometer was subsequently greased with Apiezon H Grease around the closing edge to ensure proper closure. After samples were placed inside and greased, the closing lid was put on top. A plastic closing cylinder was then put around the penetrometer through the bottom part, and closed around the lid. The lid and plastic cylinder were then further tightened with a wrench to ensure proper closure. The penetrometer with the samples inside was then weighted again.

With the parameters determined and preparation done, the sample is ready to undergo the low pressure analysis. Another plastic cylinder is placed around the penetrometer cone to ensure proper closure inside the MIP. The penetrometer is then placed inside the low pressure analysis port of the porosimeter. Parameters for the weights and penetrometer were entered in the AutoPore IV software program as last preparation. With all the preparation steps taken, the sample is ready for the low pressure analysis.

After completing the low pressure analysis, the preparation for the high pressure analysis is commenced. The penetrometer is removed from the porosimeter while keeping the open end pointed up to prevent mercury from leaking. The penetrometer with mercury inside is then weighed again. After determining the total weight, the penetrometer is placed inside the high pressure analysis port for the same named analysis. The port was then closed using the roll supporters, while keeping the valve open. A new value for the total weight with mercury was documented in the software and afterwards the high pressure analysis is set up. First a measurement with the valve opened is done, afterwards with the valve closed. With both measurements done, the high pressure analysis is commenced.

5.2.2 MIP porosity

The total porosity can be calculated by multiplying the cumulative intrusion with the bulk density acquired from the AutoPore IV results. Table 5.3 presents the results from the calculations. The porosity is calculated using the entire pore size range from the MIP results, 7.17 nm to 401.87 µm.

TABLE 5.3: Porosity calculation MIP results

Sample	Bulk density (g/ml)	Cumulative intrusion(ml/g)	Porosity (%)
30_00	2.3480	0.03516	8.26
30_05	2.2919	0.03549	8.13
30_10	2.2977	0.03391	7.79
40_00	2.2252	0.03953	8.80
40_05	2.1929	0.04453	9.77
40_10	2.1766	0.04694	10.22
50_00	2.1434	0.05333	11.43
50_05	2.1308	0.05635	12.01
50_10	2.1322	0.05532	11.80

5.3 Pore structure analysis

5.3.1 Pore Size Distribution

MIP: pore size distribution

MIP results are acquired by exporting the files from AutoPore IV to an excel file for each individual sample. Through Excel plots are made for the log differential intrusion and the cumulative intrusion. Samples were put together per W/C ratio. Results are shown in Figure 5.17-5.22. Critical pore diameter is indicated in the log differential intrusion graphs.

For the W/C ratio 0.30 samples, a critical pore diameters of 14.70, 14.71 and 19.42 nm were found for respectively the 30_00, 30_05 and 30_10 samples.

For the W/C ratio 0.40 samples, a critical pore diameters of 18.12, 16.88 and 19.41 nm were found for respectively the 40_00, 40_05 and 40_10 samples.

For the W/C ratio 0.50 samples, a critical pore diameters of 20.82, 22.23 and 22.23 nm were found for respectively the 50_00, 50_05 and 50_10 samples.

It can be observed that the samples with a lower water/cement ratio clearly have a more refined pore structure than the higher ones. For the 30 samples a sharp gradient increase can be observed for the cumulative intrusion around 20 nm, while this gradient increase for the 40 samples already starts at around 40 nm, and for the 50 samples around 50 nm. Indicating that larger capillary pores are more frequent in the higher water/cement ratio samples. This is confirmed by the log differential intrusion, through which the increase is displayed clearly around the given pore diameters.

The increased porosity due to lower workability in the 40 samples with pp fibres is reconfirmed through the MIP results. There is a 1.4% difference in porosity between the 40_00 and 40_10 while no superplasticizer was used, only pp fibre.

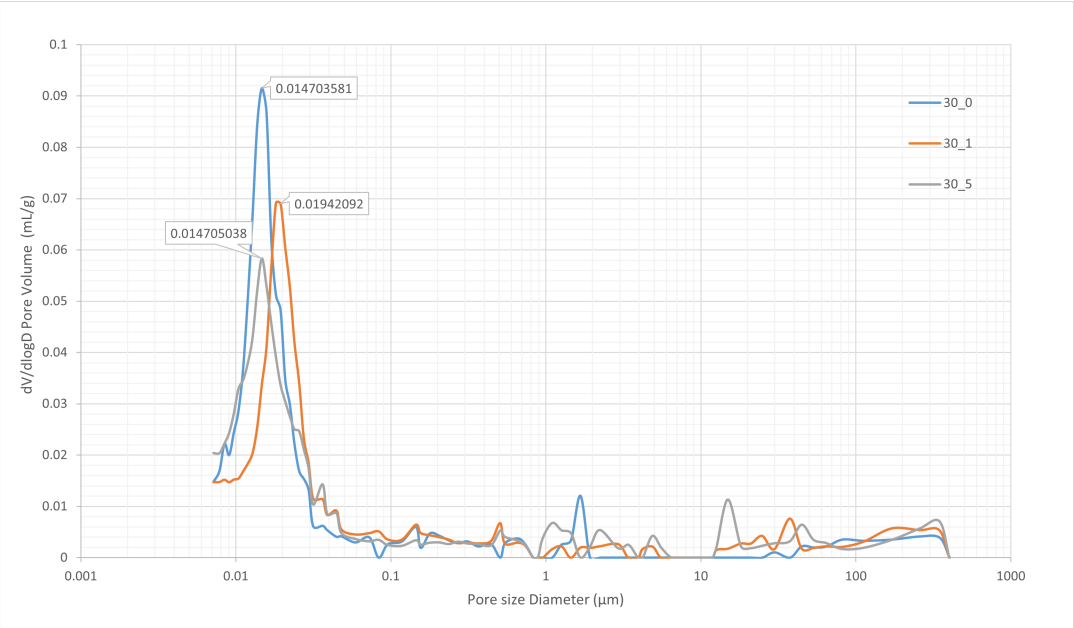


FIGURE 5.17: Log differential intrusion vs pore size diameter for 30 samples

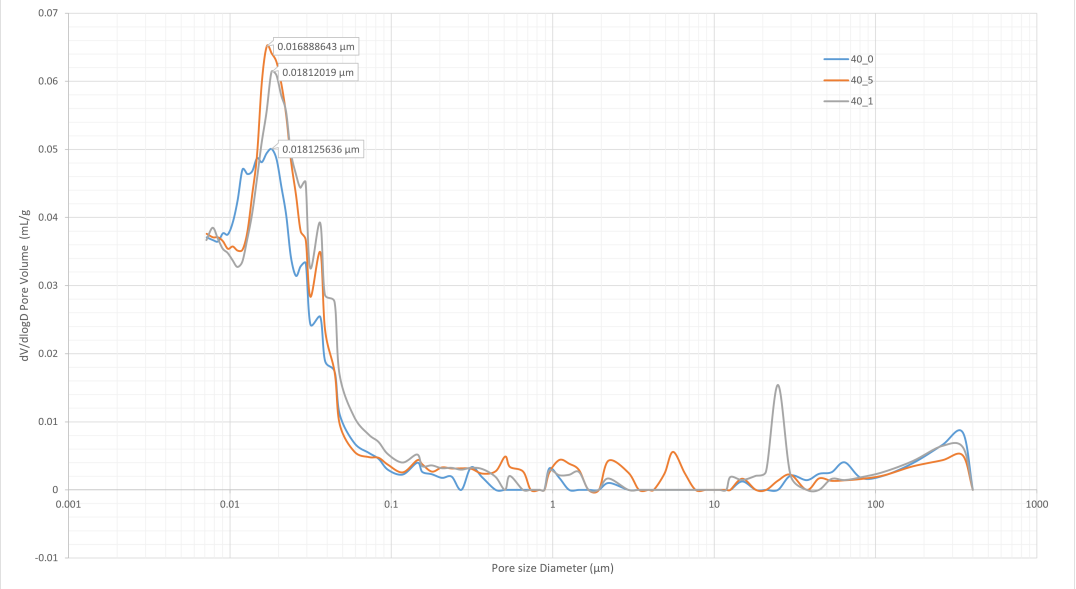


FIGURE 5.18: Log differential intrusion vs pore size diameter for 40 samples

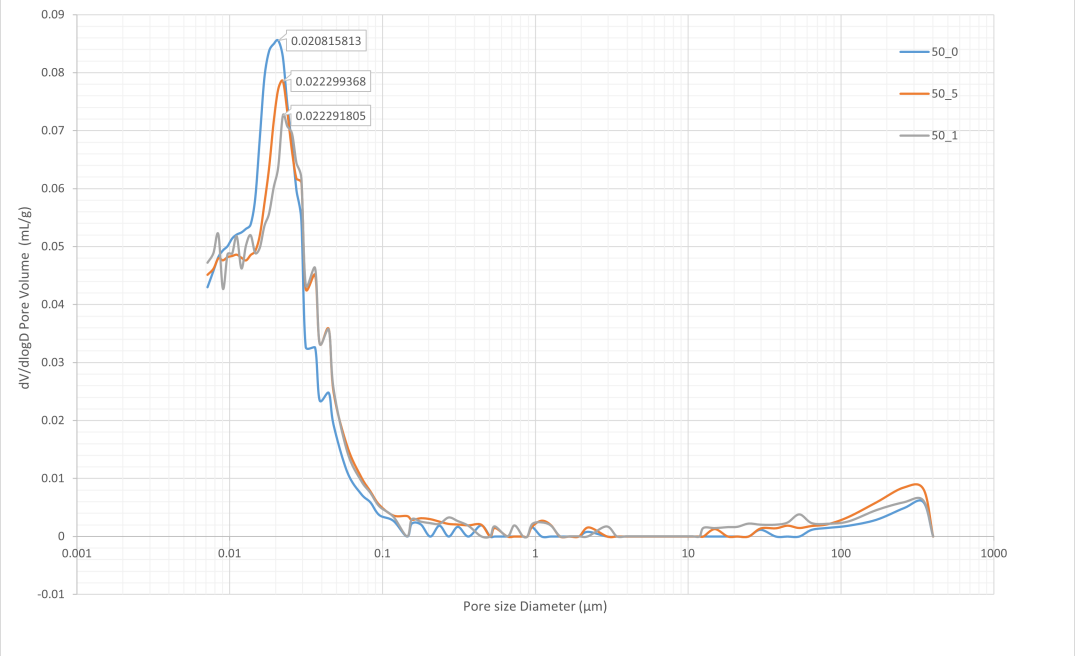


FIGURE 5.19: Log differential intrusion vs pore size diameter for 50 samples

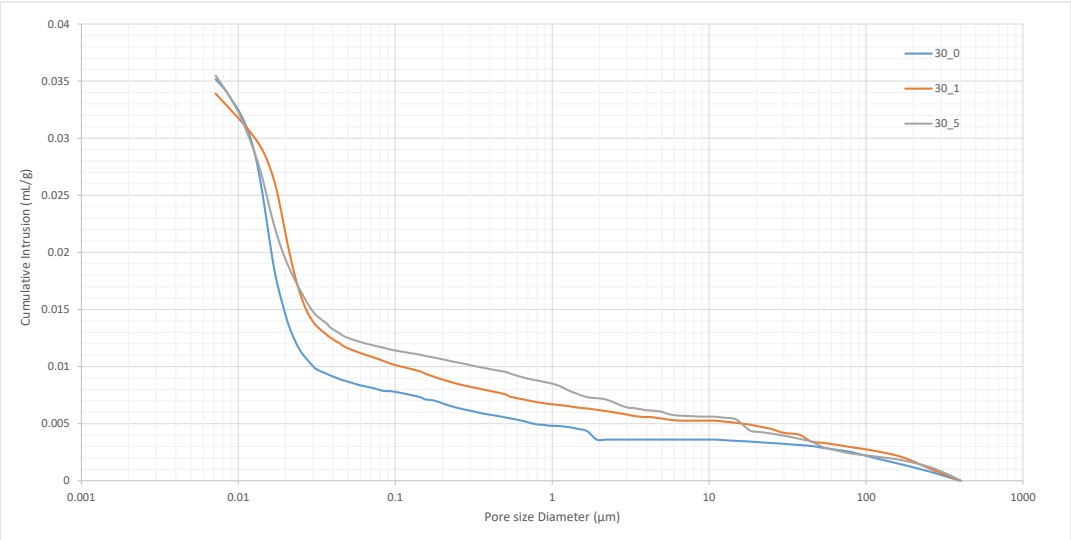


FIGURE 5.20: Cumulative intrusion vs pore size diameter for 30 samples

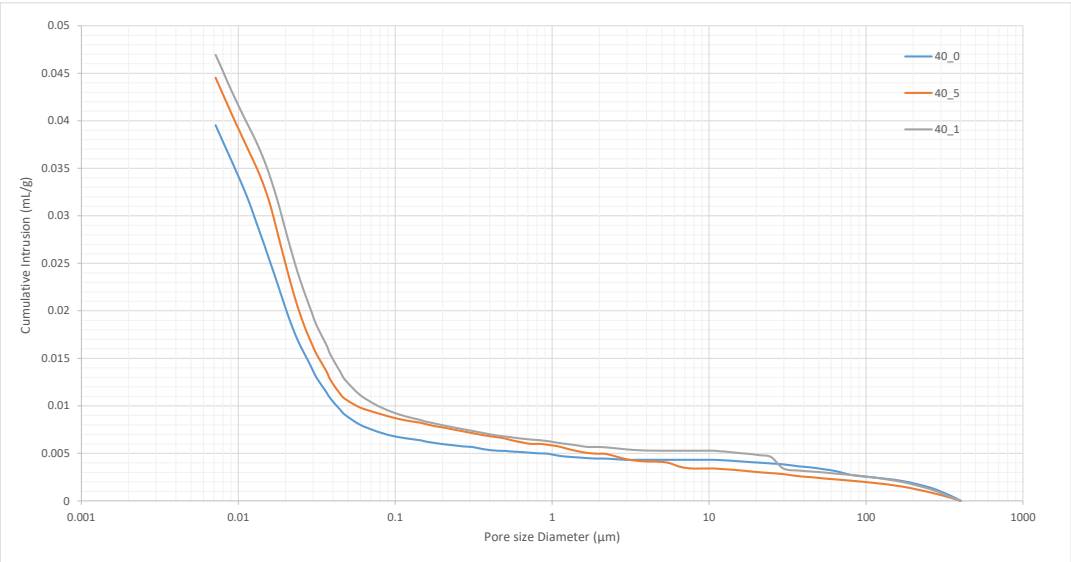


FIGURE 5.21: Cumulative intrusion vs pore size diameter for 40 samples

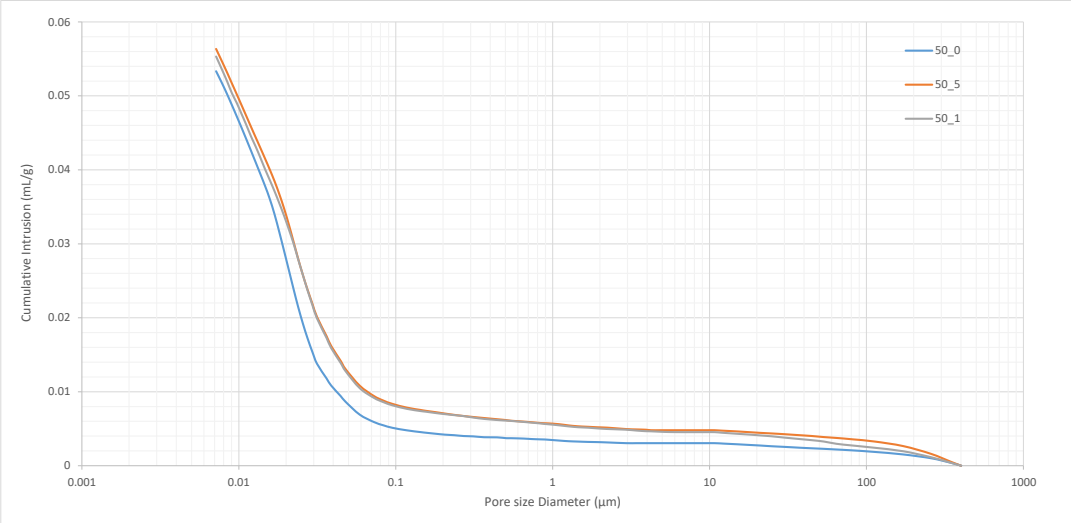


FIGURE 5.22: Cumulative intrusion vs pore size diameter for 50 samples

CT: pore size distribution

Pore size distribution for the CT samples was acquired using the BoneJ plugin in ImageJ/Fiji [28]. Using the segmented pore space consisting of a black and white binary image stack, containing the pore and fibre volume in black and the rest of the sample in white, BoneJ is able to calculate the volume of each individual pore and fibre. Values are subsequently stored and can be exported to an Excel file. The Excel file is saved separately per sample as a CSV file and exported to Matlab.

Using Matlab, it is possible to quickly treat the data and calculate the volume values. However, some assumptions had to be made. First, all pores are assumed spherical to convert them to diameter values. Secondly, fibres are assumed to be pores as well and thus spherical. This is due to the fact that it is difficult to distinguish pores from fibres through the BoneJ results.

With these assumptions, the pore diameter can be calculated from the volume values using the following formula:

$$D = \sqrt[3]{\frac{6 * V}{\pi}} \tag{5.3}$$

In which D is the pore diameter and V the volume acquired through the BoneJ results. Using the histogram function in Matlab, it is able to treat the data set and plot the pore diameter versus the frequency.

However, the histogram of pore diameter versus frequency was assessed to miss some key information. The biggest concern being that the bigger pore diameters might be low in frequency, but large in volume contribution. As a result, with a frequency plot, the contribution of the larger pore diameters seems marginal, while in truth their contribution to the total volume is quite significant.

Additionally, a number of binary image stacks have a lot of small pores visible due to over segmentation that are not pores when compared to the original CT image. These small pores show up in large abundance in the frequency plots, while the contribution to the total volume is marginal. These small pores usually consist of a single or a couple of voxels, which are in the range of 10-30 µm diameter in the graphs.

Consequently, the plot was converted to an incremental volume versus pore diameter histogram. The calculation is done by reverting the pore diameter value of the bin back to the volume, and multiplying it with the calculated frequency value from the histogram, see equation 5.4. Afterwards, the incremental volume is divided by the total volume of the sample to acquire the incremental porosity of the sample, see equation 5.5.

$$\Delta V = \frac{1}{6} * \pi * D^3 * Freq \tag{5.4}$$

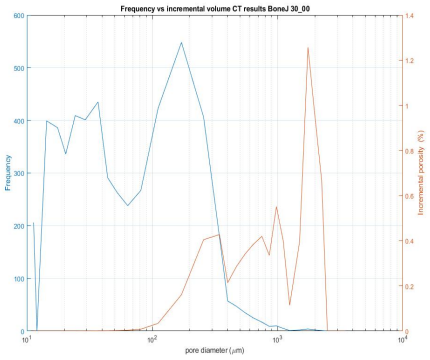
$$IP = \Delta V / V \tag{5.5}$$

In which IP is the incremental porosity (%), Δ V the volume per pore diameter bin (mm^3), and V the total volume of the cylinder (mm^3).

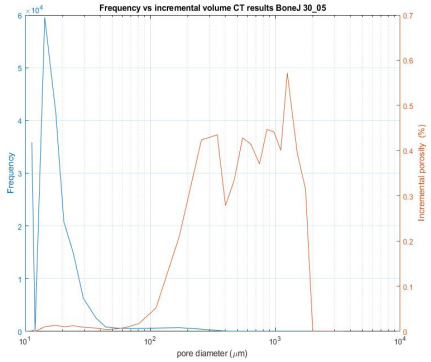
If these incremental volume values are added up, they will add up to the total porosity value of the CT scan.

As can be seen in Figure 5.23, the frequency plot is much higher in value for the lower pore diameters, while the larger pore diameters are almost negligible for the frequency values. However, when considering the volume values associated with the larger pore diameters they are actually quite significant, contributing the most to the total volume of the results.

Additionally, in the 30_05 figure the contribution of the not existing pores can be observed. The smaller pores of the 30_05 sample having a much larger frequency compared to the 30_00 sample. Resulting in an even more misleading figure.



(A) Frequency versus dV/V incremental porosity 30_00 sample



(B) Frequency versus dV/V incremental porosity 30_05 sample

FIGURE 5.23: Difference between frequency and incremental porosity dV/V plots for the 30_00 and 30_05 samples

The incremental porosity versus pore diameter is plotted in Figures 5.24-5.26.

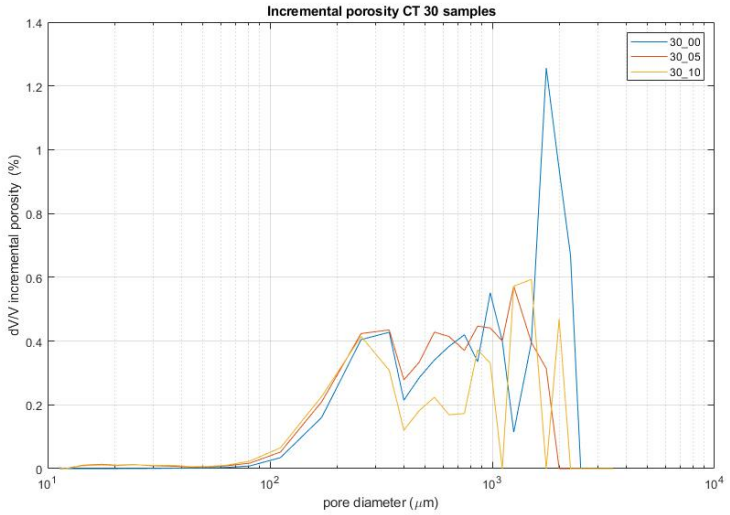


FIGURE 5.24: dV/V incremental porosity for 30 samples

The 30 sample without fibre actually had the highest porosity known from Chapter 5.1.5. As can be seen from the graph, most of that lies beyond 10^3 µm. Which could indicate that the pores beyond that range are uninfluential on the thermal shock resistance. Furthermore, the 30_00 sample runs just below the other 2 samples in the range of 10 µm - 250 µm. In between 250 µm - 10^3 µm, the lines run rather chaotic through each other, with no clear distinctions.

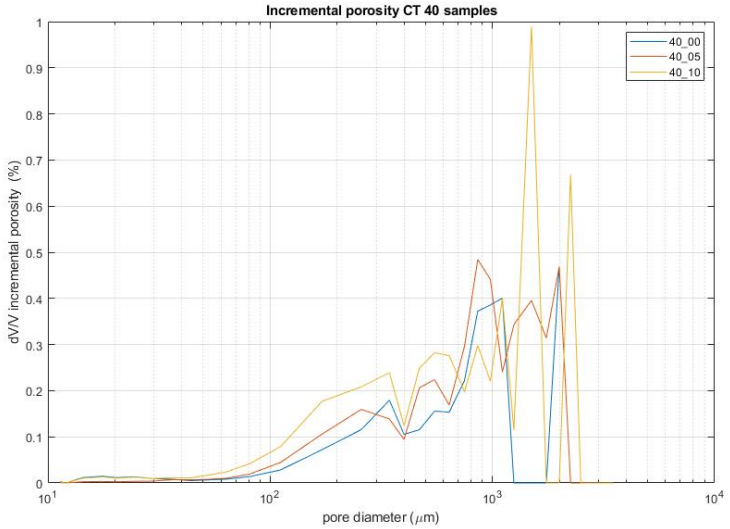


FIGURE 5.25: dV/V incremental porosity for 40 samples

The 40_10 sample has the largest volume beyond the 10^3 µm, showing opposite results from the 30 samples. This corresponds to fact that the 40_10 sample also has the largest porosity of the three samples. 10 µm - 250 µm again shows the 40_00 sample having a lower porosity than the samples with fibre.

The samples with lower thermal shock resistance, 40_00 than 40_05, both have a lower incremental porosity over the total pore diameter range. This can be predicted by the initial air content. Furthermore, this can not be regarded as conclusive results in terms of thermal shock resistance, as the 30 samples show opposite results.

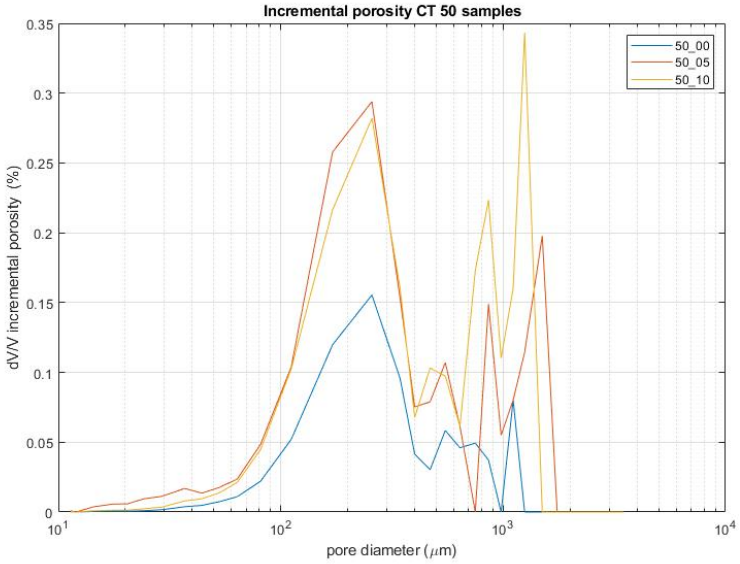


FIGURE 5.26: dV/V incremental porosity for 50 samples

Once more, the sample without fibre, the 50_00, has a lower porosity in the range of 10 µm - 250 µm. However, the 50_05 sample has a higher porosity than the 50_10 sample, while having been shown to be more prone to spalling at higher heating rates. The sample without fibre has a lower incremental porosity through the entire pore diameter range.

For most of the samples the 10 µm - 250 µm seems to comply with the spalling results. Meaning that between the samples with similar W/C ratio, the lowest incremental porosity has the highest risk of spalling. This seems to hold even for samples with a lower total porosity, namely the 30 samples. This can be explained by the addition of fibres in the samples. The fibres would show up in the range below 253 µm, as the fibres have a diameter of 31 microns and 12 mm. To further explain the lower range, it is because in the CT image results, it was observed that the diameter of the fibres was often times lower, around 20 µm - 30 µm instead of 31. Additionally, fibres can be shorter due to the mixing and cutting of the samples, which would shorten the 12 mm length.

Furthermore, there is a variance in peaks for the largest pore diameters, those larger than 10^3 µm. These peaks seem to be mostly influenced by the initial air content of the samples and as a result of that the total porosity in the CT samples. These peaks have no correlation with the spalling behaviour of the samples.

As a result of these findings it can be concluded that a incremental pore distribution on it's own is unable to predict the spalling behaviour of mortar samples.

MIP+CT: pore size distribution

To further analyse the pore size distribution of the samples, the MIP and CT results were combined using Matlab. This step was done to acquire a complete picture of all the present pore diameters. To make the results of both experiments compatible additional steps have to be taken.

For the MIP results, it was chosen to use the incremental intrusion instead of the log differential intrusion. This was necessary to make the results compatible, as the log differential intrusion changes the total intruded volume when added together

again. This gives a problem when comparing the MIP results with the CT results, as the MIP results are overestimated. Consequently, values for the MIP results are higher than the CT results, making it difficult to compare the contribution of different pore diameters.

To make the results compatible, both values of the CT and MIP need to be converted to what can be described as the incremental porosity. That is, the percentage of porosity that resides in a certain pore diameter range. This step is explained for the CT images in the previous section. While For the MIP results, the incremental intrusion volume acquired by multiplying the incremental volume with the bulk density. The bulk density and incremental volume values are acquired through MIP testing.

$$IP = IV * BD$$

In which IP is the incremental porosity (%), IV the incremental volume (mL/g) and BD the bulk density (g/mL).

With the CT results, the frequency value was first converted to a volume value using the pore diameter of the bin and than converted to the incremental porosity using the total volume, as described in section 5.3.1.

An additional problem encountered when combining the CT and MIP results, is the difference in bin sizes. The overlapping area of the graph for the results had different pore diameter increments. Consequently, it seemed that the incremental porosity values were incompatible for MIP and CT, while in fact they were quite close to each other with the correct bin sizes.

The solution was determined by extending the pore diameter vector from the MIP results to accommodate for the CT results. This pore diameter vector was then used to recalculate the incremental porosity values of the CT histogram. This opened up the possibility of using the same vector for the pore diameter on the x-axis for both results, and subsequently for the combined graph of MIP and CT.

The MIP and CT incremental porosity graphs were first combined separately to determine the compatibility of both. Afterwards, it was determined what would be a good cut-off limit to transition from MIP results to CT results, as the end-goal is to construct a single graph for the whole measured pore diameter range. With all sample graphs in mind, a pore diameter of 82 µ m was determined to be the cut-off limit.

Results for the MIP versus CT results and the combination of MIP and CT are presented in Figure 5.27 - 5.44. The combined graphs per W/C ratio are presented in Figures 5.45 - 5.47.

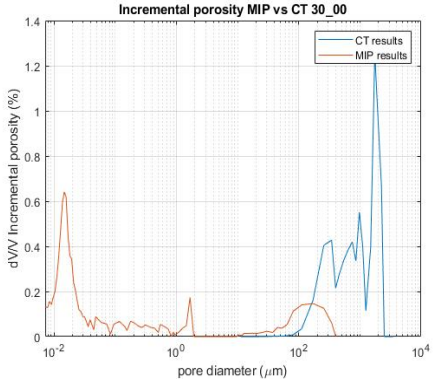


FIGURE 5.27: MIP incremental porosity versus CT incremental porosity 30_00

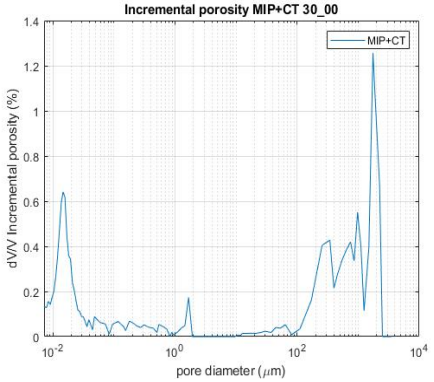


FIGURE 5.28: Incremental porosity MIP and CT combined 30_00

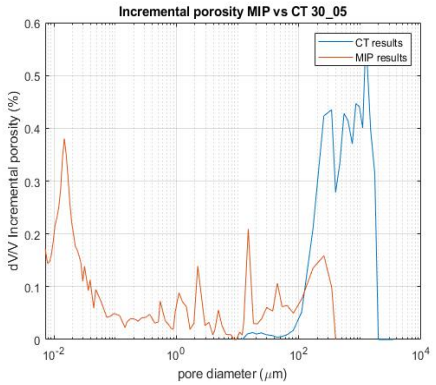


FIGURE 5.29: MIP incremental porosity versus CT incremental porosity 30_05

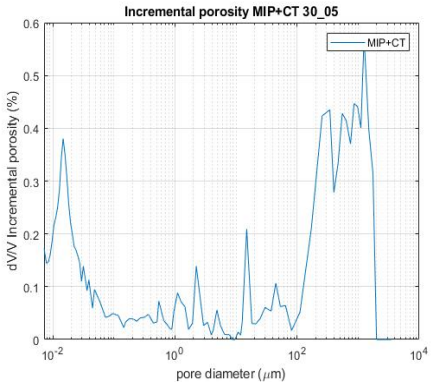


FIGURE 5.30: Incremental porosity MIP and CT combined 30_05

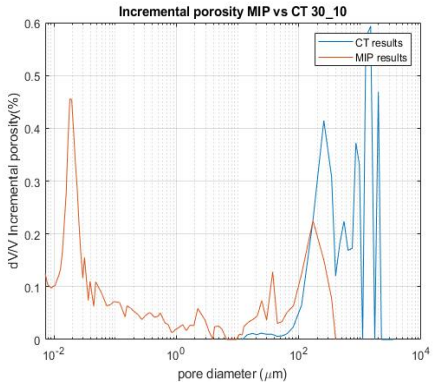


FIGURE 5.31: MIP incremental porosity versus CT incremental porosity 30_10

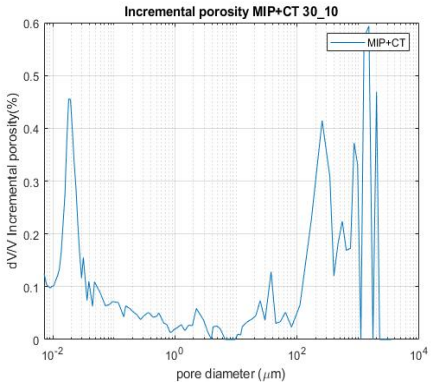


FIGURE 5.32: Incremental porosity MIP and CT combined 30_10

The 30_00 sample shows some difference in the overlapping area. While the CT results show significant porosity increase after 100 µm 100 pore diameter, the MIP results already show significant increase at 50 µm. Additionally, the MIP results seem to underestimate the porosity residing in the larger capillary pores beyond

200 µm. Furthermore, the graph shows a large amount of porosity residing in the capillary pore and air void space seen through the CT results, while the percentage of porosity residing in the gel pores is relatively lower.

The 30_05 show a more similar significant porosity increase at around 80-90 µm. Again, porosity is greatly underestimated in the MIP results for the capillary pores compared to the CT results.

The 30_10 results show the most compatible results. There seems to be some difference in the significant porosity increase compared to each other, with the MIP gaining significantly at around 40- 50 µm50 and the CT results around 80- 100 µm. However, the increment seems to gain at comparable rate with some delay.

Difference in the significant porosity increase can be explained by the maturity difference when tested. MIP testing was done at 10 weeks, while the CT testing was done at 8 weeks. Similarly the underestimation of porosity through MIP can possibly be explained by refinement of the pores as the sample matured. However, it seems unlikely that the difference in maturity at this sample age could cause an almost double porosity difference as seen in the 30 samples. Consequently, it is concluded that the MIP underestimates the porosity residing in the larger capillary pores and air voids. This conclusion to determine it an underestimation of the MIP is based on the fact that the CT results give a clear 3D visual of the pores, and is thus considered the correct value.

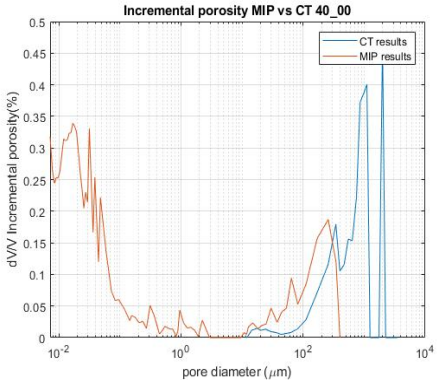


FIGURE 5.33: MIP incremental porosity versus CT incremental porosity 40_00

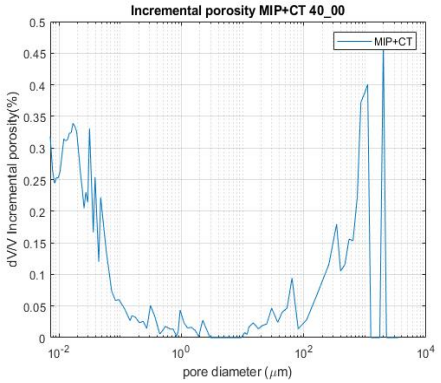


FIGURE 5.34: Incremental porosity MIP and CT combined 40_00

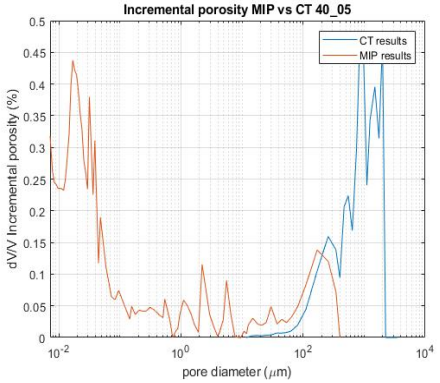


FIGURE 5.35: MIP incremental porosity versus CT incremental porosity 40_05

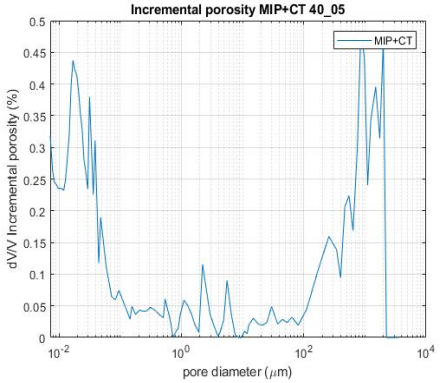


FIGURE 5.36: Incremental porosity MIP and CT combined 40_05

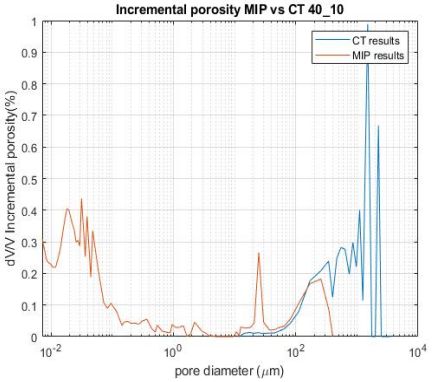


FIGURE 5.37: MIP incremental porosity versus CT incremental porosity 40_10

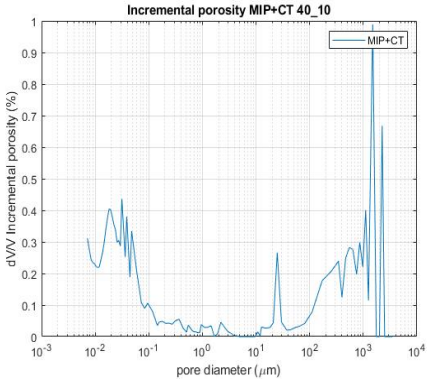


FIGURE 5.38: Incremental porosity MIP and CT combined 40_10

The 40_00 sample shows a difference in significant porosity increase consistent with the 30 samples. The MIP results show the largest increase at around 90 µm, while the CT results start to have a large porosity increase beyond 100 µm. Additionally, there resides porosity in the 10-90 µm range which is almost non-existent for the CT results.

Moreover, porosity values seem to comply with each other with some difference in it's pore diameter values. 90- 200 µm for the MIP results shows similar porosity values and increasing slope compared to the 105- 250 µm range.

The 40_05 sample has a similar disparity between results for the increase in porosity for the large capillary pores. Increase for the MIP results show at around 50 µm, compared to around 100 µm for the CT results. Again, porosity is seen below 50 µm for the MIP results which is not measured through the CT results. Furthermore, the porosity values comply with each other considering the reported disparity. However, the highest peak is slightly underestimated through the MIP results at 110 µm.

No disparity is seen for the 40_10 results. The significant increase for MIP and CT results are in the same pore diameter range. Maximum porosity value is underestimated for the MIP results compared to the CT results at a pore diameter of 200 µm. Moreover, a large peak is observed in the MIP results at 15 µm, which is not observed for the CT results. Possibility is an ink-bottle pore of quite a volume to explain the large peak.

Furthermore, the results for the MIP and CT of 40 samples seem to compare better than the 30 samples. Again, there is a difference in pore diameter for porosity values, but that can be explained by the maturity difference. The MIP samples were tested at 11 weeks, while the CT samples were tested at 7 weeks. Moreover, the large difference in porosity values that was measured for the 30 samples does not exist for the 40 samples. There is a slight underestimation for the MIP values, but not as significant as compared to the 30 samples.

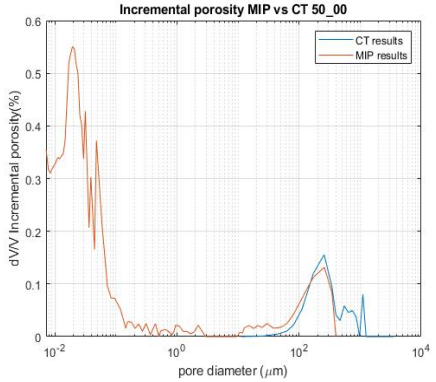


FIGURE 5.39: MIP incremental porosity versus CT incremental porosity 50_00

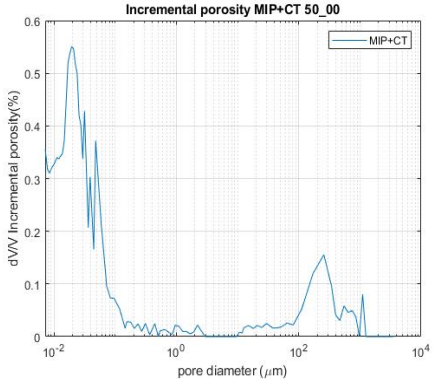


FIGURE 5.40: Incremental porosity MIP and CT combined 50_00

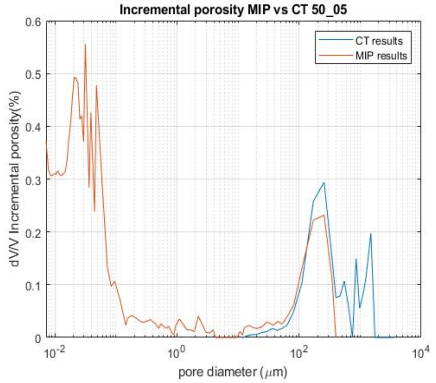


FIGURE 5.41: MIP incremental porosity versus CT incremental porosity 50_05

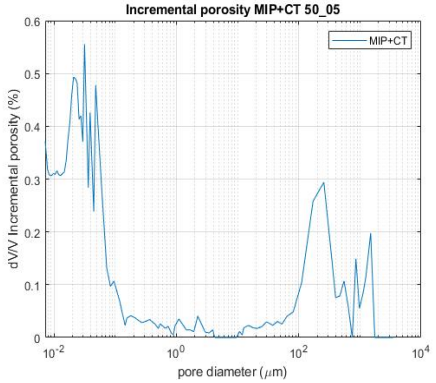


FIGURE 5.42: Incremental porosity MIP and CT combined 50_05

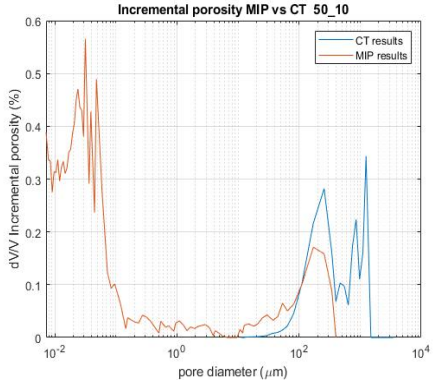


FIGURE 5.43: MIP incremental porosity versus CT incremental porosity 50_10

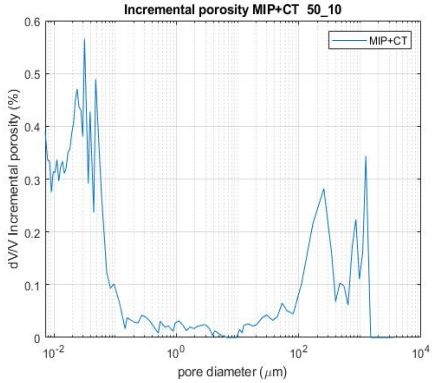


FIGURE 5.44: Incremental porosity MIP and CT combined 50_10

The 50_00 shows very compatible results between the MIP and CT porosity's. The peaks between 80- 300 µm overlap pretty well. The CT results show a somewhat higher value for the peak, while the MIP results have a steadier rise with higher values in the lower end of the pore size range.

50_05 has a similar fitting peak as the 50_00 sample. Both the increase rate and decrease rate show a comparable slope. However, maximum value for the peak is again higher for the CT results.

Lastly, 50_10 has a fitting peak between CT and MIP results as well. However, the 50_10 CT result has a much larger porosity value at the highest peak. Again, the MIP underestimates the porosity values. Additionally, while the CT results seem to be close to 0 for a pore diameter smaller than 30- 40 µm, the MIP results still detect porosity in that smaller pore diameter range.

All three samples show similar peaks with a slightly underestimated largest value for the peak at the MIP results. This is remarkable as the 50 samples were tested at different maturities for the MIP and CT tests. Specifically, 6 weeks for the CT results and 10 weeks for the MIP results.

Lastly, The samples are combined per W/C ratio to determine if a relation can be established with the spalling results.

Repeating the spalling results to clarify the following section. Every 30_00, 40_00 and 50_00 sample spalled at all 3 heating rates. 40_05 and 50_05 spalled at 30 and 50 °C/min, but did not spall at 10 °C/min. 30_05, 30_10, 40_10 and 50_10 did not spall at any of the heating rates.

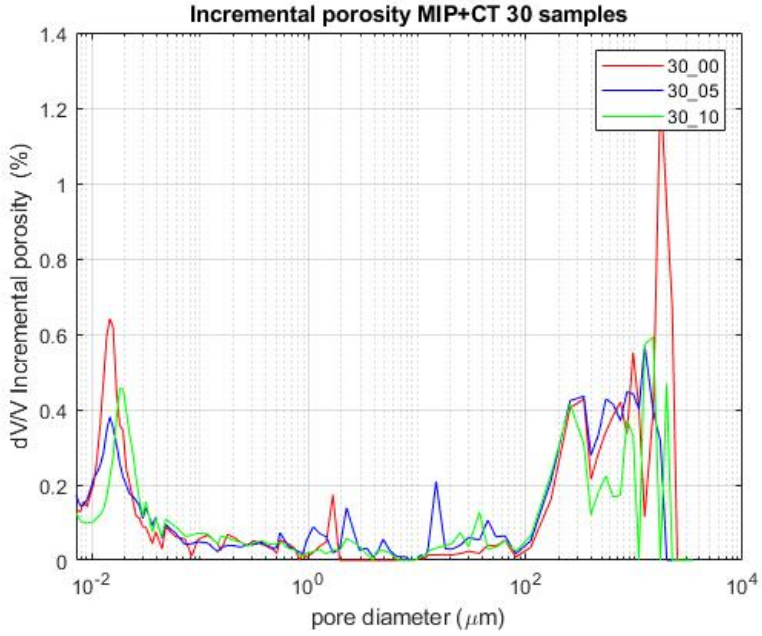


FIGURE 5.45: incremental porosity 0.30 W/C ratio

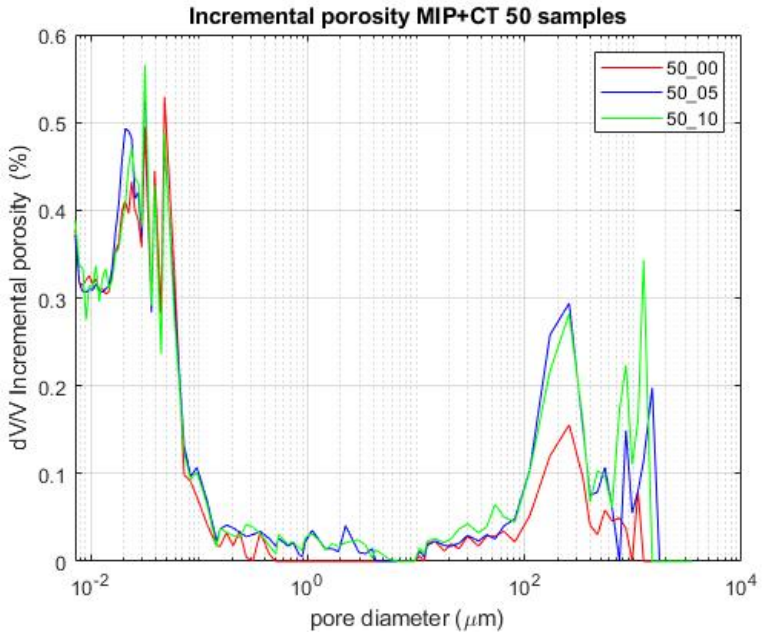


FIGURE 5.47: incremental porosity 0.50 W/C ratio

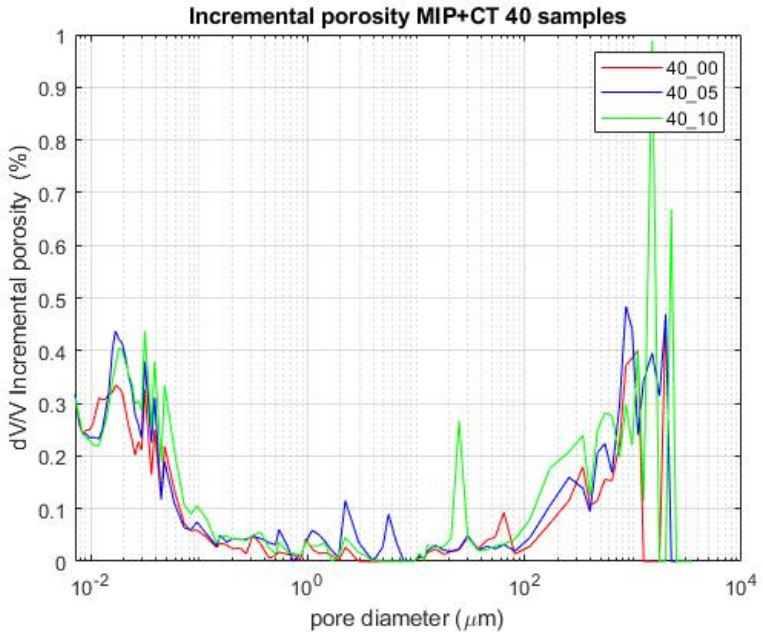


FIGURE 5.46: incremental porosity 0.40 W/C ratio

Examining the overlaying graphs per W/C ratio, no clear connection can be made in relation to the spalling results. Some differences exist between the results, but with conflicting indications in relation to the spalling behaviour.

The 30 samples display a similar pattern over the 3 samples. The sample that spalled, the 30_00 sample, actually has the highest porosity peaks across the incremental porosity. Moreover, the 30_00 has no area of decreased porosity in the displayed pore diameter range for the incremental porosity and has the highest porosity of the 3 samples.

The 40 samples display a similar pattern as well for the 3 samples. However, the

40_10 sample exhibits a porosity slightly above the 40_00 and 4_05 samples across all pore diameters.

With the 50 samples, the 50_00 has a clear lower porosity in the CT result range (80-1500 µ m). No difference is perceptible in the MIP result range across the 3 results.

As a result, while the 50_00 sample and the 40_10 exhibit a result that could be used to predict the spalling behaviour, the 30_00 sample is actually in opposite evidence, displaying higher incremental porosity values and increased spalling risk. Consequently, no conclusions can be made using the pore size distribution/incremental porosity to predict the spalling behaviour.

Porosity: re-analysis through combined PSD

With the combination of MIP and CT results, a new total porosity was calculated. This combination gives a more complete porosity value as it takes into account a larger pore diameter range and filters out the overlap between MIP and CT.

The original total porosity was calculated by adding up the MIP and CT values for porosity. However, these values contain an overlap with each other. Consequently, the values were recalculated through Matlab using the cut-off limits. This value is represented in the new porosity column in Table 5.4.

Unfortunately, due to the assumption that all the pores are spherically, and the large range used in bin sizes, quite an overestimation is created for the CT porosity values. The overestimation is large enough that the new porosity value exceeds the original porosity. Consequently, it was decided to use the original CT porosity value in combination with the new MIP porosity values to calculate the combined porosity. This value is represented in the column adj.(adjusted) porosity, Table 5.4.

To underpin the decision to keep the original CT porosity value, it can be seen from Figures 5.27-5.44 that the CT porosity residing below the cut-off limit is quite a small percentage. Consequently, it can be concluded that it has a small significance on the total porosity.

As can be seen from the last column adj. porosity, the total porosity was once more not a good indicator for the spalling behaviour of the samples. The 30_00 actually has the highest total porosity and spalled at heating rates. The 30_10 samples did not spall at any heating rates while having the lowest total adjusted porosity.

TABLE 5.4: Total porosity MIP and CT results combined

Sample	Orig. MIP porosity	New MIP porosity	Orig. CT porosity	New CT porosity	Orig. porosity	New porosity	Adj. porosity
30_00	8.25	7.67	5.67	7.34	13.92	15.01	13.34
30_05	8.13	7.26	4.20	5.62	12.33	12.88	11.46
30_10	7.79	6.80	3.09	4.24	10.88	11.04	9.89
40_00	8.79	8.20	2.20	2.79	10.99	10.98	10.39
40_05	9.77	9.30	3.34	4.14	13.11	13.44	12.64
40_10	10.22	9.70	3.44	4.56	13.66	14.26	13.14
50_00	11.43	10.99	0.57	0.79	12.00	11.78	11.56
50_05	12.01	11.25	1.32	1.78	13.33	13.02	12.57
50_10	11.80	11.21	1.56	2.15	13.36	13.36	12.77

5.3.2 Pore Connectivity analysis

MIP: pore connectivity

From literature review, it is known that not all of the porosity found through MIP results contribute to the permeability and pore connectivity of the tested sample [1,

66]. The Ink-bottle pores are known to contribute to the total penetrated volume with the first intrusion using MIP. However, during extrusion and the second intrusion these pores stay saturated with mercury and are unable to be extruded during depressurization(see Figure 5.48). Consequently, these pores are believed to not contribute to the permeability and pore connectivity of the sample [88]. Using this fact a pore connectivity value can be calculated using the MIP results.

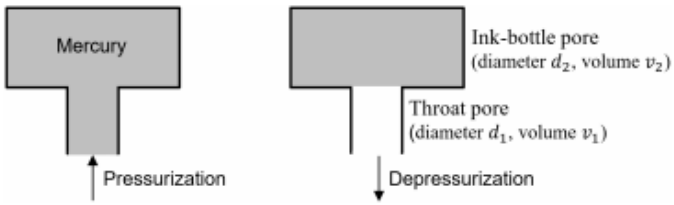


FIGURE 5.48: Ink-bottle effect visualized during extrusion[92]

The volume that is able to be extruded is called the effective porosity, as that is the volume through which liquids and vapours are consistently able to enter and exit the sample. As such, the effective porosity attained from the extrusion curve is considered the porosity that contributes to the permeability and pore connectivity of the sample. The ink-bottle porosity and effective porosity can be calculated using an MIP graph as presented in Figure 5.49.

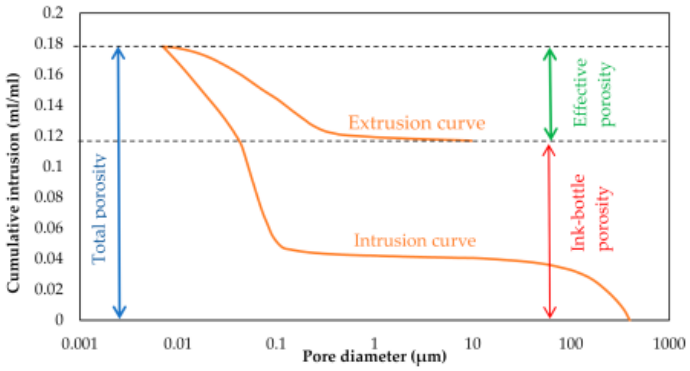


FIGURE 5.49: Determination of ink-bottle porosity and effective porosity [51]

Using the previous described parameters, Yu et al. [88] states using that the pore connectivity of a sample can be calculated using the following formula with the calculated ink-bottle porosity and effective porosity:

$$Pore\ connectivity(\%) = \frac{Effective\ capillary\ porosity}{Total\ porosity} * 100 \tag{5.6}$$

or:

$$Pore\ connectivity(\%) = (1 - \frac{Ink - bottle\ porosity}{Total\ porosity}) * 100 \tag{5.7}$$

Using the acquired results from the MIP results, the pore connectivity was calculated for the tested samples, presented in Table 5.5. Cumulative intrusion and Cumulative extrusion were acquired from the MIP test results. The cumulative extrusion is already equal to the ink-bottle volume (I-B volume in Table), as can be

determined from Figure 5.49. Effective volume was calculated by subtracting the cumulative extrusion from the cumulative intrusion. Finally, the pore connectivity was calculated using one of the formulas presented in Equation 5.6 & 5.7. Furthermore, the porosity from MIP results is presented to show how the connectivity relates to the determined total porosity from MIP.

TABLE 5.5: Pore connectivity through MIP

Sample	Cumulative Intrusion (mL/g)	Cumulative Extrusion/ I-B Volume (mL/g)	Pore Connectivity (%)	Porosity (%)	Effective porosity(%)
30_00	0.0352	0.0264	24.96	8.25	2.06
30_05	0.0355	0.0265	25.26	8.13	2.05
30_10	0.0339	0.0227	32.97	7.79	2.57
40_00	0.0395	0.0243	38.55	8.79	3.39
40_05	0.0445	0.0281	36.80	9.77	3.60
40_10	0.0469	0.0289	38.487	10.22	3.93
50_00	0.0533	0.0275	48.52	11.43	5.55
50_05	0.0563	0.0306	45.75	12.01	5.49
50_10	0.0553	0.0288	47.87	11.80	5.65

First observation that can be made is that there is a clear difference in pore connectivity between the samples based on W/C ratio. Per W/C ratio it can be observed that the values are quite closely to each other. The 50 samples have an average around 47%, the 40 samples an average around 38 and the 30 samples around 25%. Only outlier in the results is the 30_10 sample, which has a connectivity of 32% compared to the average 25% of the other two samples. This difference in pore connectivity amplifies the difference in porosity when considering what part is effective in contributing to the pore connectivity, as seen in the last column of Table 5.5. Effective porosity for the 50 samples is more than double the value of the 30 samples.

Secondly, the pore connectivity looks unrelated to the total cumulative intruded volume and thus the total porosity and is only influenced by the W/C ratio. This is especially apparent in the 40 samples, having a difference of 1.50 % in porosity, while the connectivity numbers are quite similar. This is not unexpected, but good to present with numbers.

Thirdly, there is a difference in connectivity for the 30 samples. This is believed to be caused by the workability, and the initial air content of the mix design. As is known from the air void content tests, there is a difference in the air content for the 30 samples. In which a higher air content indicates a lower workability. The reduced workability is believed to consequently cause a lower pore connectivity. 30_10 is known to have the lowest initial air content of the 30 samples, while the 30_05 and 30_00 samples both have higher initial air content values. Consequently, the connectivity is believed to be reduced as a result from the lower workability during casting. However, this relation does not show for the 40 samples, which had similar differences in the initial air content in the mix design.

In terms of thermal shock resistance, no conclusion can be made in relation to the spalling behaviour. The results for the pore connectivity through MIP on it's own shows no connection to the spalling behaviour from the oven experiments. As made clear in the first observation, the pore connectivity per W/C ratio stays relatively the same while the spalling results changed drastically between the samples based on the fibre content.

CT: pore connectivity

The pore connectivity is analysed using an ImageJ (note: not Fiji) plugin developed by Roque and Costa [78] called Tortuosity. Tortuosity as a value, is another way

to measure and describe the pore connectivity as they are inversely related to each other.

The Tortuosity plugin does what it is called, calculate the Tortuosity of an image stack. It can threshold the image in binary values, either black or white. As the image stack is already in black and white, this step is unnecessary. Afterwards it's possible to either run it in the 2D or 3D pore space. The directions to run the Tortuosity plugin in can be selected, x(+), x(-), y(+) and y(-) for 2d, and an additional z(+) and z(-) for 3d images.

The tortuosity value describes the increased path length that is need to reach point a from point b, compared to the shortest/straightforward path. Meaning in terms of thermal shock resistance, that for water vapours to easily travel through the sample a low tortuosity value indicates an easier path to travel from a to b, while a high tortuosity value indicates that the vapours have to travel an increased distance to reach point b from a. The tortuosity is described by the following formula in the Tortuosity script [78]:

$$\tau = \frac{L_g}{L_e} \tag{5.8}$$

In which τ is the tortuosity value, L_g the geodesic length of the curve which is the true travelling distance, and L_e the euclidean length which is the shortest path between reference planes (see Figure 5.50).

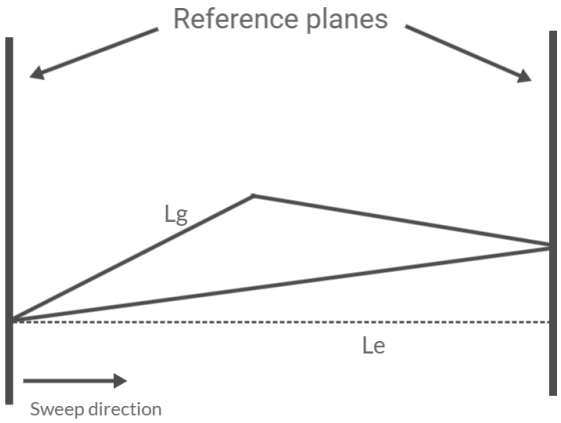


FIGURE 5.50: Determination Geodesic and Euclidean length according to ImageJ Tortuosity script [78]

Tortuosity script: pore space & non-pore space

Using the previously acquired binary black and white image stacks of the pores and fibres, the tortuosity was calculated per sample. First, the tortuosity was calculated in the pores and fibre volume space. However, as most of the pores and fibres are isolated (see Figures in section 5.1.4), the tortuosity script is running in individual pore and fibre volumes. Consequently, it is believed to be not the most reliable measure. In addition, the calculated tortuosity values seemed completely at random, while it was believed to at least be able to show some correlation with the pp fibre content.

To counter this problem, it was decided to run the tortuosity script in the non-pore space, meaning everything except the pores and fibres. Reversing the idea of the tortuosity value, as it now would mean that a high tortuosity value indicates

a good connectivity. The idea behind it was that there are large capillary pores in the way of the shortest path and that these large capillary pores are of importance in alleviating vapour pressures. Meaning that more pores and fibres residing in the shortest path would increase the tortuosity value and thus make it easier for the water vapour to travel towards the large capillary pores and fibres. Consequently, a high tortuosity value would indicate more pores inside the sample to which the water vapours can travel and mitigate spalling risk.

All calculated values are presented in Table C.3.

TABLE 5.6: Tortuosity pore space % non-pore space

Sample	Tortuosity pore space	Tortuosity non-pore space	CT porosity
30_00	1.01152	1.2683	5.67
30_05	1.00923	1.2926	4.20
30_10	1.00706	1.3028	3.09
40_00	1.00511	1.0070	2.20
40_05	1.00806	1.183	3.34
40_10	1.00794	1.1634	3.44
50_00	1.00138	1.0018	0.57
50_05	1.00322	1.0030	1.32
50_10	1.00370	1.0409	1.56

Unfortunately, these results are quite inconclusive. Some results show correlation with the spalling results, but this is more of a possibility by chance than a direct correlation.

The first tortuosity values correlate quite well with the calculated porosity values for the CT samples, meaning a higher porosity visible in the CT samples leads to a higher tortuosity value. Consequently, as the higher visible porosity through CT is influenced by the air content in the mix design, the acquired tortuosity value would be a better indicator to estimate the initial air content.

For the non-pore space tortuosity the values hold when considering the same W/C ratio. Each sample with no fibre content has the lowest tortuosity, which as explained above, indicates it is more difficult in the sample to encounter large capillary pores and fibres when the water vapours travel through the sample. However, there is absolutely no correlation between the different W/C ratio's and the observed spalling behaviour. Consequently, the tortuosity of the non-pore space is also deemed to be an insufficient indicator for the spalling risk of the tested samples. The tortuosity again seems mostly influenced by the amount of pores visible. The samples with higher visible porosity in the CT images clearly have higher porosity for the non-pore space with some variation depending on the pore and fibre distribution. This can be seen in the 30_00, as it still has the lowest tortuosity while having the highest porosity of the 30 samples.

Tortuosity script: cement and pore space

The biggest encountered problem when analysing the CT results, was that the pores and fibres stay separate from each other. Although it is possible with the MIP results, there is no possibility to analyse the 3D orientation of the pores and it's pore connectivity. At the same time, through MIP results it is known that the fibres and large capillary pores in the CT images are not separated from each other, but have cement in between them with a known porosity and pore connectivity. Consequently, it was

decided to try the tortuosity script on the pore and fibre space with the addition of the cement volume.

TABLE 5.7: Tortuosity cement + pores

Sample	Tortuosity cement + pores
30_00	1.08188
30_05	1.0562
30_10	1.07963
40_00	1.06304
40_05	1.09694
40_10	1.09198
50_00	1.06825
50_05	1.09931
50_10	1.08769

Unfortunately, as can be seen in the table above, the results are again inconclusive. No real distinction can be made between all the samples. Part of the problem was that it was quite difficult to segment the aggregate and cement correctly due to beam hardening. It was either overestimating the outside cement, or overestimating the inside aggregate content. This is caused by the overlapping grey level intensity of the inside cement and outside aggregate of the samples. Consequently, the inconclusive results are in part due to the inaccuracy of the images.

5.4 Predicting spalling: Formula

One of the main goals of the thesis was to predict spalling through the pore connectivity of the samples. The pore connectivity was chosen to be assessed through MIP and CT tests and analysis. The tests and analysis have been presented in previous sections of the chapter with mixed results.

This section presents a formula that could describes the spalling behaviour of mortar samples. The formula is compatible with the spalling behaviour of the oven experiments. However, spalling is influenced by certain parameters that were kept constant over the experiments, and thus not added to the formula, but are certainly of influence on the spalling behaviour.

The parameters that are taken into account and added to the formula are the volume/surface ratio, the heating rate, the flexural strength, the MIP connectivity and the PP fibre ratio. In future use of the formula, the volume/surface ratio should be expanded to take into account the exposed surface with one sided heating. Furthermore, additional influencing factors that are disregarded in the current formula are the compressive loading in comparison to the compressive strength, the degree of pore saturation and the tortuosity through CT that was tried to measure in the previous Chapter.

The following unity check formula is proposed that fits the experimental spalling results:

$$U.C = \frac{\sqrt{HR}}{f_{ct,fl} * 1.70 * C_{MIP}} * \frac{(0.20 - PP\%)^{1.5}}{0.20} \tag{5.9}$$

If the U.C. check is above 1.0, the sample is at risk of spalling damage. If this value is between 1.0 and 1.5, the damage will be with large spalling pieces. If the

value is above 1.5, the spalling will be more of a peeling off kind which spalls layer by layer.

The HR parameter is the heating rate. The heating rate is under a square root as the influencing was determined to be of a diminishing non-linear influence as the heating rate gets higher. Examining the experimental results, the spalling changes for the 40_05 and 50_05 when increasing the heating rate from 10 to 30 °C/min while there is no change in the spalling behaviour for the _10 samples when changing the heating rate from 30 to 50 °C/min. This points to a non-linear influence for the heating rate. A sketch to show this influence is shown in Figure 5.51, which is based on the 40 and 50 samples. The sketched orange line indicates the non-linear spalling line/front. Meaning that when a sample is below the line it will spall, and above it is safe.

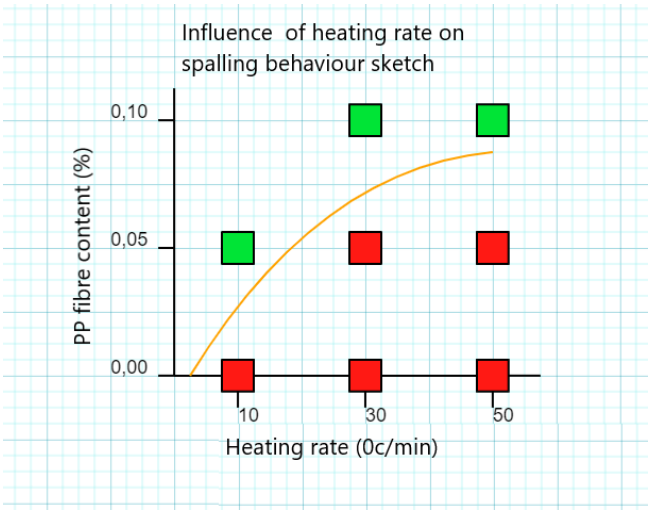


FIGURE 5.51: Sketch of heating rate influence on spalling behaviour. Yellow line indicating spalling front, green safe samples, red spalled samples

Finally, the influence of the pp fibre ratio and heating rate on the spalling behaviour has to be linked back to the pore connectivity. Quite straightforward, the pore connectivity increases when the pp fibre content increases. Using this relation, the pp fibre content can be substituted by the pore connectivity in the graph and spalling behaviour influence. Proving that the heating rate increases the risk of spalling, with a diminishing effect for higher heating rates.

$f_{ct,fl}$ is the flexural strength of the concrete. This captures the pore pressure build-up the sample is able to endure before cracking happens. Higher values indicate larger resistance. Thus, it is put in the divisor part of the function as it will decrease the spalling risk with higher values.

C_{MIP} is the pore connectivity determined through the MIP experiments. The connectivity is inserted as an absolute value and not a percentage. It takes into account the difficulty for the vapours to dissipate inside the sample. Meaning that the effect of higher connectivity is positive for the spalling resistance of a sample. Consequently, the pore connectivity trough MIP experiments is also inserted in the divisor part of the function.

$(0.20 - PP\%)^{1.5}/0.20$ is the part that takes into account the influence of the fibre. This is estimated at 0.20 based on the Eurocode recommendation of 2 kg/m3 which is approximately equal to 0.20 % [83], while PP% is the percentage of pp fibre present

in the cast sample. This part of the formula is constructed as a rational function as the influence of fibre is seen as a non-linear influence.

To further explain the rational function; it is evident that small percentages of fibres have almost no influence on the spalling mitigation while increasingly larger percentages will, after a certain percentage, always be able to mitigate spalling. This influence is already quite apparent in the experiments, as 0.05 % is only able to mitigate the 10 °C/min, while 0.10 % is able to mitigate up to 50 °C/min. Furthermore, to the power of 1.5 is applied to increase the effect of the rational function as it fits better to the presented results.

If a usable tortuosity value is found, it should replace this part of the formula. The tortuosity can give a better indication to extra influencing factors of the fibres such as fibre orientation and fibre length.

The 1,7 constant is determined by fitting the the variable parameters with the experimental results. It should be underlined however, that the value is not set in stone and was fitted to the experimental results. The constant might change with more data to analyse different influences on the spalling behaviour. For example, it could be possible that the influence of the heating rate doesn't act like a pure square root function, which could consequently alter the constant and the square root function. Possibly one of the earlier mentioned disregarded influencing factor has a unknown way in which it influences the different samples, and influence the constant.

The results for the samples at different heating rates are presented in Figure 5.52. As can be seen the formula captures the results of the experiments quite well with the exception of the 30 samples. However, the 30 samples had some trouble with testing circumstances as described in Section 4.1.

As can be seen, all the 0.00 % fibre samples show that they are prone to spalling as determined through the experiments. The lowest heating rate falling between 1.0 and 1.5 and should exhibit larger spalling pieces, which it did. The other samples are above 1.5 which indicates smaller spalling pieces, which is again true for the experiments.

For the 0.05 % samples there is no risk at 10 °C/min, risk of big spalling pieces at 30 °C/min and smaller spalling pieces layer by layer at 50 °C/min. This is all agrees with the observed experimental results.

Lastly, there is no risk of spalling for any of the 0.10 % fibre samples which again is in agreement with the experiments.

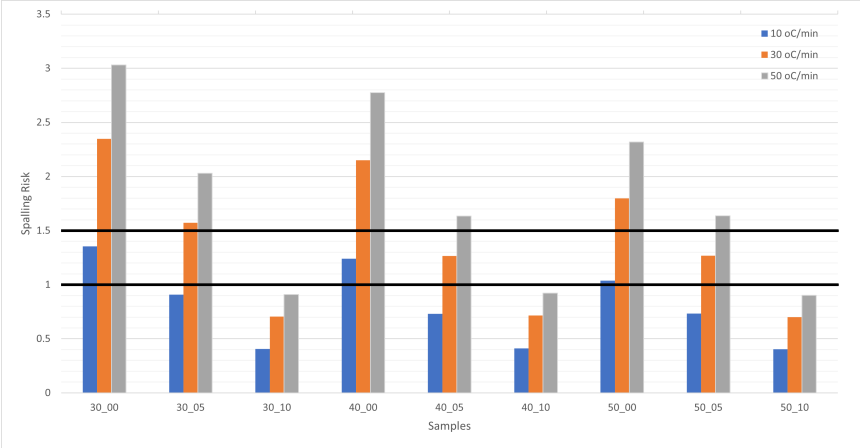


FIGURE 5.52: Determination of spalling risk using the determined formula

Points of attention are the chosen factors to fit results. These might change depending on results that are added. The current experiments were mostly focused on the influence of the fibre, heating rate and W/C ratio. As previously mentioned, more influencing factors should be considered such as the volume/surface ratio, the compressive stress, the degree of pore saturation and the tortuosity.

5.5 Discussion and Conclusions

The initial goal for the characterization of the pore structure was to find a link with the risk of spalling of cement based materials. While an absolute connection or formula has not been obtained, much can be concluded and contribute towards further research in the future. The main takes of the analytical research on the pore structure is summarized below.

1. It was reconfirmed through the analysis that porosity and pore size distribution are an unfit parameter to predict the thermal shock resistance of cement based materials. Both porosity and the pore size distribution show poor correlation with the oven tests. Additional observations could also be made based on the 3D images acquired.

    - Porosity has been shown to be largely influenced by the workability of the samples and the W/C ratio.

      The W/C ratio largely determines the porosity for the MIP results. Showing a direct correlation for the 30 and 50 samples. With the 40 samples there is some difference due to the addition of fibres, but still has decreasing porosity based on the W/C ratio.

      For the CT results the porosity seems to correlate most with the initial air content, which in turn is influenced by the workability, W/C ratio and the use of superplasticizer.

      The combined porosity from MIP and CT for each sample was observed to be quite close to each other. Displaying that when the W/C ratio is lowered with an accompanied higher workability, the porosity doesn't get lowered but redistributed from gel pores and small capillary pores to larger capillary pores and air voids.
    - The pore size distribution gave a clear overview of where the porosity resides in the studied pore range. A method to combine CT and MIP result into one pore size distribution has been presented. Showing that both results are compatible with each other and can be merged into one graph that displays the entire pore range. However, while compatible, every sample displayed some difference between CT and MIP results. This could be due to a variety of reasons. Mainly, difference between used MIP and CT sample, less accuracy for MIP in the higher pore diameter range, CT inaccuracy for the lower pore size range, or the difference in maturity.
    - There is more air entrainment and larger pores observed for the lower W/C ratio samples. In addition, the pp fibre ratio also increases the air content. For the 0.30 W/C ratio samples, the increased air entrainment is believed to be caused by the superplasticizer. With the 0.40 W/C ratio samples it is thought to be more of a workability issue, as there is a clear difference in porosity between the 0.00% and the 0.10% fibre sample while both contain no superplasticizer.

- Mix designs with a higher W/C ratio have a lower internal friction, causing the pp fibres to align in a horizontal direction, and possibly agglomerate. This could have implications on the effectiveness of the pp fibres.

2. Pore connectivity was initially deemed to be the missing link in the spalling prediction of mortar and concrete samples. It unfortunate to say that with the above used experiments the results are inconclusive at most. However, it is believed that with some adjustments more usable results could be achieved with future experimental research.

   - First off, the MIP results do give usable information on the pore connectivity in the gel pores and smaller capillary pores. With the information acquired, proving that besides the lower porosity, the pore connectivity is lowered as well. This will make the effective porosity even lower for the samples with a lower W/C ratios. Proving that the W/C ratio not only lowers the porosity but the pore connectivity as well by creating a more disconnected pore space within the material.
   - The main problem with the pore connectivity CT images being inconclusive is believed to be caused by the voxel size. A voxel size of 6.5 µm is too large to capture the intrinsic pore network that connects the larger capillary pores, fibres and air voids. Consequently, the acquired image stacks show a largely disconnected pore and fibre network while MIP results already prove that there is existing pore connectivity in the sample.
   - The proposed formula works for the given experimental samples.However, this formula only takes a couple of influencing factors into account. Namely, the W/C ratio, the heating rate, the connectivity through MIP, the tensile strength and the pp fibre ratio. Other known influencing factors from the literature review have not been added to the formula such as the volume/surface ratio, degree of pore saturation, the degree of constrained thermal dilation, influence of cyclical heating and of course the connectivity through CT images. Further research should prove if the proposed formula is indeed in the right direction.

Chapter 6

Conclusions and Recommendations

Unfortunately, no real connection could be made between the pore connectivity and the spalling behaviour of mortar samples. However, a number of conclusions and recommendations can be made based on the literature review and experimental results. This is a summation of the conclusions made at the end of each chapter combined with a final recommendation for future research.

Through literature review it has been found that pore connectivity is of significant influence on the thermo-hygral mechanism. The pore connectivity is in turn influenced by increase the W/C ratio and/or the pp fibre ratio as they both increases the connectivity between pores. Using the discovered definitions and quantification for the pore connectivity towards the proposed research was deemed insufficient. Instead, the tortuosity was chosen to be used as a way to measure the connectivity between pores. The tortuosity has shown to be inversely related to the pore connectivity in most cases. By using this inverse relation, the connectivity of the samples can be assessed.

The pp fibre proved to be the largest influence on the spalling behaviour of the mortar samples. A fibre percentage of 0.10% proved to mitigate spalling entirely in the researched samples, while the 0.05% was able to mitigate for the lowest heating rate of 10 C°/min. This is contrary to the samples without fibres, which were unable to prevent spalling at all heating rates. Once again proving the effectiveness of pp fibres in the prevention of spalling.

Furthermore, for this volume and mix design, the researched W/C ratio's showed to not influence the spalling behaviour of the samples. The proposed W/C ratios of 0.30, 0.40 and 0.50 all showed spalling at the same heating rates and fibre percentages. However, some differences in the spalling pieces were observed, and through literature review it is already proven to be of influence. Consequently, it can only be concluded to not influence the spalling behaviour of the samples researched in this paper, but should always be taken into account.

The tortuosity script in combination with the CT images proved to be insufficient in assessing the pore connectivity. The calculated values were at random, and showed no difference to known improved pore connectivity through higher fibre values. The difference between different W/C ratio's with similar fibre ratio's was also inconclusive. Consequently, it can only be concluded that through the research done, it held no correlation with the spalling behaviour and further developments are necessary in the algorithm or the utilization of the script.

However, the connectivity acquired trough MIP experiments proved to be quite useful in predicting the spalling behaviour. It is able to capture the influence of the

W/C ratio, and is believed to also be able to account the use of additives that could further reduce pore connectivity. Consequently, the MIP connectivity is thought to be a first step in mapping out the complete pore connectivity of a sample.

With the acquired results, a first estimation has been proposed to predict the spalling behaviour of mortar samples. A formula has been developed that takes into account the researched varying influences. Namely, the heating rate, the pp fibre ratio and the W/C ratio. It is believed to be a step in the direction of developing a formula containing all the possible influences on the thermal shock resistance of cement based materials. However, much is still to be researched. The goal of developing and using the connectivity acquired from CT images proved to be unfortunately insufficient due to the voxel size.

The advice for future research is thus to explore the possibility of lowering the voxel size to at least capture the connectivity of the samples between fibres and pores. An option could be to explore the use of nano-CT. However, this could shift the problem as it's current application is unable to capture the entirety of a sample, and instead is only able to capture a small volume of the already small CT sample. Nonetheless, it is believed that with the use of nano-CT the pore connectivity of a sample can be assessed more effectively. Multiple small volume areas can be selected to assess the pore connectivity to account for the inhomogeneity of the material. The key to make the pore connectivity representative then is how to implement the pore connectivity of these small volumes to the entirety of the sample.

Furthermore, the literature survey proved that an existing compressive force can significantly increase the risk of spalling. More specifically, the compressive force restricts the dilation caused by the heating. This is still a relatively poorly understood topic but believed to be with serious impact on the safety of structures. Combined with other factors such as the volume/surface ratio, degree of pore saturation, and the influence of cyclical heating much can still be researched in the future.

Hopefully, the findings of this research can contribute to the future investigations on further understanding the phenomenon. The thermal shock resistance and spalling risk of mortars and concrete structures proved to be a complex topic with more influencing factors than initially thought. The implications on the safety of structures are enormous and yet still quite unknown. It's precisely because of this that the final recommendation can only be to urge further research into this phenomenon to fully comprehend the full spalling mechanism with all it's influencing factors.

Bibliography

[1] A.B. Abell, K.L. Willis, and D.A. Lange. "Mercury Intrusion Porosimetry and Image Analysis of Cement-Based Materials". In: *Journal of Colloid and Interface Science* 211.1 (1999), pages 39–44. ISSN: 0021-9797. DOI: https://doi.org/10.1006/jcis.1998.5986. URL: https://www.sciencedirect.com/science/article/pii/S0021979798959860 (cited on pages 20, 61, 79).

[2] P.C. Aïtcin. *Science and technology of concrete admixtures*. Elsevier, 2016. ISBN: 978-0-08-100696-2. URL: http://dx.doi.org/10.1016/B978-0-08-100693-1.00001-1 (cited on pages 26–28).

[3] Pierer-Claude Aïtcin. *High-performance Concrete*. Taylor and Francis e-Library, 1998. ISBN: 0-203-47503-8. URL: - (cited on pages 6, 8, 19).

[4] Ali Nazari et al. "Thermal shock reactions of ordinary portland cement and geopolymer concrete: microstructural and mechanical investigation". In: 196.- (Nov. 2019), pages 492–498 (cited on page 28).

[5] Kalliopi K. Aligizaki. *Pore structure of Cement-based Materials*. Taylor and Francis, 2006. ISBN: 0-419-22800-4. URL: - (cited on pages 5–10).

[6] Dr. Salahaldein Alsadey. "Influence of Superplasticizer on Strength of Concrete". In: 1.3 (- 2012). ISSN: 2277-4378 (cited on pages 8, 26).

[7] Gerasimos S. Armatas. "Determination of the effects of the pore size distribution and pore connectivity on the pore tortuosity and diffusive transport in model porous networks". In: 61.- (Mar. 2006), pages 4662–4675 (cited on pages 10–12).

[8] Mugume Rodgers Bangi and Takashi Horiguchi. "Pore pressure development in hybrid fibre-reinforced high strength concrete at elevated temperatures". In: *Cement and Concrete Research* 41.11 (Nov. 2011), pages 1150–1156. ISSN: 00088846. DOI: 10.1016/j.cemconres.2011.07.001 (cited on page 18).

[9] Z Bazant. *Analysis of Pore Pressure, Thermal Stress and Fracture in Rapidly Heated Concrete*. en. 1997-02-13 1997. URL: https://tsapps.nist.gov/publication/get_pdf.cfm?pub_id=916655 (cited on pages 15, 16).

[10] James J. Beaudoin et al. "Solvent replacement studies of hydrated portland cement systems: The role of calcium hydroxide". In: *Advanced Cement Based Materials* 8.2 (Sept. 1998), pages 56–65. ISSN: 10657355. DOI: 10.1016/S1065-7355(98)00008-X (cited on page 61).

[11] James J. Beaudoin et al. "Solvent exchange in partially saturated and saturated microporous systems length change anomalies". In: *Cement and Concrete Research* 30.3 (Mar. 2000), pages 359–370. ISSN: 00088846. DOI: 10.1016/S0008-8846(99)00260-4 (cited on page 63).

[12] Sun Bei and Lin Zhixiang. "Investigation on spalling resistance of ultra-high-strength concrete under rapid heating and cooling". In: 4.- (- 2016), pages 146–153 (cited on pages 19, 25, 30).

[13] B.H. Bharatkumar et al. “Mix proportioning of high performance concrete”. In: 23.- (- 2001), pages 71–80 (cited on pages 1, 8, 25–27).

[14] V. Bhikshma, K Nitturkar, and Y. Venkatesham. “Investigation on mechanical properties of high strength silica fume concrete”. In: 10.3 (- 2009), pages 335–346 (cited on page 27).

[15] Nathan Bossa et al. “Micro- and nano-X-ray computed-tomography: A step forward in the characterization of the pore network of a leached cement paste”. In: *Cement and Concrete Research* 67 (Jan. 2015), pages 138–147. ISSN: 00088846. DOI: 10.1016/j.cemconres.2014.08.007 (cited on pages 10, 12, 20, 22).

[16] Lars Boström and Robert Jansson. “Spalling of self compacting concrete”. In: *Proceedings of 4th International Workshop on Structures in Fire :* Universidade de Averio, 2006 (cited on page 16).

[17] Bensaid Boulekbache et al. “Flowability of fibre-reinforced concrete and its effect on the mechanical properties of the material”. In: (2010). DOI: 10.1016/j.conbuildmat.2010.02.025 (cited on page 52).

[18] Sébastien Brisard, Marijana Serdar, and Paulo J.M. Monteiro. “Multiscale X-ray tomography of cementitious materials: A review”. In: *Cement and Concrete Research* 128.June 2019 (2020). ISSN: 00088846. DOI: 10.1016/j.cemconres.2019.105824 (cited on page 20).

[19] Sébastien Brisard, Marijana Serdar, and Paulo J.M. Monteiro. “Multiscale X-ray tomopgraphy of cementitious materials: A review”. In: 128.- (- 2020), page 105824 (cited on page 21).

[20] J.A. Cabrera-Madrid, J.I. Escalante-Garcia, and P. Castro-Borges. “Compressive strength of concretes with blast furnace slag. Re-visited state-of-the-art”. In: 6.1 (Jan. 2016), pages 64–83 (cited on page 27).

[21] Fabio Cardoso et al. “Scale-up effect on the drying behavior of high-alumina refractory castables”. In: *Journal of the Technical Association of Refractories* 23 (Jan. 2003), pages 226–230 (cited on page 17).

[22] Sammy Y.N. Chan, Gai-fei Peng, and John K.W. Chan. “Comparison between high strength concrete and normal strength concrete subjected to high temperature”. In: 29.- (Dec. 1996), pages 616–619 (cited on pages 1, 19).

[23] Y.N. Chan, X. Luo, and W.Sun. “Compressive strength and pore structure of high-performance concrete after exposure to high temperature up to 800 C”. In: 30.- (- 1999), pages 247–251 (cited on pages 1, 14, 20).

[24] Raymond John Connolly. “The spalling of concrete in fires.” In: (1998) (cited on page 18).

[25] G. Debicki, R. Haniche, and F. Delhomme. “An experimental method for assessing the spalling sensitivity of concrete mixture submitted to high temperature”. In: *Cement and Concrete Composites* 34.8 (Sept. 2012), pages 958–963. ISSN: 09589465. DOI: 10.1016/j.cemconcomp.2012.04.002 (cited on pages 17, 18).

[26] Sidney Diamond. “Aspects of concrete porosity revisited”. In: *Cement and Concrete Research* 29.8 (1999), pages 1181–1188. ISSN: 00088846. DOI: 10.1016/S0008-8846(99)00122-2 (cited on pages 6, 8, 61).

[27] Sidney Diamond. *Mercury porosimetry. An inappropriate method for the measurement of pore size distributions in cement-based materials*. 2000. DOI: 10.1016/S0008-8846(00)00370-7 (cited on page 20).

[28] Michael Doube et al. "BoneJ: Free and extensible bone image analysis in ImageJ". In: *Bone* 47.6 (2010), pages 1076–1079. ISSN: 87563282. DOI: 10.1016/j.bone.2010.08.023 (cited on pages 51, 58, 68).

[29] R. F. Feldman. "Diffusion measurements in cement paste by water replacement using Propan-2-OL". In: *Cement and Concrete Research* 17.4 (1987), pages 602–612. ISSN: 00088846. DOI: 10.1016/0008-8846(87)90133-5 (cited on page 61).

[30] R.F. Feldman. "Effect of Predrying on Rate of Water Replacement from Cement Paste by propan-2-oL". In: *Reprint from "il cemento"* 85 (1988) (cited on page 63).

[31] R. Feret. "Sur la Compacite des Mortiers Hydrauliques". In: *Ann. Pntas et Chaussees, Mem Doc* 4 (1892), pages 5–164. URL: https://ci.nii.ac.jp/naid/10004106953/en/ (cited on page 5).

[32] Yufang Fu and Lianchong Li. "Study on mechanism of thermal spalling in concrete exposed to elevated temperatures". In: (). DOI: 10.1617/s11527-010-9632-6 (cited on pages 14–16, 30).

[33] Cheon Goo Han et al. "Performance of spalling resistance of high performance concrete with polypropylene fiber contents and lateral confinement". In: *Cement and Concrete Research* 35.9 (2005), pages 1747–1753. ISSN: 00088846. DOI: 10.1016/j.cemconres.2004.11.013 (cited on pages 25, 30).

[34] Cheon-Goo Han et al. "Performance of spalling resistance of high performance concrete with polypropylene fiber contents and lateral confinement". In: 35.- (- 2005), pages 1747–1753 (cited on pages 1, 13).

[35] G. H.A. van der Heijden et al. "Moisture transport in heated concrete, as studied by NMR, and its consequences for fire spalling". In: *Cement and Concrete Research* 37.6 (June 2007), pages 894–901. ISSN: 00088846. DOI: 10.1016/j.cemconres.2007.03.004 (cited on page 19).

[36] Kristian Hertz. "Heat-Induced Explosion of Dense Concretes". In: (1984), page 20 (cited on pages 17–19).

[37] Peter C. Hewlett and Martin Liska. *DLea's Chemistry of Cement and Concrete*. Elsevier, 2019. ISBN: 978-0-08-100773-0. URL: https://www.elsevier.com/books/leas-chemistry-of-cement-and-concrete/hewlett/978-0-08-100773-0 (cited on pages 1, 5–10, 26, 27).

[38] J. Hoshen and R. Kopelman. "Percolation and cluster distribution. I. Cluster multiple labeling technique and critical concentration algorithm". In: *Physical Review B* 14.8 (1976), pages 3438–3445. ISSN: 01631829. DOI: 10.1103/PhysRevB.14.3438 (cited on page 12).

[39] Robert Jansson and Lars Bostro¨m. "The Influence of Pressure in the Pore System on Fire Spalling of Concrete". In: (). DOI: 10.1007/s10694-009-0093-9 (cited on page 18).

[40] Pierre Kalifa, Grégoire Chéné, and Christophe Gallé. "High-temperature behaviour of HPC with polypropylene fibres - From spalling to microstructure". In: *Cement and Concrete Research* 31.10 (Oct. 2001), pages 1487–1499. ISSN: 00088846. DOI: 10.1016/S0008-8846(01)00596-8 (cited on pages 13, 16, 20).

[41] Pierre Kalifa, Grégoire Chéné, and Christophe Gallé. "High-temperature behaviour of HPC with polypropylene fibres from spalling to microstructure". In: 31.- (- 2001), pages 1487–1499 (cited on pages 19, 30).

[42] Pierre Kalifa, François Dominique Menneteau, and Daniel Quenard. "Spalling and pore pressure in HPC at high temperatures". In: *Cement and Concrete Research* 30.12 (Dec. 2000), pages 1915–1927. ISSN: 00088846. DOI: 10.1016/S0008-8846(00)00384-7 (cited on pages 13, 14, 16).

[43] M Kanema et al. "Experimental and numerical studies of thermo-hydrous transfers in concrete exposed to high temperature". In: (). DOI: 10.1007/s00231-006-0212-9 (cited on page 14).

[44] M. Kanéma et al. "Spalling, Thermal, and Hydrous Behavior of Ordinary and High-Strength Concrete Subjected to Elevated Temperature". In: *Journal of Materials in Civil Engineering* 23.7 (2011), pages 921–930. ISSN: 0899-1561. DOI: 10.1061/(asce)mt.1943-5533.0000272 (cited on pages 15, 17, 19).

[45] Okan Karahan and Cengiz Duran Atiş. "The durability properties of polypropylene fiber reinforced fly ash concrete". In: *Materials & Design* 32.2 (2011), pages 1044–1049. ISSN: 0261-3069. DOI: https://doi.org/10.1016/j.matdes.2010.07.011. URL: https://www.sciencedirect.com/science/article/pii/S0261306910004462 (cited on page 19).

[46] Safwan A. Khedr and Mohamed Nagib Abou-Zeid. "Characteristics of silica-fume concrete". In: 6.3 (- 1994), pages 357–375 (cited on page 27).

[47] Gabriel Alexander Khoury. *Effect of fire on concrete and concrete structures*. Technical report (cited on page 16).

[48] Yun Yong Kim et al. "Effect of W/C ratio on durability and porosity in cement mortar with constant cement amount". In: *Advances in Materials Science and Engineering* 2014 (2014). ISSN: 16878442. DOI: 10.1155/2014/273460 (cited on page 6).

[49] Eike W. Klingsch. "Explosive spalling of concrete in fire". In: *BRISK Binary Robust Invariant Scalable Keypoints* (2009), pages 12–19. URL: https://doi.org/10.3929/ethz-a-010025751 (cited on pages 10, 13–16, 18, 19, 42).

[50] Radoslaw M. Kowalczyk, Agata M. Gajewicz, and Peter J. Mcdonald. "The mechanism of water-isopropanol exchange in cement pastes evidenced by NMR relaxometry". In: *RSC Advances* 4.40 (2014), pages 20709–20715. ISSN: 20462069. DOI: 10.1039/c4ra00889h (cited on pages 17, 61).

[51] Marija Krstic et al. "Freeze-thaw resistance and air-void analysis of concrete with recycled glass-pozzolan using X-ray micro-tomography". In: *Materials* 14.1 (2021), pages 1–26. ISSN: 19961944. DOI: 10.3390/ma14010154 (cited on page 80).

[52] Rakesh Kumar and Bishwa Bhattacharjee. "Porosity, pore size distribution and in situ strength of concrete". In: *Cement and Concrete Research* 33.1 (Jan. 2003), pages 155–164. ISSN: 00088846. DOI: 10.1016/S0008-8846(02)00942-0 (cited on page 9).

[53] Senthil Kumar and Manu Santhanam. "Particle packing theories and their application in concrete mixture proportioning: A review". In: -.13 (Sept. 2003), pages 1324–1331 (cited on page 29).

[54] Francois de Larrard and Thierry Sedran. "Mix-proportioning of high-performance concrete". In: 32.- (May 2002), pages 1699–1704 (cited on page 25).

[55] Maiko van Leeuwen. *School of Maiko*. Discussion with Lab technician at TU Delft. 2021 (cited on page 36).

[56] Ye Li et al. "Pore pressure build-up and explosive spalling in concrete at elevated temperature: A review". In: *Construction and Building Materials* 284 (May 2021), page 122818. ISSN: 09500618. DOI: 10.1016/j.conbuildmat.2021.122818 (cited on pages 14, 17, 19).

[57] Jin Cheng Liu and Kang Hai Tan. "Mechanism of PVA fibers in mitigating explosive spalling of engineered cementitious composite at elevated temperature". In: *Cement and Concrete Composites* 93 (Oct. 2018), pages 235–245. ISSN: 09589465. DOI: 10.1016/j.cemconcomp.2018.07.015 (cited on pages 10, 19, 20).

[58] Jin Cheng Liu, Kang Hai Tan, and Yao Yao. "A new perspective on nature of fire-induced spalling in concrete". In: *Construction and Building Materials* 184 (Sept. 2018), pages 581–590. ISSN: 09500618. DOI: 10.1016/j.conbuildmat.2018.06.204 (cited on pages 1, 13–18, 42).

[59] Jin Cheng Liu and Yao Zhang. "A simplified model to predict thermo-hygral behaviour and explosive spalling of concrete". In: *Journal of Advanced Concrete Technology* 17.7 (2019), pages 419–433. ISSN: 13468014. DOI: 10.3151/jact.17.419 (cited on page 14).

[60] T.J Lu and N.A. Fleck. "The thermal shock resistance of solids". In: 46.13 (- 1998), pages 4755–4768 (cited on pages 13, 17, 30).

[61] Ana Paula da Luz, Mariana A.L. Braulio, and Victor Pandolfelli. *Refractory Castable Engineering*. Göller Verlag GmbH, Germany, 2015. ISBN: 978-3-87264-004-8 (cited on pages 10, 13, 17, 19).

[62] Harun Mallisa and Gidion Turuallo. "Proceedings Conference: The maximum percentage of fly ash to replace part of original portland cement (OPC) in producing high strength concrete". In: *AIP conference proceedings 1903, 030012*. 2017. URL: https://doi.org/10.1063/1.5011519 (cited on page 28).

[63] Kumar Mehta and Paulo J.M. Monteiro. *Concrete: Microstructure, Properties and Materials*. The MCgraw-Hill Companies, 2006. ISBN: 0071589198. DOI: 10.1036/0071462899 (cited on pages 5–8, 10).

[64] F.F. Mendonça Filho et al. "Surface effects of molten slag spills on calcium aluminate cement paste". In: *Materials Design* 217 (2022), page 110623. ISSN: 0264-1275. DOI: https://doi.org/10.1016/j.matdes.2022.110623. URL: https://www.sciencedirect.com/science/article/pii/S0264127522002441 (cited on page 18).

[65] L D Mitchell and J C Margeson. "The effects of solvents on C-S-H as determined by thermal analysis". In: *Journal of Thermal Analysis and Calorimetry*. Volume 86. 3. 2006, pages 591–594. DOI: 10.1007/s10973-006-7712-1 (cited on page 61).

[66] Beat Münch and Lorenz Holzer. "Contradicting Geometrical Concepts in Pore Size Analysis Attained with Electron microscopy and Mercury Intrusion". In: 91.12 (- 2008), pages 4059–4067 (cited on pages 20, 80).

[67] Beat Münch and Lorenz Holzer. "Contradicting geometrical concepts in pore size analysis attained with electron microscopy and mercury intrusion". In: *Journal of the American Ceramic Society* 91.12 (2008), pages 4059–4067. ISSN: 00027820. DOI: 10.1111/j.1551-2916.2008.02736.x (cited on page 61).

[68] *NEN-EN 12390-13: Beproeving van verhard beton - Deel 13: Bepaling van de secans-elasticiteitsmodulus onder druk*. Standard. CEN-CENELEC Management Centre: Rue de la Science 23, B-1040 Brussels: Eurocode, June 2021 (cited on page 34).

[69] *NEN-EN 12390-5: Beproeving van verhard beton - Deel 5: buigsterkte van proefstukken*. Standard. CEN-CENELEC Management Centre: Rue de la Science 23, B-1040 Brussels: Eurocode, July 2021 (cited on pages 34, 35).

[70] *DIN EN 196-1: Methods of testing cement - Part 1: Determination of strength*. Standard. CEN-CENELEC Management Centre: Rue de la Science 23, B-1040 Brussels: Eurocode, - 2016 (cited on page 30).

[71] *NEN-EN 1015-7:1998 en. Beproevingsmethoden voor mortel voor metselwerk - Deel 7: Bepaling van het luchtgehalte van mortelspecie*. Standard. CEN-CENELEC Management Centre: Rue de la Science 23, B-1040 Brussels: Eurocode, Nov. 1998 (cited on page 35).

[72] Adam Neville and Pierre-Claude Aïtcin. "High performance concrete- An overview". In: 31.- (Mar. 1998), pages 111–117 (cited on pages 1, 5, 25–28).

[73] A. Noumowé et al. "High-Strength Self-Compacting Concrete Exposed to Fire Test". In: *Journal of Materials in Civil Engineering* 18.6 (2006), pages 754–758. ISSN: 0899-1561. DOI: 10.1061/(asce)0899-1561(2006)18:6(754) (cited on pages 18, 30).

[74] Treval Clifford Powers and Theodore Lucius Brownyard. "Studies of the physical properties of hardened Portland cement paste". In: *Journal Proceedings*. Volume 43. 9. 1946, pages 101–132 (cited on pages 6, 7).

[75] Michael Angelo B. Promentilla et al. "Characterizing the 3D pore structure of hardened Cement paste with synchrotron microtomography". In: *Journal of Advanced Concrete Technology* 6.2 (June 2008), pages 273–286. ISSN: 13468014. DOI: 10.3151/jact.6.273 (cited on pages 10, 12, 20).

[76] F T Ramal, R Salomão, and V C Pandolfelli. "Water content and its effect on the drying behaviour of refractory castables". In: *Refractories Applications & News* 10.3 (2005), pages 10–13. ISSN: 1537-6443 (cited on page 18).

[77] Mugume Rodgers Bangi and Takashi Horiguchi. "Effect of fibre type and geometry on maximum pore pressures in fibre-reinforced high strength concrete at elevated temperatures". In: (2011). DOI: 10.1016/j.cemconres.2011.11.014 (cited on page 19).

[78] Waldir L. Roque and Richelieu R.A. Costa. "A plugin for computing the pore/grain network tortuosity of a porous medium from 2D/3D MicroCT image". In: *Applied Computing and Geosciences* 5.August 2019 (2020), page 100019. ISSN: 25901974. DOI: 10.1016/j.acags.2020.100019. URL: https://doi.org/10.1016/j.acags.2020.100019 (cited on pages 81, 82).

[79] U. Schneider et al. *Physical properties and behaviour of high-performance concrete at high temperatures*. Springer, 2019. ISBN: 978-3-319-95431-8 (cited on pages 5, 14, 16).

[80] G. de Schutter and A.M. Poppe. "Quantification of the water demand of sand in mortar". In: *Construction and Building Materials* 18.7 (2004), pages 517–521. ISSN: 09500618. DOI: 10.1016/j.conbuildmat.2004.04.004 (cited on pages 29, 30).

[81] AGH University of Science and Technology in Krakow: department of fossil fuels. *porosimetry laboratory: theory*. URL: http://galaxy.agh.edu.pl/~kse/x/en/team/the-porosimetry-laboratory/ (cited on page 21).

[82] D. Snoeck et al. "The influence of different drying techniques on the water sorption properties of cement-based materials". In: *Cement and Concrete Research* 64 (Oct. 2014), pages 54–62. ISSN: 00088846. DOI: 10.1016/j.cemconres.2014.06.009 (cited on page 61).

[83] Hyoung-Seok So. "Spalling prevention of high performance concrete at high temperatures". In: - (Oct. 2016), pages -. DOI: 10.5772/64551. URL: https://www.intechopen.com/books/high-performance-concrete-technology-and-applications/spalling-prevention-of-high-performance-concrete-at-high-temperatures (cited on pages 1, 13, 14, 18–20, 25, 30, 85).

[84] E W Washburn and Edward W Washburn. *PHYSICS: NOTE ON A METHOD OF DETERMINING THE DISTRIBUTION OF PORE SIZES IN A POROUS MATERIAL*. Technical report (cited on page 20).

[85] Douglas Winslow and Ding Liu. "The pore structure of paste in concrete". In: *Cement and Concrete Research* 20.2 (1990), pages 227–235. ISSN: 00088846. DOI: 10.1016/0008-8846(90)90075-9 (cited on pages 28, 29).

[86] Chengqing Wu, Jun Li, and Yu Su. *Development of Ultra-High Performance Concrete againsts Blasts*. Elsevier, 2018. ISBN: 978-0-08-102495-9. URL: https://www.sciencedirect.com/book/9780081024959/development-of-ultra-high-performance-concrete-against-blasts (cited on pages 1, 10, 25, 27).

[87] Zhuqing Yu and Guang Ye. "The pore structure of cement paste blended with fly ash". In: 45.- (- 2013), pages 30–35 (cited on page 27).

[88] Zhuqing Yu et al. "Relationship between water permeability and pore structure of Portland cement paste blended with fly ash". In: *Construction and Building Materials* 175 (2018), pages 458–466. ISSN: 09500618. DOI: 10.1016/j.conbuildmat.2018.04.147. URL: https://doi.org/10.1016/j.conbuildmat.2018.04.147 (cited on page 80).

[89] Mathhias Zeiml et al. "How do polypropylene fibers improve the spalling behavior of in-situ concrete". In: 36.- (- 2006), pages 929–942 (cited on page 10).

[90] Matthias Zeiml et al. "How do polypropylene fibers improve the spalling behavior of in-situ concrete?" In: *Cement and Concrete Research* 36.5 (May 2006), pages 929–942. ISSN: 00088846. DOI: 10.1016/j.cemconres.2005.12.018 (cited on pages 13–16, 18–20, 25).

[91] Jie Zhang and George W. Scherer. "Comparison of methods for arresting hydration of cement". In: *Cement and Concrete Research* 41.10 (Oct. 2011), pages 1024–1036. ISSN: 00088846. DOI: 10.1016/j.cemconres.2011.06.003 (cited on pages 18, 61–63).

[92] Yong Zhang et al. "Ink-bottle E ff ect and Pore Size Distribution of Cementitious Materials Identified by Pressurization – Depressurization Cycling Mercury". In: *Materials* (2019) (cited on page 80).

[93] Zhidong Zhang and George W. Scherer. "Supercritical drying of cementitious materials". In: *Cement and Concrete Research* 99 (Sept. 2017), pages 137–154. ISSN: 00088846. DOI: 10.1016/j.cemconres.2017.05.005 (cited on page 61).

[94] Zhidong Zhang and George W. Scherer. "Evaluation of drying methods by nitrogen adsorption". In: *Cement and Concrete Research* 120 (June 2019), pages 13–26. ISSN: 00088846. DOI: 10.1016/j.cemconres.2019.02.016 (cited on page 61).

[95] Zhidong Zhang, George W. Scherer, and Alexandre Bauer. "Morphology of cementitious material during early hydration". In: *Cement and Concrete Research* 107 (May 2018), pages 85–100. ISSN: 00088846. DOI: 10.1016/j.cemconres.2018.02.004 (cited on pages 6, 61).

[96] Yanjing Zhao et al. "Characterization of interconnectivity, size distribution and uniformity of air voids in porous asphalt concrete using X-ray CT scanning images". In: *Construction and Building Materials* 213 (2019), pages 182–193. ISSN: 0950-0618. DOI: https://doi.org/10.1016/j.conbuildmat.2019.04.056. URL: https://www.sciencedirect.com/science/article/pii/S0950061819309043 (cited on page 11).

[97] Chunsheng Zhou et al. "Pore-size resolved water vapor adsorption kinetics of white cement mortars as viewed from proton NMR relaxation". In: *Cement and Concrete Research* 105 (Mar. 2018), pages 31–43. ISSN: 00088846. DOI: 10.1016/j.cemconres.2017.12.002 (cited on page 9).

[98] Chunsheng Zhou et al. "Pore-size resolved water vapor adsorption kinetics of white cement mortars as viewed from proton NMR relaxation". In: *Cement and Concrete Research* 105 (Mar. 2018), pages 31–43. ISSN: 00088846. DOI: 10.1016/j.cemconres.2017.12.002 (cited on pages 61–63).

[99] Semion Zhutovsky and Konstantin Kovler. "Chemical Shrinkage of High-Strength / High-Performance Cementitious Materials". In: *International Review of Chemical Engineering (IRECHE)* 10.1 (2018), page 1. ISSN: 2035-1755. DOI: 10.15866/ireche.v10i1.15794 (cited on page 6).

Appendix A

Figures Oven Results

A.1 Oven results 30 samples

A.1.1 30_0 at 10°C/min

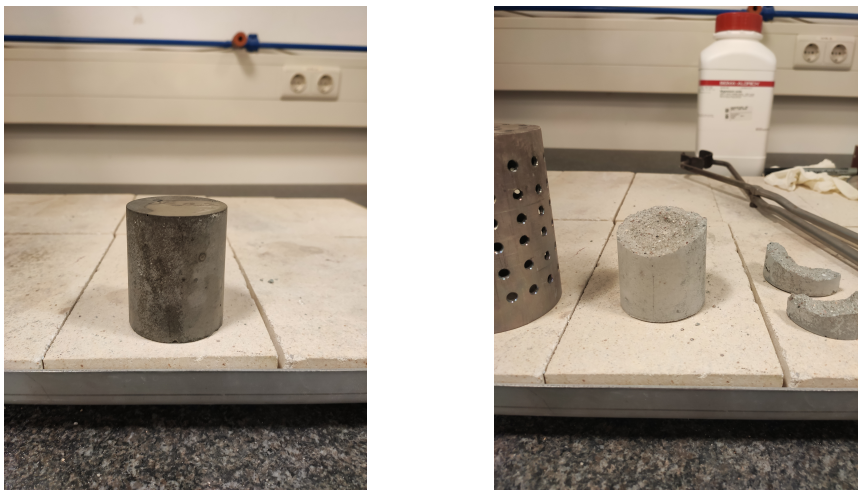


FIGURE A.1: w/c ratio 0,3 and 0,00% fibre at 10°C/min



FIGURE A.2: w/c ratio 0,3 and 0,00% fibre at 10°C/min

A.1.2 30_0 at 30°C/min

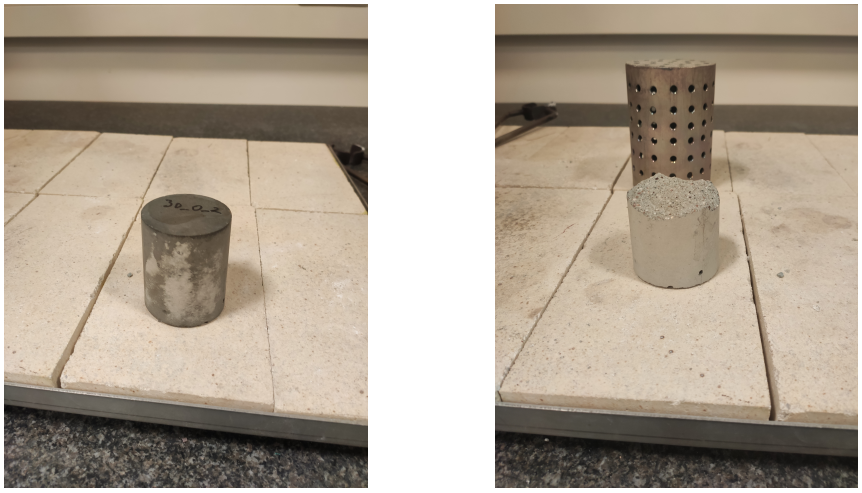


FIGURE A.3: w/c ratio 0,3 and 0,00% fibre at 30°C/min



FIGURE A.4: w/c ratio 0,3 and 0,00% fibre at 30°C/min

A.1.3 30_0 at 50°C/min



FIGURE A.5: w/c ratio 0,3 and 0,00% fibre at 50°C/min



FIGURE A.6: w/c ratio 0,3 and 0,00% fibre at 50°C/min

A.1.4 30_5 at 30°C/min

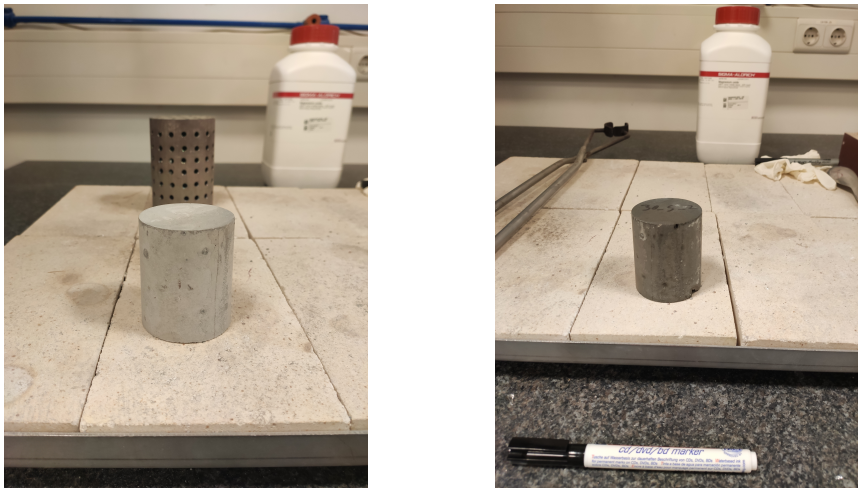


FIGURE A.7: w/c ratio 0,3 and 0,05% fibre at 30°C/min

A.1.5 30_5 at 50°C/min



FIGURE A.8: w/c ratio 0,3 and 0,05% fibre at 50°C/min

A.1.6 30_1 at 50°C/min

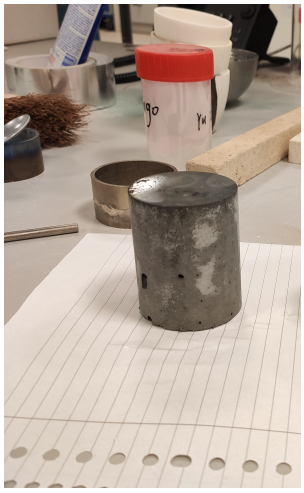




FIGURE A.9: w/c ratio 0,3 and 0,1% fibre at 50°C/min

A.2 Oven results 40 samples

A.2.1 40_0 at 10°C/min





FIGURE A.10: w/c ratio 0,4 and 0,00% fibre at 10°C/min




FIGURE A.11: w/c ratio 0,4 and 0,00% fibre at 10°C/min

A.2.2 40_0 at 50°C/min




FIGURE A.12: w/c ratio 0,4 and 0,00% fibre at 50°C/min




FIGURE A.13: w/c ratio 0,4 and 0,00% fibre at 50°C/min

A.2.3 40_5 at 10°C/min

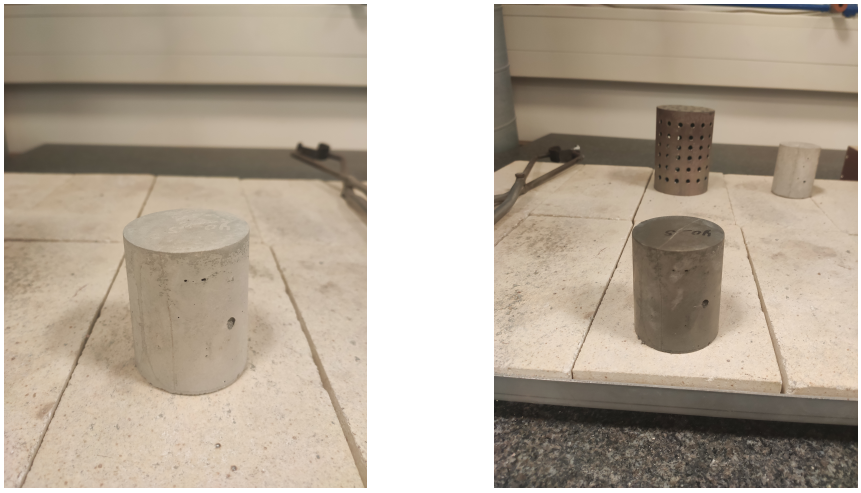


FIGURE A.14: w/c ratio 0,4 and 0,05% fibre at 10°C/min

A.2.4 40_5 at 30°C/min

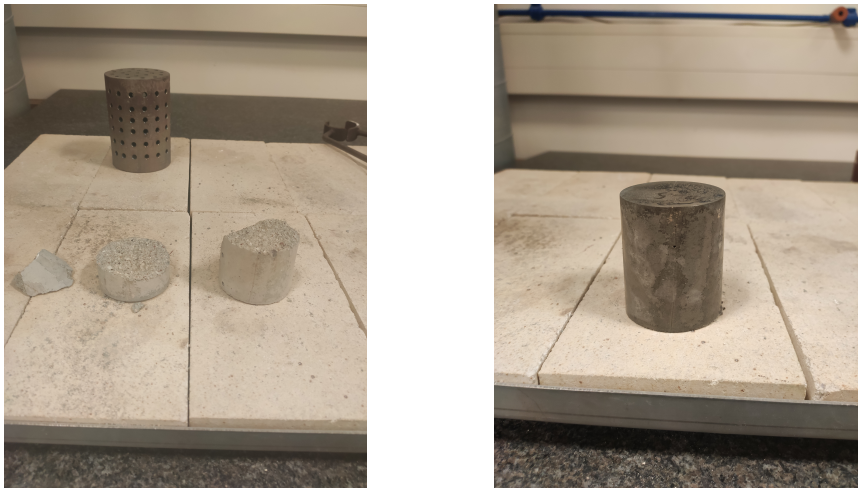


FIGURE A.15: w/c ratio 0,4 and 0,05% fibre at 30°C/min




FIGURE A.16: w/c ratio 0,4 and 0,05% fibre at 30°C/min

A.2.5 40_5 at 50°C/min




FIGURE A.17: w/c ratio 0,4 and 0,05% fibre at 50°C/min



FIGURE A.18: w/c ratio 0,4 and 0,05% fibre at 50°C/min

A.2.6 40_1 at 30°C/min

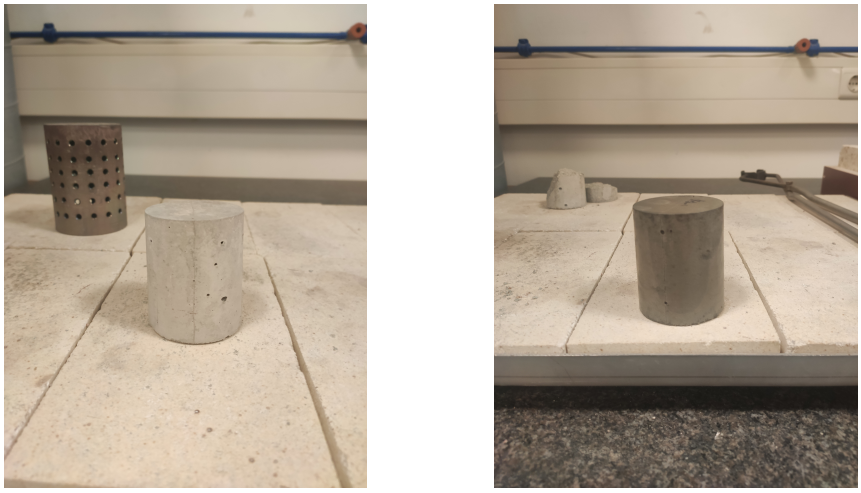


FIGURE A.19: w/c ratio 0,4 and 0,1% fibre at 30°C/min

A.2.7 40_1 at 50°C/min

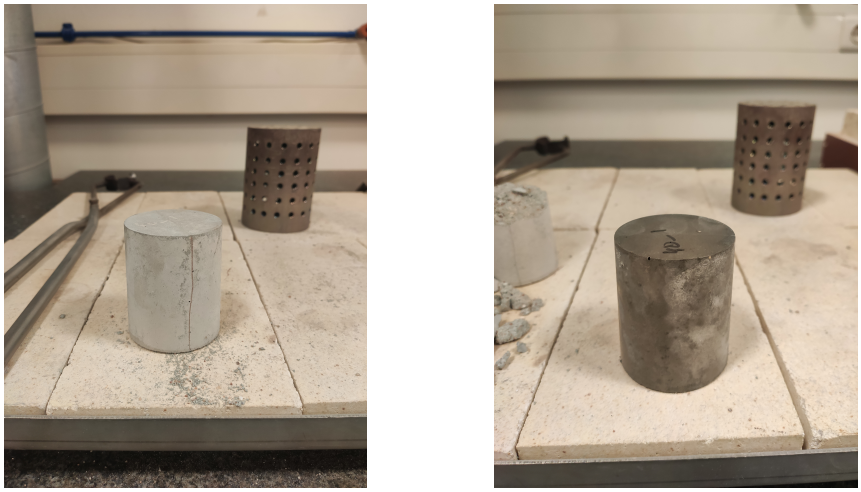


FIGURE A.20: w/c ratio 0,4 and 0,1% fibre at 50°C/min

A.3 Oven results 50 samples

A.3.1 50_0 at 10°C/min



FIGURE A.21: w/c ratio 0,5 and 0,00% fibre at 10°C/min



FIGURE A.22: w/c ratio 0,5 and 0,00% fibre at 10°C/min

A.3.2 50_5 at 10°C/min



FIGURE A.23: w/c ratio 0,5 and 0,05% fibre at 10°C/min

A.3.3 50_5 at 30°C/min



FIGURE A.24: w/c ratio 0,5 and 0,05% fibre at 30°C/min




FIGURE A.25: w/c ratio 0,5 and 0,05% fibre at 30°C/min

A.3.4 50_5 at 50°C/min

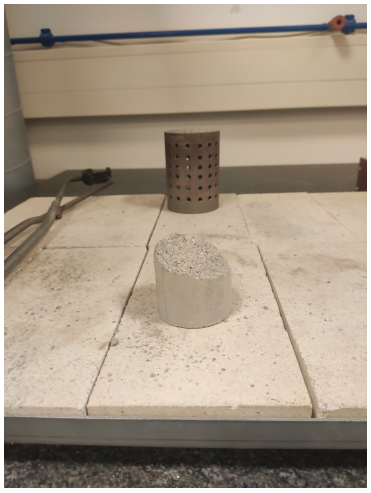



FIGURE A.26: w/c ratio 0,5 and 0,05% fibre at 50°C/min




FIGURE A.27: w/c ratio 0,5 and 0,05% fibre at 50°C/min

A.3.5 50_1 at 30°C/min

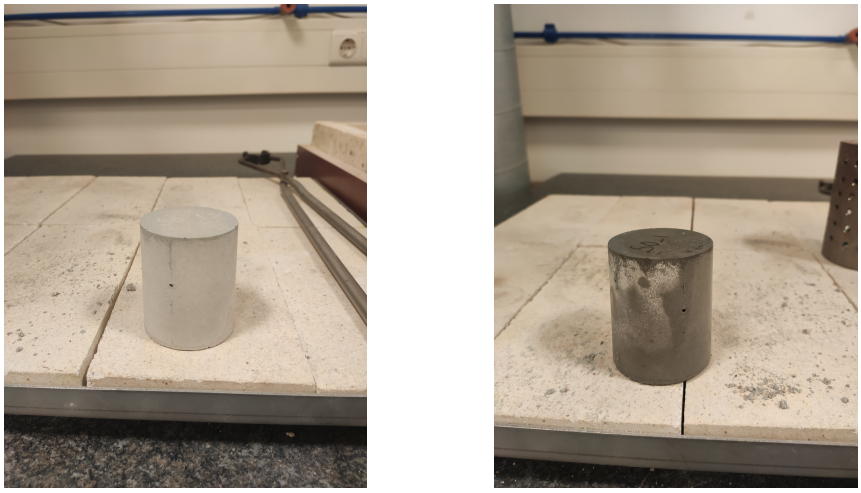


FIGURE A.28: w/c ratio 0,5 and 0,1% fibre at 30°C/min

A.3.6 50_1 at 50°C/min

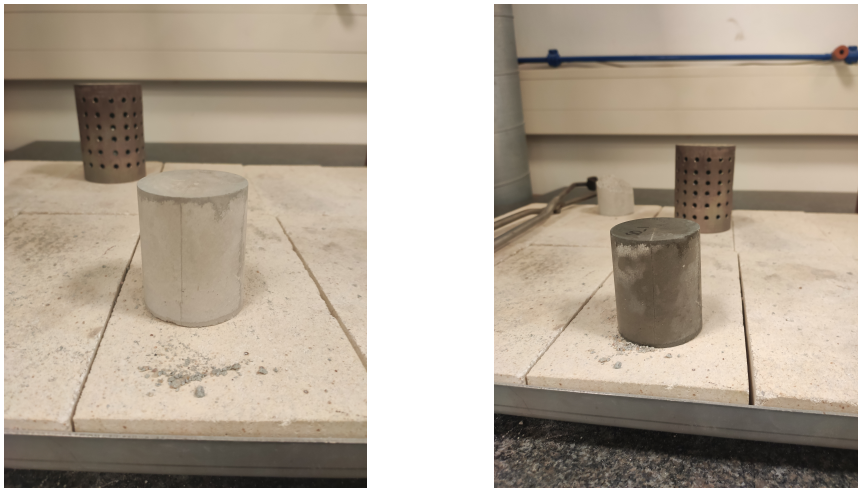


FIGURE A.29: w/c ratio 0,5 and 0,1% fibre at 50°C/min

Appendix B

VGStudio Max 3D reconstruction images

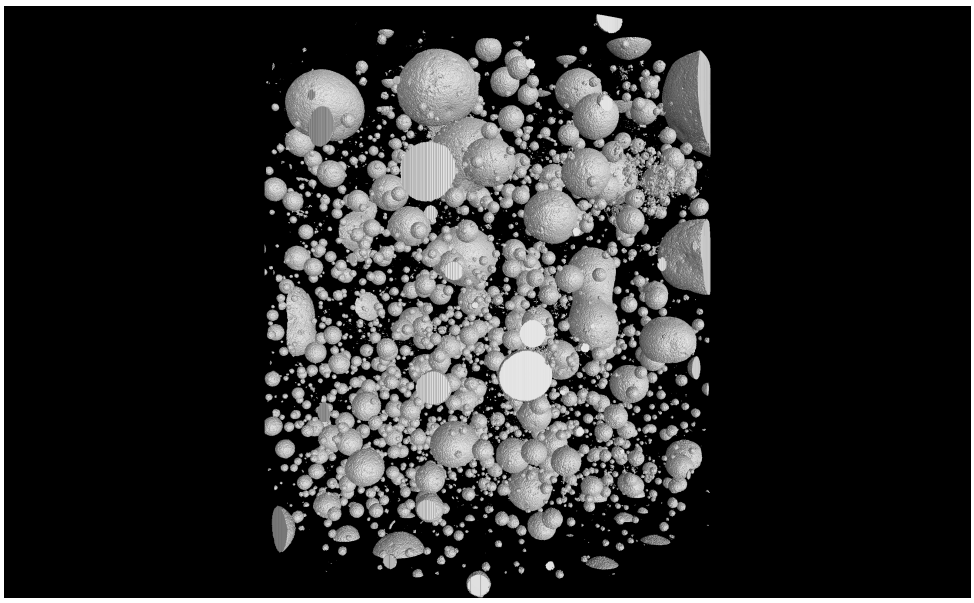


FIGURE B.1: 3D view of pores in the 30_0 sample through VGStudio Max 3.0

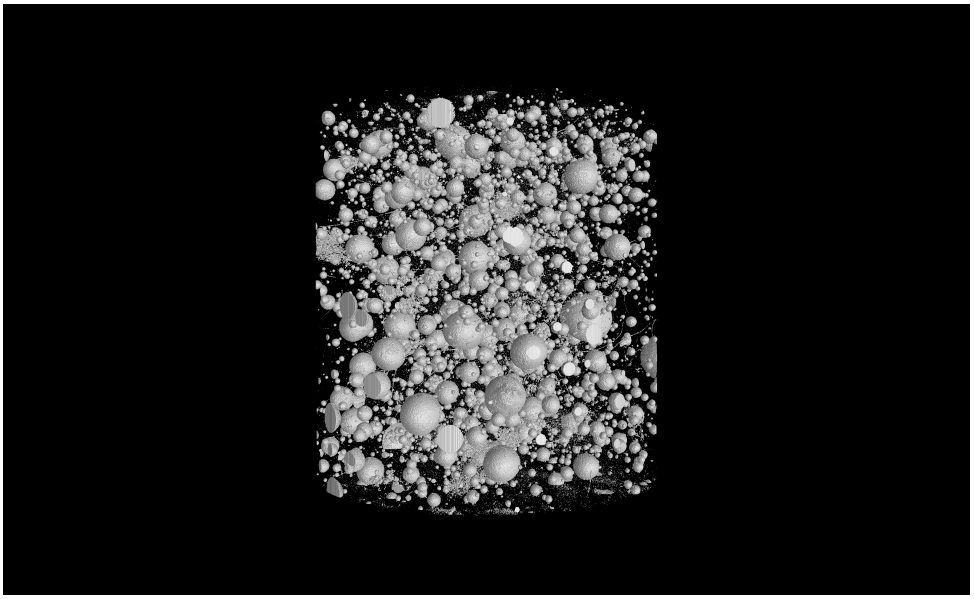


FIGURE B.2: 3D view of pores and pp fibres in the 30_5 sample through VGStudio Max 3.0

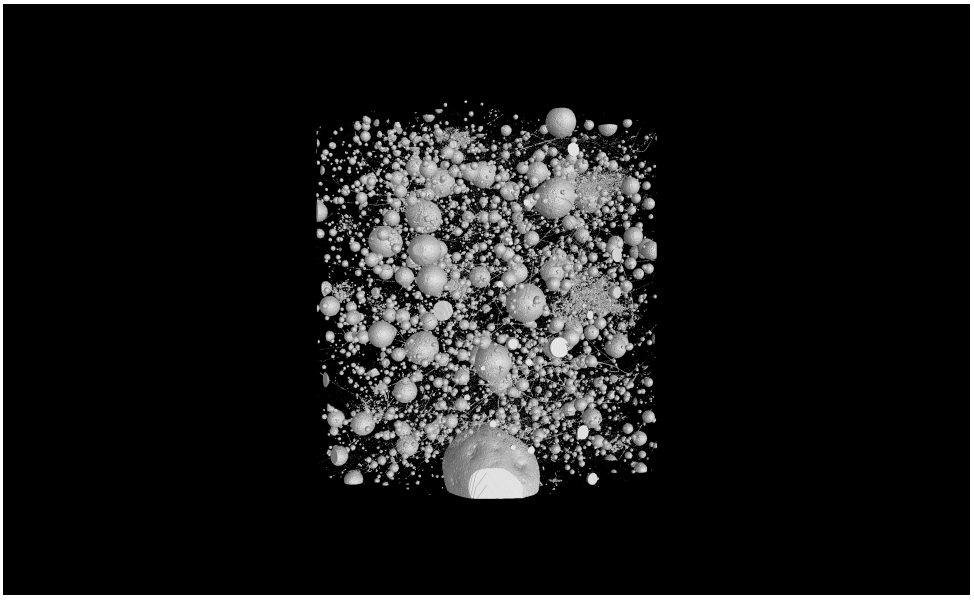


FIGURE B.3: 3D view of pores and pp fibres in the 30_1 sample through VGStudio Max 3.0

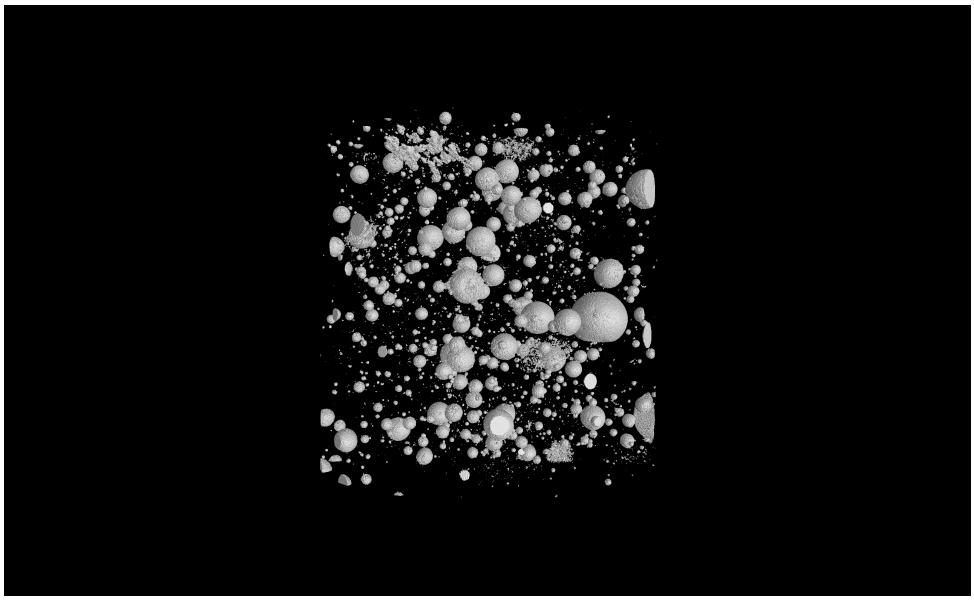


FIGURE B.4: 3D view of pores of the 40_0 sample through VGStudio Max 3.0

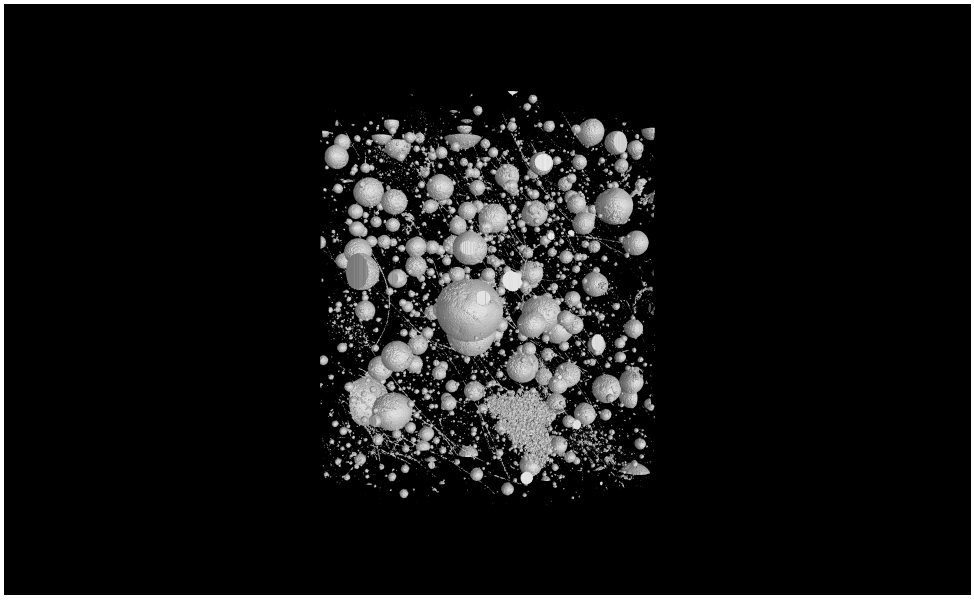


FIGURE B.5: 3D view of pores and pp fibres of the 40_5 sample through VGStudio Max 3.0

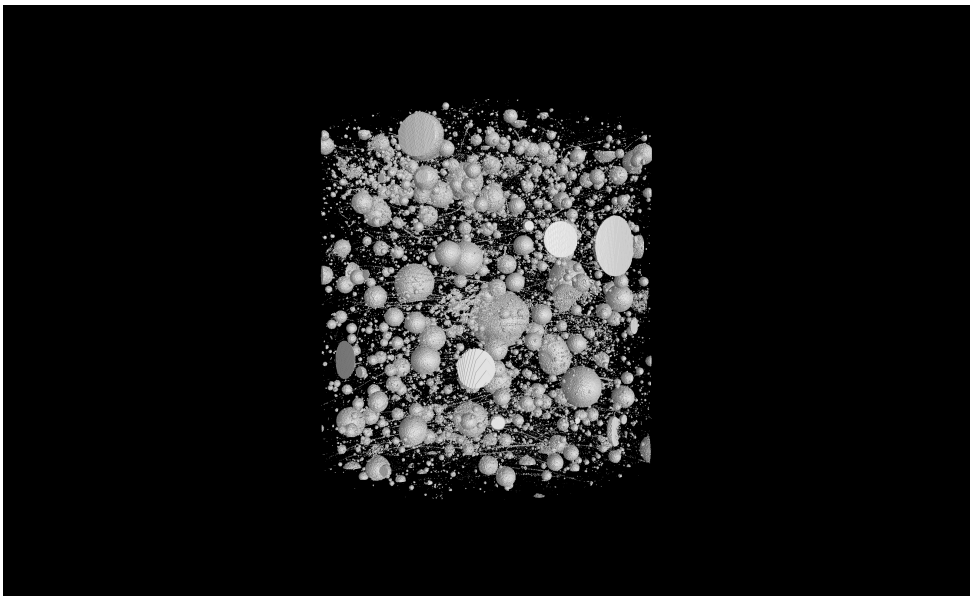


FIGURE B.6: 3D view of pores and pp fibres of the 40_1 sample through VGStudio Max 3.0

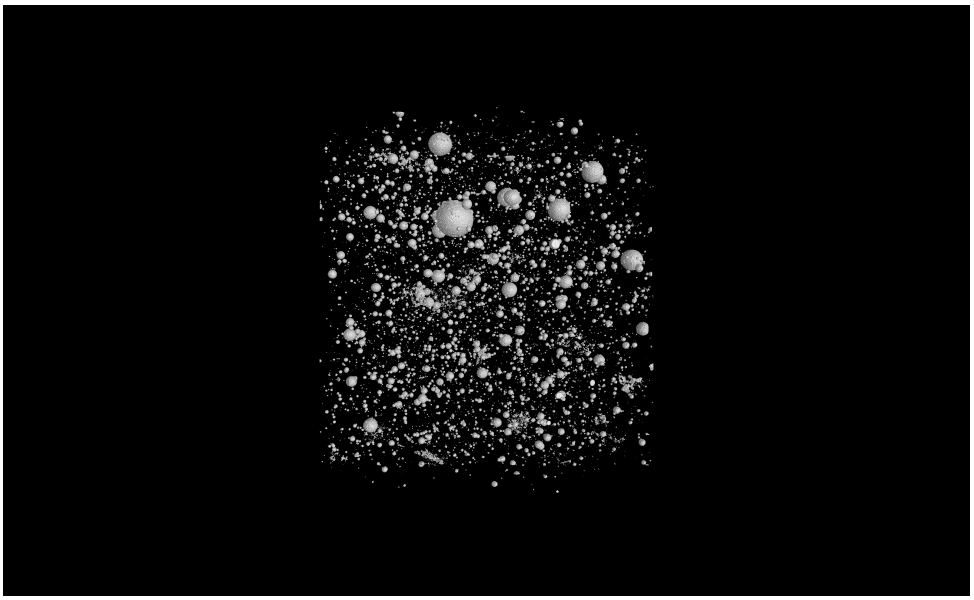


FIGURE B.7: 3D view of pores of the 50_0 sample through VGStudio Max 3.0

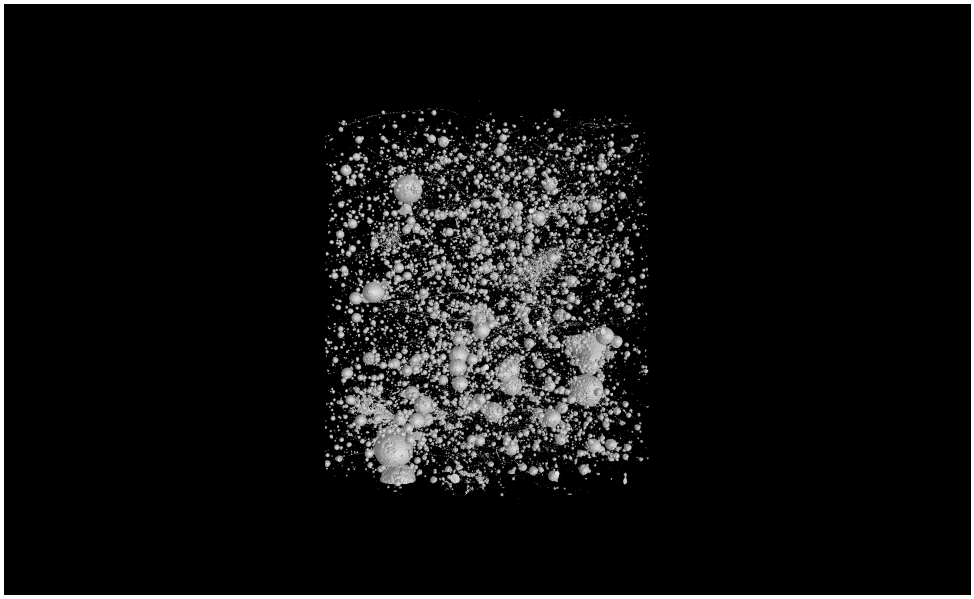


FIGURE B.8: 3D view of pores and pp fibres of the 50_5 sample through VGStudio Max 3.0

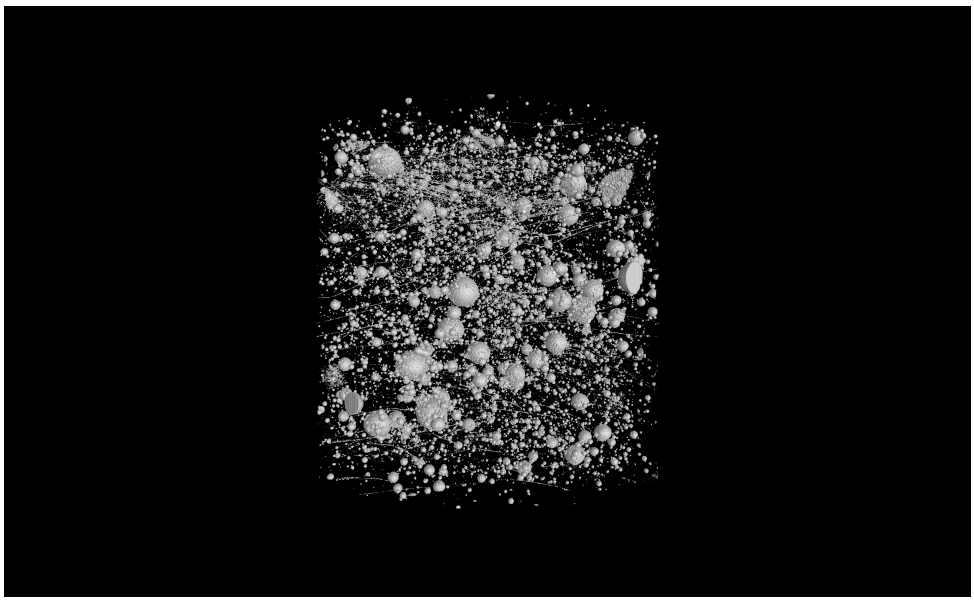


FIGURE B.9: 3D view of pores and pp fibres of the 50_1 sample through VGStudio Max 3.0

Appendix C

Tortuosity results

Overview of the tortuosity results in all tested directions. Negative directions were abandoned to test as the negative direction showed similar results to the positive direction, while running the script in an additional direction took multiple hours. Consequently, the negative direction was skipped to save time.

Graphs below present the results for each of the tortuosity scripts ran. In the pore and fibre space, the non-pore space and the cement + pores and fibres space. Furthermore, some samples have a tested negative direction to prove the minimal difference in results.

TABLE C.1: Tortuosity pores and fibre space

Direction	30_00	30_05	30_10	40_00	40_05	40_10	50_00	50_05	50_10
x(+)	1.012319	1.009736	1.007623	1.005237	1.008174	1.008809	1.001440	1.003305	1.003702
x(-)	-	1.009785	1.0075809	-	-	-	-	-	-
y(+)	1.012869	1.009220	1.006835	1.005175	1.007872	1.008033	1.001422	1.003371	1.003974
y(-)	-	1.009193	-	-	-	-	-	-	-
z(+)	1.0093708	1.008227	1.006211	1.004915	1.008131	1.006984	1.001269	1.002975	1.003435
z(-)	-	-	-	-	-	-	-	-	-
Average	1.001151	1.00923	1.00706	1.00511	1.00806	1.00794	1.0138	1.00322	1.00370

TABLE C.2: Tortuosity non-pore space

Direction	30_00	30_05	30_10	40_00	40_05	40_10	50_00	50_05	50_10
x(+)	1.08438	1.46036	1.80620	1.01116	1.81326	1.37061	1.00017	1.01218	1.07939
x(-)	1.02755	1.32698	1.80416	1.02428	0.99934	1.36348	1.00780	1.00159	1.00126
y(+)	1.76822	1.47396	1.10445	1.00221	1.00463	1.24617	1.00096	1.00214	1.00830
y(-)	1.72379	1.49200	1.09816	1.00468	1.26686	1.00069	1.00184	1.00214	1.15663
z(+)	1.00927	1.00689	1.00237	0.99956	0.99782	0.99849	1.00000	0.99993	0.99976
z(-)	0.99649	0.99561	1.00165	1.00040	1.00041	1.00113	0.99999	0.99997	1.00009
Average	1.26828	1.29263	1.30283	1.00705	1.18039	1.16343	1.00179	1.00299	1.04090

TABLE C.3: Tortuosity Cement+ pores

Direction	30_00	30_05	30_10	40_00	40_05	40_10	50_00	50_05	50_10
x(+)	1.08939	1.05945	1.08848	1.06897	1.10950	1.10456	1.07354	1.08090	1.10047
x(-)	1.08989	-	-	-	-	-	1.07415	-	1.09933
y(+)	1.09381	1.06029	1.08640	1.07010	1.11078	1.10415	1.07561	1.08200	1.10139
y(-)	1.09202	-	-	-	-	-	1.07670	-	1.09942
z(+)	1.06244	1.04886	1.06402	1.05006	1.07055	1.06722	1.05561	1.05776	1.06121
z(-)	1.06339	-	-	-	-	-	1.05575	-	1.06281
Average	1.08188	1.05620	1.07963	1.06304	1.09694	1.09198	1.06825	1.07356	1.08769